Storage of fiber-guided light in a nanofiber-trapped ensemble of cold cesium atoms

DISSERTATION

zur Erlangung des akademischen Grades

Doktor der technischen Wissenschaften

eingereicht von

Bernhard Albrecht

Matrikelnummer 0626209

Julius Raab Straße 10/4, 2345 Brunn am Gebirge

an der
Fakultät für Physik der Technischen Universität Wien

Betreuung: Prof. Dr. Arno Rauschenbeutel, E141 – Atominstitut

Diese Dissertation haben begutachtet:

(Prof. Dr. Arno Rauschenbeutel)	(Begutachter extern 1)	(Begutachter extern 2)

Wien, 03.09.2016

(Bernhard Albrecht)

Storage of fiber-guided light in a nanofiber-trapped ensemble of cold cesium atoms

DISSERTATION

submitted in partial fulfillment of the requirements for the degree of

Doktor der technischen Wissenschaften

by

Bernhard Albrecht

Registration Number 0626209

Julius Raab Straße 10/4, 2345 Brunn am Gebirge

to the Faculty of Physics
at the Vienna University of Technology

Advisor: Prof. Dr. Arno Rauschenbeutel, E141 – Atominstitut

The dissertation has been reviewed by:

(Prof. Dr. Arno Rauschenbeutel)	(Begutachter extern 1)	(Begutachter extern 2)

Wien, 03.09.2016

(Bernhard Albrecht)

Abstract

To store a classical light pulse is an important capability for the realization of all-optical signal processing schemes. Optical buffers that allow storing optical pulses can be extended to work as optical quantum memories, in which quantum states of light can be stored. Those optical quantum memories are crucial elements of large-scale quantum optical networks.

The storage of light has been achieved with several systems, such as cold or ultracold atoms. Despite this, the realization of efficient and long-lived fiber-integrated optical memories is still subject to active research.

In this thesis, I report on the progress towards a novel implementation of an optical quantum memory. Here, a nanofiber-based experimental platform for trapping and optically interfacing laser-cooled Cesium atoms is used, where the nanofiber is realized as the waist of a tapered optical fiber. Despite the atoms being trapped close to the nanofiber surface, the system offers a long ground state coherence time. This, in combination with the good coupling of the trapped atoms to fiber-guided light fields, renders this system a promising candidate for the realization of a fiber-coupled quantum memory.

I demonstrate the realization of an optical memory for weak optical pulses, using the effect of electromagnetically induced transparency. This effect allows to drastically reduce the group velocity of a fiber-coupled light pulse when propagating through the medium. Eventually, the light pulse can be brought to a halt. In this context, I experimentally show storage and retrieval of fiber-guided light at the single-photon level, while featuring a competitive characteristic memory lifetime. The presented results are an important step towards realizing fully fiber-based quantum networks.

For further improvement of the lifetime of the presented optical memory, it is of advantage to gain better control over the trapped atom's motional degree of freedom. One possibility to achieve this goal utilizes the trapping light field-induced fictitious magnetic fields. It allows the coupling between the external motional state and the internal hyperfine state of the atom. As shown in this thesis, this coupling can be used to implement microwave sideband cooling, allowing the preparation of the majority of the nanofiber-coupled Cesium atoms in the motional ground state. Furthermore, the coupling can be utilized as a tool to probe specific parameters of the trapped atoms, such as the trap frequency, the mean motional excitation number or the heating rate.

Kurzfassung

Die Fähigkeit klassische Lichtpulse abspeichern zu können ist unerlässlich für die Realisierung vollständig optischer Methoden zur Signalverarbeitung. Diese optischen Zwischenspeicher können derart erweitert werden, dass sie als optische Quantenspeicher operieren, in welchen die Quantenzustände von Licht abgespeichert werden können. Solche Quantenspeicher sind unabdingbare Elemente weitverzweigter optischer Quantennetzwerke.

Das Abspeichern von Lichtpulsen wurde bereits mithilfe mehrerer Systeme erreicht, wie zum Beispiel mit kalten oder ultrakalten Atome. Dennoch ist die Realisierung effizienter und langlebiger optischer Speicher, integriert in einer Glasfaser, noch immer Ziel aktiver Forschung.

In dieser Doktorarbeit berichte ich über den Fortschritt in Richtung einer neuartigen Implementierung eines optischen Quantenspeichers. Zu diesem Zweck wird eine Nanofaser basierte experimentelle Plattform verwendet, die das Fangen lasergekühlter Cäsium Atome erlaubt und eine optische Schnittstelle zwischen dem fasergeführten Licht und den gefangenen Atomen bereitstellt. Die Nanofaser wird hierbei als eine verjüngte Glasfaser realisiert. Obwohl die Atome nahe der Oberfläche der Nanofaser gefangen werden, bietet das System lange Kohärenzzeiten des atomaren Grundzustandes. Dies, zusammen mit der guten Kopplung der gefangenen Atome an das fasergeführte Lichtfeld, macht aus diesem System einen vielversprechenden Kandidaten für die Realisierung eines fasergekoppelten Quantenspeichers.

Ich demonstriere die Realisierung eines optischen Speichers für schwache Lichtpulse, unter Verwendung des Effekts der elektromagnetisch induzierten Transparenz. Dieser Effekt ermöglicht es, die Gruppengeschwindigkeit eines Lichtpulses im atomaren Medium drastisch zu reduzieren und sogar innerhalb des Mediums zu stoppen. In diesem Zusammenhand zeige ich experimentell das Abspeichern und Abrufen fasergeführter Lichtpulse, bestehend aus einzelnen Photonen, mit einer konkurrenzfähigen charakteristischen Speicherzeit. Diese Resultate sind ein wichtiger Schritt in Richtung vollständig glasfaserbasierter optischer Speicher.

Um die Speicherzeit weiter erhöhen zu können, ist es vorteilhaft mehr Kontrolle über die Bewegungsfreiheitsgrade der gefangenen Atome zu erhalten. Eine Möglichkeit um dies zu erreichen wird in dieser Arbeit vorgestellt. Hier macht man sich die fiktiven Magnetfelder zunutze, welche durch die Fallenlichtfelder induziert werden und die Kopplung zwischen dem externen Bewegungszustand und dem internen Hyperfeinzustand der Atome ermöglichen. Dies erlaubt die Implementierung von Mikrowellen Seitenbandkühlen, was einen befähigt den Großteil der gefangenen Cäsium Atome im niedrigsten Bewegungszustand zu präparieren. Zusätzlich kann diese Kopplung verwendet werden um diverse Parameter der gefangenen Atome, wie zum Beispiel die Fallenfrequenz, den mittleren Bewegungszustand oder die Heizrate, zu untersuchen.

List of Publications

In the process of working on this thesis, the following articles have been published in peer-reviewed journals or will be published soon:

- B. Albrecht, Y. Meng, C. Clausen, A. Dareau, P. Schneeweiss, and A. Rauschenbeutel.
  Fictitious magnetic-field gradients in optical microtraps as an experimental tool for interrogating and manipulating cold atoms
  Phys. Rev. A, 94, 061401, 2016.

- C. Sayrin, C. Junge, R. Mitsch, B. Albrecht, D. O'Shea, P. Schneeweiss, J. Volz and A. Rauschenbeutel.
  Nanophotonic Optical Isolator Controlled by the Internal State of Cold Atoms
  Phys. Rev. X, 5, 041036, 2015.

- C. Sayrin, C. Clausen, B. Albrecht, P. Schneeweiss and A. Rauschenbeutel.
  Storage of fiber-guided light in a nanofiber-trapped ensemble of cold atoms
  Optica, 2, 353, 2015.

- R. Mitsch, C. Sayrin, B. Albrecht, P. Schneeweiss and A. Rauschenbeutel.
  Quantum state-controlled directional spontaneous emission of photons into a nanophotonic waveguide
  Nature Commun., 5:5713, 2014.

- R. Mitsch, C. Sayrin, B. Albrecht, P. Schneeweiss and A. Rauschenbeutel.
  Exploiting the local polarization of strongly confined light for sub-micrometer-resolution internal state preparation and manipulation of cold atoms
  Phys. Rev. A, 89:063829, 2014.

- D. Reitz, C. Sayrin, B. Albrecht, I. Mazets, R. Mitsch, P. Schneeweiss and A. Rauschenbeutel.
  Backscattering properties of a waveguide-coupled array of atoms in the strongly non-paraxial regime
  Phys. Rev. A, 89:031804(R), 2014.

Contents

viii

CHAPTER 1

Introduction

Quantum communication via quantum networks allows the user to efficiently exchange information and secure the latter by means of quantum cryptography [1–4]. To this end, the ability to distribute quantum states over distances of several $100\,\mathrm{km}$ is essential. To achieve such extensive networks, the connected quantum systems exchange information via photons, where the required transmission channels are usually optical fibers or free-space. In general, these transmission channels are subject to loss, which limits the distance over which two connected quantum systems can reliably communicate. Although the losses of optical fibers of less than $0.2\,\mathrm{dB/km}$ at telecommunication wavelengths are quite low, they still have a high impact on the photon transmission rate for a quantum network operating on a worldwide scale. On such a large scale the transmission rate can be reduced by several orders of magnitude. In classical communication networks, this problem can be solved by using repeaters that amplify the signal. This approach, however, cannot be directly applied for quantum networks due to the no-cloning theorem [5, 6]. Instead, one relies on quantum repeaters that are based on entanglement [7]. Here the transmission channel is divided into segments, that are spanning a shorter distance, and entanglement is created for each individual segment. In the following, the entanglement is distributed from one segment to the next via entanglement swapping [8]. This leads to an entanglement between the sender and the recipient in the end, without the need of direct interaction between both. In order for the entanglement swapping to properly perform, the entanglement of each individual segment has to be stored in a quantum memory until the entanglements in the adjacent segments have been established successfully [9]. One possible approach towards a quantum repeater [10] proposes the use of atomic ensembles as a quantum memory due to the strong and controllable coupling between the atomic ensemble and photons.

An example for the implementation of a quantum memory using an ensemble of atoms is via electromagnetically induced transparency (EIT) [11–13]. EIT leads to a modified optical response of an atomic ensemble, caused by a quantum interference between possible excitation paths between the atomic states, due to a coherent control light field. For the example of a three-level system, this results in the atomic medium being transparent for a light field resonant with the transition between two energy levels. Furthermore, EIT leads to an increased dispersion in

1

the spectral region of reduced absorption, giving rise to several effects including, e.g., reduced group velocities, longitudinal pulse compression and storage of light [14]. It is these features that render EIT very attractive for the realization of a quantum memory for photons, since it allows the transfer of quantum states and coherences to collective atomic spin excitations. In several experimental realizations, the capability of the EIT scheme to store light pulses as well as single photons has been demonstrated (e.g. [15, 16]). Furthermore, it has been shown that the nonclassical character of the correlation between a photon pair survives the storage and retrieval process [17].

In order to prepare an atomic ensemble, and provide a versatile light-matter interface, laser-cooled atoms confined in an optical dipole trap are of particular interest. Optical dipole forces have proven to be a universal tool for trapping and manipulating dipoles, such as, e.g., neutral atoms, ions or nitrogen-vacancy centers. These forces occur when dipoles interact with an electromagnetic field that features a gradient in its intensity. Depending on the frequency of the light field with respect to the transition frequency of the atom, the dipole forces can attract an atom towards the intensity maximum or repel it from the latter [18]. In the last years a couple of notable achievements have been made with optical dipole traps. Those include the investigation of quantum-degenerate gases [19, 20], quantum simulation of many-body systems in optical lattices [21], long-lived quantum memories for light [22] and optical frequency standards as well as precision spectroscopy [23]. Optical dipole traps that are able to confine a single atom or a few atoms to a small volume are usually referred to as optical microtraps. They provide a strong spatial confinement for laser-cooled atoms and can be realized, e.g., with strongly focused light beams [24, 25] or in the near fields of optical nanoscale waveguides as well as photonic nanostructures. Such devices have been utilized recently to, among others, study Rydberg interactions [26, 27] or investigate collisional entangling dynamics between two atoms [28]. A possibility to create optical microtraps in the near field of waveguides is to use tapered optical fibers. They offer a strong transverse confinement of the fiber-guided light over the full length of the taper section and, thus, allow a homogeneous and efficient coupling to ensembles of trapped atoms [29, 30]. Due to the interaction of the atoms with the trapping light fields, the energy states of the atom experience a shift that depends on the considered internal state as well as the motional state. In conjunction with the atoms being in a thermal state, i.e., many motional states are populated, this leads to an inhomogeneous broadening of the transitions, resulting in reduced coherence times. The latter can be a limiting factor considering the duration for which light pulses or photons can be stored using an EIT scheme. To reduce the effect of decoherence, it is beneficial to prepare the atoms in a defined motional state, e.g., by cooling them to the motional ground state.

In this thesis, I demonstrate that EIT can be implemented using laser-cooled atoms, that are trapped in the evanescent field surrounding an optical nanofiber, with fiber-guided probing and control light fields. In addition, I show experimental results indicating the reduction of the group velocity of a fiber-guided light pulse as well as storage and retrieval at the single photon level [31]. Moreover, I demonstrate how one can take advantage of confinement-induced fictitious magnetic fields, enabling the coupling of the nanofiber-trapped atom's motional state with their internal hyperfine states. I present recorded microwave spectra, used to infer the

temperature of the atoms as well as the trap parameters. I show, that the microwave coupling of the motional quantum states can be tuned by controlling the state-dependent displacement of the trapping potential, either by means of homogeneous magnetic field or by additional fiber-guided light fields. Lastly, I present experimental data for the implementation of microwave sideband cooling, which is used in order to reduce the mean number of motional quanta to a value close to the motional ground state [32].

The structure of this thesis is as follows: In Ch. 2, I introduce optical fibers with a sub-wavelength diameter, here referred to as optical nanofibers, and describe their production process. I give a brief overview of how to derive the mode profile function of the fundamental mode guided in the nanofiber and explain the polarization properties in the evanescent field surrounding the nanofiber. In Ch. 3, I discuss the interaction between the nanofiber-guided light field and the neutral Cesium atoms that allow one to realize an optical two-color dipole trap. Furthermore, I motivate how this interaction leads to the existence of fictitious magnetic fields in the vicinity of the nanofiber and give examples of the effects they can have on the nanofiber-trapped atoms. Chapter 4 contains the experimental setup, explaining all components necessary for the realization of the presented experiments. In Ch. 5, I give a brief description of EIT. Moreover, I discuss how it can be utilized in the presented setup, to slow down a nanofiber-guided light pulse and, eventually, store it within the nanofiber-trapped ensemble of neutral Cesium atoms. At last, in Ch. 6, I describe how one can take advantage of the gradients of the fictitious magnetic field to achieve coupling of the motional state of the nanofiber-trapped atoms to their internal hyperfine states using microwave transitions. I detail how one can infer the temperature of the atomic ensemble in this system and give examples of how the aforementioned coupling can be tuned and used to reduce the mean number of motional quanta in the direction of the fictitious field gradient.

Optical nanofibers

Nowadays, glass fibers are indispensable for modern communication technology as they form the backbone of the worldwide communication network. They are necessary to transport light over vast distances with only very little losses. Their working principle is rather simple, as it is solely based on total internal reflection. Here, the light is reflected off the interface between the silica fiber and the surrounding medium, which must have a lower refractive index. In order to protect the optical fibers, e.g., against pollution, they consist of two layers, namely core and cladding. The majority of the light is confined inside the core and the surrounding cladding, which is usually silica as well, has a lower refractive index. By carefully dimensioning core and cladding and adding dopants to either of them, optical fibers can be tailored to guide light in a wide range of wavelengths with losses as low as $0.2\,\mathrm{dB/km}$.

While the cladding protects the fiber-guided light from environmental influences, it also prevents access to the evanescent field, that extends outside of the fiber core. To allow interactions between a fiber-guided light field and cold atoms access to this evanescent field is required. To this end, the diameter of the optical fiber is reduced down to a diameter comparable to the wavelength of the guided light for a small section of several millimeters in length.

The first section of this chapter will elucidate the process of producing an optical nanofiber out of a standard optical fiber. It will be followed by a short overview regarding the derivation of a model to describe nanofiber-guided electromagnetic modes. At the end, a description of the properties and features of evanescent fields around optical nanofibers will be given.

2.1 Tapered optical fibers

Optical nanofibers are granting access to the evanescent field of a fiber-guided light field. They have to fulfill a couple of requirements [33]. One of them is the need for a uniform diameter on the order of the guided field's wavelength over the whole taper section. In addition, the coupling of the light field into the nanofiber should be efficient to be able to interface the trapped atoms with negligible losses. To achieve this, the nanofiber is realized as the waist of a tapered optical
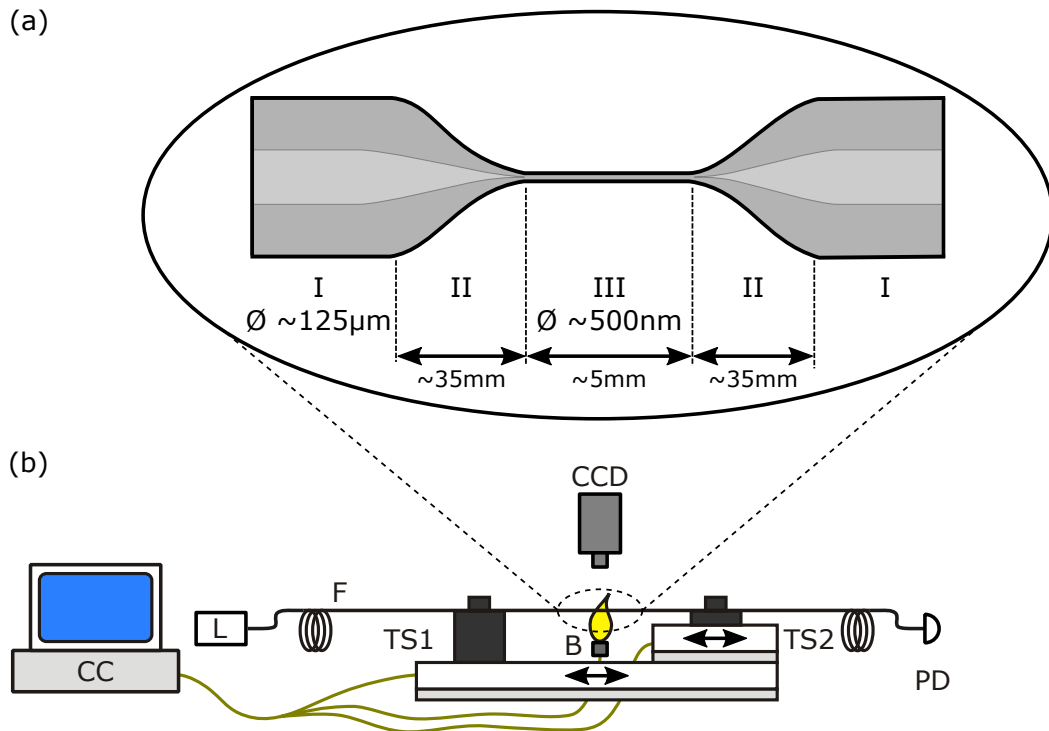
(a)

(b)

Figure 2.1: (a) Sketch of the tapered optical fiber. The darker gray area indicates the cladding and the light gray area the core of the fiber. Section I is the standard optical fiber. Section II is the taper region, where the fiber diameter is adiabatically reduced. Here the fiber-guided light field is transferred from core guided to cladding guided. Section III is the waist section with a diameter of $500\,\text{nm}$. (b) Sketch of the fiber pulling rig. The fiber (F) is mounted onto two translation stages (TS), which can be moved along the same axis and allow to move the fiber (TS1) and to stretch it (TS2). A burner (B) is used to heat up the fiber via a hydrogen-oxygen flame. A control computer (CC) is used to operate the TS and B. Using a CCD camera the fiber diameter can be monitored. The laser (L) and the photodiode (PD) allow measuring the nanofiber transmission.

fiber (TOF) in this group. A schematic of the fiber radius profile is shown in Fig. 2.1(a). Starting from the unprocessed part (I) the fiber diameter is adiabatically reduced in the taper section (II) to a diameter of about $500\,\text{nm}$. This diameter is kept for about $5\,\text{mm}$ (III), before the diameter is adiabatically increased again until it merges with the unprocessed fiber. It is critical, that the taper transition is shaped such that the fiber guided light field is adiabatically transferred from the core guided mode to the cladding guided mode [34] and vice versa. At first the light field is compressed due to the shrinking fiber diameter. Once the core diameter is smaller than the wavelength of the light field, the latter expands and leaves the core. It is then solely guided by the cladding [35]. In the waist section of the nanofiber the evanescent field extends into the surrounding vacuum. After propagating through the waist section the process is reversed

and the light field is guided by the standard fiber core. For a well designed taper transition the transmission through the nanofiber can be 99 % [36] or even more [37].

In this group the nanofibers are produced on a custom-made fiber pulling rig in a heat and pull process. A sketch of the device is shown in Fig. 2.1(b) [33, 38]. The fiber is mounted on two stacked high precision translation stages that can move along one common axis. A hydrogen-oxygen flame is used to heat the fiber, while the bottom translation stage (TS1) is used to move the fiber over the flame to uniformly heat the silica. During this oscillatory movement the fiber is stretched and therefore thinned by moving the second translation stage (TS2) in a well defined manner. The translation stages and the burner are controlled by a computer system, enabling precise and reproducible production of the nanofibers [39]. After the pulling process is complete the fiber is fixed onto an aluminum mount. To maintain the high transmission through the nanofiber a dust-free environment is essential. Without dust particles that stick to the fiber and act as scatterers, the maximum optical power that can be safely guided can be as high as $100\,\mathrm{mW}$ [40], even in vacuum. Since the optical powers required for our purposes are in the range of several ten mW, the capability to safely transmit such relatively high powers is of importance for our experiment.

2.2   Nanofiber-guided modes

The propagation of electromagnetic waves in optical fibers is well understood [41, 42]. In this section a brief overview regarding the eigenmodes of an electromagnetic field propagating through a cylindrical step index optical fiber will be given. The complete and more extensive derivation can be found in [42].

The electric (E) and magnetic (H) fields, respectively, propagating inside a cylindrically symmetric waveguide along the fiber axis can be calculated by solving the wave equation

$$\Delta \mathbf{E} - \mu\epsilon(r)\frac{\partial^2 \mathbf{E}}{\partial t^2} = -\boldsymbol{\nabla}\left(\frac{1}{\epsilon(r)}\mathbf{E}\cdot\boldsymbol{\nabla}\epsilon(r)\right) \tag{2.1}$$

$$\Delta \mathbf{H} - \mu\epsilon(r)\frac{\partial^2 \mathbf{H}}{\partial t^2} = 0 \tag{2.2}$$

that can be derived from Maxwell's equations. Here μ is the vacuum permeability, $\epsilon(r)$ the permittivity of the medium, r the radial coordinate and Δ the Laplace operator which is given by

$$\Delta = \partial_r^2 + \frac{1}{r}\partial_r + \frac{1}{r^2}\partial_\phi^2 + \partial_z^2, \tag{2.3}$$

in cylindrical coordinates. For a cylindrical symmetric waveguide the variation of the permittivity ($\boldsymbol{\nabla}\epsilon(r)$) can be neglected, resulting in the right hand side of Eq. 2.1 to vanish. The solutions of the wave equation are of the form

$$\mathbf{E}(\mathbf{r},t) = \boldsymbol{\mathcal{E}}(r,\phi)\exp(i(\omega t - \beta z)) + c.c. \quad \text{and} \tag{2.4}$$

$$\mathbf{H}(\mathbf{r},t) = \boldsymbol{\mathcal{H}}(r,\phi)\exp(i(\omega t - \beta z)) + c.c., \tag{2.5}$$

7

with the envelope vectors $\mathcal{E}$ and $\mathcal{H}$, the angular frequency ω, the time t, the cylindrical coordinates r, ϕ and z as well as the propagation constant β. The transverse components $E_{r,\phi}$ and $H_{r,\phi}$ of the electric and magnetic fields, respectively, can be expressed in terms of the longitudinal components E_z and H_z using Maxwell's equations [42]. Therefore it is sufficient to solve the wave equation only for the latter. Inserting Eq. 2.4 into Eq. 2.1 one obtains, with the wavenumber $k = \mu\epsilon\omega^2$,

$$\left(\partial_r^2 + \frac{1}{r}\partial_r + \frac{1}{r^2}\partial_\phi^2 + (k^2 - \beta^2)\right)\left(\begin{array}{c} E_z(\mathbf{r}, t) \\ H_z(\mathbf{r}, t) \end{array}\right) = 0. \tag{2.6}$$

Separating Eq. 2.6 in r and ϕ, with solutions

$$\left(\begin{array}{c} E_z(r, \phi) \\ H_z(r, \phi) \end{array}\right) = \left(\begin{array}{c} E_z(r) \\ H_z(r) \end{array}\right)\exp(\pm il\phi), \tag{2.7}$$

it can be simplified to

$$\left(\partial_r^2 + \frac{1}{r}\partial_r + (k^2 - \beta^2 - l^2/r^2)\right)\left(\begin{array}{c} E_z(r, t) \\ H_z(r, t) \end{array}\right) = 0. \tag{2.8}$$

The variable l can be seen as a parameter similar to the orbital angular momentum quantum number of an electron in an azimuthally symmetric potential [42]. The sign of the exponent can be interpreted as describing the sense of rotation (clockwise or counter-clockwise) with respect to the direction of propagation.

Equation 2.8 is the Bessel differential equation, with the solution depending on the sign of $k^2 - \beta^2$. In a step index fiber the refractive index in the core (n_1) is higher than in the cladding (n_2). A fiber guided mode is lossless if its propagation constant β is within the range of $n_1 k_0 > \beta > n_2 k_0$, with $k_0 = \omega/c$. In the core $k^2 - \beta^2 = h_1^2 > 0$, thus, Eq. 2.8 is solved by
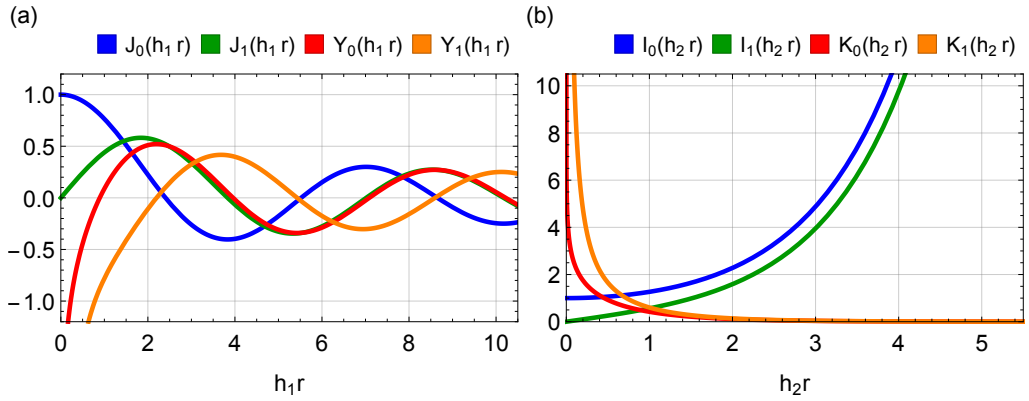

Figure 2.2: (a) Bessel functions $J_0(h_1 r)$, $J_1(h_1 r)$ in blue and green as well as $Y_0(h_1 r)$, $Y_1(h_1 r)$ in red and orange, respectively. (b) Modified Bessel functions $I_0(h_2 r)$, $I_1(h_2 r)$ in blue and green as well as $K_0(h_2 r)$, $K_1(h_2 r)$ in red and orange, respectively.

a linear combination of the Bessel functions of the first ($J_l(h_1 r)$) and second ($Y_l(h_1 r)$) kind

$$\psi(r) = c_1 J_l(h_1 r) + c_2 Y_l(h_1 r). \tag{2.9}$$

In the cladding $\beta^2 - k^2 = h_2 > 0$, with Eq. 2.8 solved similarly by a linear combination of the modified Bessel functions of the first ($I_l(h_2 r)$) and second ($K_l(h_2 r)$) kind

$$\psi(r) = d_1 I_l(h_2 r) + d_2 K_l(h_2 r). \tag{2.10}$$

Figure 2.2(a) shows the Bessel functions $J_l(h_1 r)$ and $Y_l(h_1 r)$ of order $l = \{1, 2\}$. One can observe, that $Y_l(h_1 r)$ diverges for r approaching zero. To prevent the fields in the core from diverging, c_2 is set to zero and only the $J_l(h_1 r)$ are considered, giving

$$\begin{pmatrix} E_z(\mathbf{r}, t) \\ H_z(\mathbf{r}, t) \end{pmatrix} = \begin{pmatrix} A \\ B \end{pmatrix} J_l(h_1 r) \exp\left(i(\omega t \pm l\phi - \beta z)\right). \tag{2.11}$$

In Fig. 2.2(b) the modified Bessel functions $I_l(h_2 r)$ and $K_l(h_2 r)$ are depicted. Here $I_l(h_2 r)$ diverges for $h_2 r$ approaching ∞, while $K_l(h_2 r)$ diverges for $r \to 0$. In order to have a decaying evanescent field the divergence at $r \to \infty$ has to be avoided, thus $d_1 = 0$ and only the $K_l(h_2 r)$ are considered, resulting in

$$\begin{pmatrix} E_z(\mathbf{r}, t) \\ H_z(\mathbf{r}, t) \end{pmatrix} = \begin{pmatrix} C \\ D \end{pmatrix} K_l(h_2 r) \exp\left(i(\omega t \pm l\phi - \beta z)\right). \tag{2.12}$$

The coefficients A, B, C and D, determining the strength of the field components, as well as β can be calculated by considering the boundary conditions for the fields. The electric field components that are parallel to the interface between n_1 and n_2 have to be continuous at the radial position of the interface $r = a$ [43] and the same holds true for the magnetic field components that are orthogonal to the interface. With this a set of four relations can be derived, yielding a nontrivial solution for the coefficients. Using the acquired solution one can determine the propagation constant β by writing down the mode condition [42]

$$\frac{J_l'(h_1 a)}{J_l(h_1 a) h_1 a} = -\frac{n_1^2 + n_2^1}{2n_1^2} \frac{K_l'(h_2 a)}{K_l(h_2 a) h_2 a}$$

$$\pm \sqrt{\left(\frac{n_1^2 - n_2^1}{2n_1^2}\right)^2 \left(\frac{K_l'(h_2 a)}{K_l(h_2 a) h_2 a}\right)^2 + \frac{l^2 \beta^2}{n_1^2 k^2} \left(\frac{1}{h_2^2 a^2} + \frac{1}{h_1^2 a^2}\right)^2}. \tag{2.13}$$

Rearranging the above equation one gets a set of two equations, that can be assigned to the hybrid modes EH and HE

$$\frac{J_{l+1}(h_1 a)}{J_l(h_1 a) h_1 a} = \frac{n_1^2 + n_2^1}{2n_1^2} \frac{K_l'(h_2 a)}{K_l(h_2 a) h_2 a} + \frac{l}{h_1^2 a^2} - \sqrt{\cdots} \tag{2.14}$$

$$\frac{J_{l-1}(h_1 a)}{J_l(h_1 a) h_1 a} = -\frac{n_1^2 + n_2^1}{2n_1^2} \frac{K_l'(h_2 a)}{K_l(h_2 a) h_2 a} + \frac{l}{h_1^2 a^2} - \sqrt{\cdots}, \tag{2.15}$$

respectively. The square root $\sqrt{\cdots}$ in Eq. 2.14 and in Eq. 2.15 represents the square root in Eq. 2.13. The transcendental equations can be solved either numerically or graphically. In the

special case of $l = 0$ one can find solutions for the above mode equations where only three out of six field components are not zero. For Eq. 2.14 all field components except for H_r, H_z and E_ϕ are zero, consequently the electric field varies only in the transverse plane. This mode is referred to as transversely electric TE_{lm}, where $l = 0$ and $m \in \mathbb{N}$ are the different mode solutions. Similarly for Eq. 2.15 all field components apart from E_r, E_z and H_ϕ vanish for $l = 0$. The mode is referred to as transversely magnetic TM_{lm} since the magnetic field has only transverse components.

As discussed earlier in this chapter we use an optical nanofiber with a diameter of $500\,\mathrm{nm}$ to have access to a strong evanescent field. In the nanofiber the light is guided due to total internal reflection at the interface between fused silica ($n_1 = 1.4525$) and vacuum ($n_2 = 1$). The nanofiber is only capable of guiding the fundamental mode HE_{11} for light fields in the wavelength range used in this experiment. To be able to calculate the fields of the fundamental mode in the nanofiber the electric field amplitude A has to be determined. This can be done by using the relation of A to the total power P of the electromagnetic field propagating in the fiber via the Pointing vector $\mathcal{P} = 1/2\,\mathrm{Re}(\mathbf{E} \times \mathbf{H}^*)$, reading [44]

$$A = \sqrt{\frac{\beta P}{\pi a^2 \omega \epsilon}} \frac{1}{\sqrt{D_{\mathrm{in}} + D_{\mathrm{out}}}}. \tag{2.16}$$

Here D_{in} and D_{out} are proportional to the fractions of the light field's power traveling inside and outside the nanofiber [44, 45]

$$
\begin{aligned}
D_{\mathrm{in}} &= n_1^2 \frac{h_2^2 K_1^2(h_2 a)}{h_1^2 J_1^2(h_1 a)} \Big[(1-s)(1-s_1) \left(J_0^2(h_1 a) + J_1^2(h_1 a) \right) \\
&+ (1+s)(1+s_1) \left(J_2^2(h_1 a) - J_1(h_1 a) J_3(h_1 a) \right) \Big] \\
D_{\mathrm{out}} &= n_2^2 \Big[(1-s)(1-s_2) \left(K_1^2(h_2 a) - K_0^2(h_2 a) \right) \\
&+ (1+s)(1+s_2) \left(K_1(h_2 a) K_3(h_2 a) - K_2^2(h_2 a) \right) \Big],
\end{aligned}
$$

$$\tag{2.17}$$
$$\tag{2.18}$$

with

$$
\begin{aligned}
s &= \left(\frac{1}{h_2^2 a^2} + \frac{1}{h_1^2 a^2} \right) \left(\frac{J_1'(h_1 a)}{h_1 a J_1(h_1 a)} + \frac{K_1'(h_2 a)}{h_2 a K_1(h_2 a)} \right)^{-1} \\
s_1 &= s \frac{\beta^2}{k_0^2 n_1^2} \\
s_2 &= s \frac{\beta^2}{k_0^2 n_2^2}.
\end{aligned}
$$

$$\tag{2.19}$$

Having calculated the field amplitude one can write down the envelope vectors $\mathcal{E}(\mathbf{r})$ and $\mathcal{H}(\mathbf{r})$

10

of the quasi-circularly polarized HE_{11} mode's electric and magnetic field [44, 45], respectively:

$$\mathcal{E}_r = i\frac{h_2 K_1(h_2 a)}{h_1 J_1(h_1 a)}\Big((1-s)J_0(h_1 r) - (1+s)J_2(h_1 r)\Big) \tag{2.20}$$

$$\mathcal{E}_\phi = -\frac{h_2 K_1(h_2 a)}{h_1 J_1(h_1 a)}\Big((1-s)J_0(h_1 r) - (1+s)J_2(h_1 r)\Big) \tag{2.21}$$

$$\mathcal{E}_z = \frac{2h_2 K_1(h_2 a)}{\beta J_1(h_1 a)}J_1(h_1 r) \tag{2.22}$$

$$\mathcal{H}_r = \frac{\omega\,\epsilon_0\,n_1^2\,h_2 K_1(h_2 a)}{\beta h_1 J_1(h_1 a)}\Big((1-s_1)J_0(h_1 r) - (1+s_1)J_2(h_1 r)\Big) \tag{2.23}$$

$$\mathcal{H}_\phi = i\frac{\omega\,\epsilon_0\,n_1^2\,h_2 K_1(h_2 a)}{\beta h_1 J_1(h_1 a)}\Big((1-s_1)J_0(h_1 r) - (1+s_1)J_2(h_1 r)\Big) \tag{2.24}$$

$$\mathcal{H}_z = is\frac{2h_2 K_1(h_2 a)}{\omega\mu J_1(h_1 a)}J_1(h_1 r) \tag{2.25}$$

inside the fiber and

$$\mathcal{E}_r = i\Big((1-s)K_0(h_2 r) - (1+s)K_2(h_2 r)\Big) \tag{2.26}$$

$$\mathcal{E}_\phi = -\Big((1-s)K_0(h_2 r) + (1+s)K_2(h_2 r)\Big) \tag{2.27}$$

$$\mathcal{E}_z = \frac{2h_2 K_1(h_2 r)}{\beta} \tag{2.28}$$

$$\mathcal{H}_r = \frac{\omega\,\epsilon_0\,n_2^2}{\beta}\Big((1-s_2)K_0(h_2 r) - (1+s_2)K_2(h_2 r)\Big) \tag{2.29}$$

$$\mathcal{H}_\phi = i\frac{\omega\,\epsilon_0\,n_2^2}{\beta}\Big((1-s_2)K_0(h_2 r) - (1+s_2)K_2(h_2 r)\Big) \tag{2.30}$$

$$\mathcal{H}_z = is\frac{2h_2 K_1(h_2 r)}{\omega\mu} \tag{2.31}$$

outside of the fiber. The electric and magnetic field for a quasi-linearly polarized fundamental mode can be obtained by calculating the linear superposition of the clockwise and counter-clockwise circularly polarized fields. They read [45]

$$\mathbf{E}(r,\phi,z) = \sqrt{2}A\begin{pmatrix}\mathcal{E}_r\cos(\phi-\varphi_0)\\ i\mathcal{E}_\phi\sin(\phi-\varphi_0)\\ \pm\mathcal{E}_z\cos(\phi-\varphi_0)\end{pmatrix}\exp\Big(i(\pm\beta z-\omega t)\Big) \tag{2.32}$$

$$\mathbf{H}(r,\phi,z) = \sqrt{2}A\begin{pmatrix}i\mathcal{H}_r\sin(\phi-\varphi_0)\\ \mathcal{H}_\phi\cos(\phi-\varphi_0)\\ \pm i\mathcal{H}_z\sin(\phi-\varphi_0)\end{pmatrix}\exp\Big(i(\pm\beta z-\omega t)\Big) \tag{2.33}$$

where φ_0 denotes the orientation of the transverse field component with respect to the x-axis and the $\pm$ accounts for the propagation direction along the fiber axis $\pm z$. The real part of the

electric field is depicted as a vector plot in Fig. 2.3, where (a) depicts the field in the $x-y$ plane and (b) in the $x-z$ plane. The normalized intensity of the evanescent field is shown color-coded in the background. The gray disk (a) or rectangle (b), respectively, represents the nanofiber. The red double arrow indicates the main polarization axis of the light field in the transverse plane of the fiber. In this example $\varphi_0 = 0$, meaning the polarization is oriented along the x-axis. The plot in (a) shows, that the field also has a component along y for $x, y \neq 0$. With time progressing the orientation of the x and y component oscillates between positive and negative direction. The intensity does not only decay in radial direction, it also varies in azimuthal direction. At $y = 0$ the intensity is at its relative maximum and decreases along ϕ for a fixed radial position, with the minimum at $\phi = \pm\pi/2$. From Fig. 2.3(b) one finds, that the field has a strong z component depending on the axial position for a fixed point in time. When letting time evolve and fixing the axial position z one can observe that the electric field vector rotates, clockwise on the right side of the fiber and counter-clockwise on the left side of the fiber, for propagation along positive z and looking along negative y onto the $x-z$ plane. If the direction of propagation is changed the sign of the circularity also changes, meaning that the electric field vector rotates counter-clockwise on the right side of the fiber and vice versa on the left side of the fiber. Here the intensity is uniform along the fiber axis.
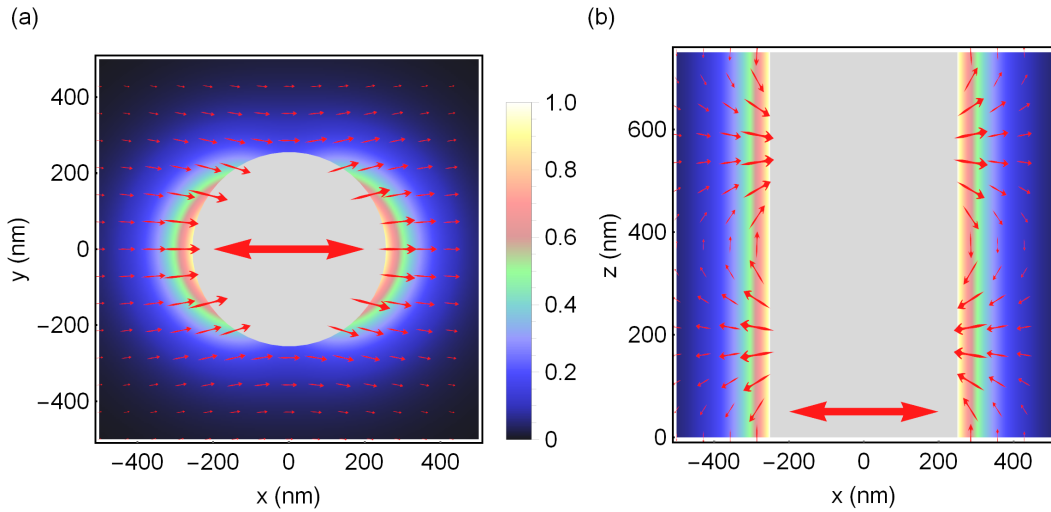
Figure 2.3: Evanescent field in the vicinity of the nanofiber. The red arrows indicate the real part of the electric field of the fundamental mode at a given point in time plotted in the (a) x–y and (b) x–z plane, respectively. The double arrow indicates the main polarization axis of the nanofiber-guided light field. The gray (a) circle and (b) rectangle, respectively, represents the nanofiber. The colored density plot in the background shows the intensity of the evanescent field normalized to its value at the fiber surface, with white showing high intensity. For the calculation a nanofiber with diameter $a = 250\,\mathrm{nm}$, $n_1 = 1.45247$ and a light field with wavelength $\lambda = 852\,\mathrm{nm}$ was assumed.

2.2.1 Polarization properties of the evanescent field of optical nanofibers

As already indicated by the behavior of the electric field in the vicinity of the nanofiber, the nanofiber-guided light has extraordinary polarization properties. Knowledge of these properties is crucial to fully understand the interaction between the fiber-guided light fields and the nanofiber trapped atoms, as it influences which optical transition can be driven. A convenient formalism to describe the polarization is to express the electric fields in terms of spherical tensor components. Here three basis vectors $\mathbf{e}_{\pm 1}$ and $\mathbf{e}_0$ describe the light field components that are $\sigma^{\pm}$ and π-polarized, respectively. Without loss of generality the quantization axis can be chosen to be along an applied external magnetic field, oriented along, e.g., the y-axis. The new basis vectors can then be expressed by Cartesian coordinates as [44]

$$\mathbf{e}_{\pm 1} = \mp 1/\sqrt{2}\big(\mathbf{e}_z \pm i\mathbf{e}_x\big), \quad \mathbf{e}_0 = \mathbf{e}_y. \tag{2.34}$$

In this new basis the positive frequency envelope $\boldsymbol{\mathcal{E}}$ of the electric field can then be written as [44]

$$\boldsymbol{\mathcal{E}} = \sum_q \big(-1\big)^q \mathcal{E}_q \mathbf{e}_{-q}, \text{ with } q = -1, 0, 1. \tag{2.35}$$

The $\mathcal{E}_q$ relate to their Cartesian representation in the same manner as the $\mathbf{e}_q$

$$\mathcal{E}_{\pm 1} = \mp 1/\sqrt{2}\big(\mathcal{E}_z \pm i\mathcal{E}_x\big), \quad \mathcal{E}_0 = \mathcal{E}_y. \tag{2.36}$$

One has to pay attention to the changed representation of the polarization, as $\mathcal{E}_{+1}$ ($\mathcal{E}_{-1}$) expresses σ_- (σ_+) polarized light. Figure 2.4 shows the spherical tensor components of the electric field [45]. All plots show a transverse cut through the fiber with the nanofiber depicted as a gray disk. The main polarization axis is indicated by the red double arrow in the center of the plot. For the calculations a nanofiber with radius $a = 250\,\text{nm}$ guiding a light field with a wavelength $\lambda = 852\,\text{nm}$ was assumed. The light field propagates along z, where $+z$ points out of the plane towards the reader. The atoms are trapped at $y = 0\,\text{nm}$ and $|x| > 250\,\text{nm}$, which defines the main region of interest for this discussion. The quantization axis is chosen to be along $+y$. In Fig. 2.4(a) the $\mathcal{E}_{-1}$ ($\mathcal{E}_{+1}$)-component is plotted for a main polarization axis oriented parallel to the x-axis and light propagating along $+z$ ($-z$). As mentioned before, this corresponds to the fraction of σ^+ (σ^-) polarized light. On can directly see that the majority of the evanescent field on the right side of the fiber is σ^+ (σ^-) polarized. Figure 2.4(b) depicts the $\mathcal{E}_{+1}$ ($\mathcal{E}_{-1}$)-component for a main polarization axis oriented parallel to the x-axis and light propagating along $+z$ ($-z$). This corresponds to the fraction of σ^- (σ^+) polarized light of this mode in the vicinity of the nanofiber. Here, the majority of the evanescent field on the left side of the fiber is σ^- (σ^+) polarized. In both cases the fraction of π-polarized light is negligible and the circularity reaches its peak value of 93 % at the fiber surface at $y = 0\,\text{nm}$. The remaining 7 % can be attributed to circular polarization with the opposite circularity. When the main polarization axis is oriented parallel to the y-axis this changes, as illustrated in Fig. 2.4(c). Here the $\mathcal{E}_0$ component is plotted, indicating that the evanescent field is fully π-polarized at $y = 0\,\text{nm}$ on both sides of the fiber. This behavior is independent of the propagation direction of the fiber-guided light field.
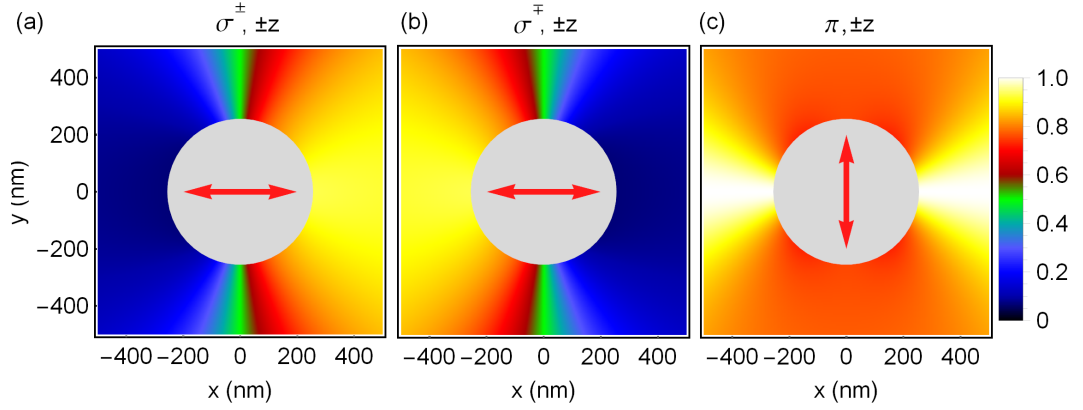
Figure 2.4: The double arrow indicates the main polarization axis of the nanofiber-guided light field. The gray disk represents the nanofiber. The colored density plot shows the square of the spherical tensor components of the electric field (a) $\mathcal{E}_{\mp 1}$, (b) $\mathcal{E}_{\pm 1}$ and (c) $\mathcal{E}_0$, respectively, normalized to $\mathcal{E}^2$. For a light field propagating in positive z direction (out of the frame) this corresponds to σ^+, σ^- and π respectively, considering a quantization axis along $+y$. Inverting the direction of propagation ($+z \rightarrow -z$) flips the sign of the circular polarization. For the calculation the same parameters as in Fig 2.3 were assumed.

This shows that the choice of the orientation of the linear polarization, as well as the propagation direction, influences which optical transitions can be driven. Depending on the driven transitions this can, e.g., lead to optical pumping of the trapped atoms [46].

Nanofiber-mediated atom-light interaction

The optical nanofiber presented in the previous chapter allows accessing the evanescent part of a nanofiber-guided light field. Thus, atoms that are in the vicinity of the nanofiber can couple to this evanescent field enabling investigations of nanofiber-trapped atoms. While a waveguide is not required to couple atoms to a light field, they have the considerable advantage of uniform coupling over the whole length of the waveguide.

To keep the atoms in a close and defined distance to the nanofiber surface they have to be confined in a trapping potential. The first section of this chapter will explain the mechanisms required for trapping the atoms close to the nanofiber surface. This will be followed by a short explanation of the techniques used to create a three-dimensional trapping potential. The last part of this chapter will focus on the existence of fictitious magnetic fields and their effect on the eigenstates of the trapped atoms.

3.1   Hyperfine interaction, AC Stark shift and Zeeman shift

Most quantum optics experiments working with neutral atoms use alkali atoms because of their advantageous properties. Their electronic transitions are usually in the near infrared, they feature a simple hydrogen-like level scheme and they offer closed transitions. The latter is an important feature for cooling, trapping and manipulating alkali atoms with optical fields. The shells of alkali atoms are fully occupied, with one valence electron in the outermost shell. As the closed shells do not contribute to the angular momentum, both the spin- and the orbital angular momentum, $\mathbf{S}$ and $\mathbf{L}$, respectively, are set by the single valence electron. The coupling between $\mathbf{S}$ and $\mathbf{L}$, referred to as spin-orbit coupling, is responsible for the fine structure of the atomic energy levels. Here the energy depends on the quantum number $\mathbf{J} = \mathbf{L} + \mathbf{S}$, ranging from $J = |L - S|$ to $J = L + S$. Due to the coupling between the total angular momentum $\mathbf{J}$ of the electron and the
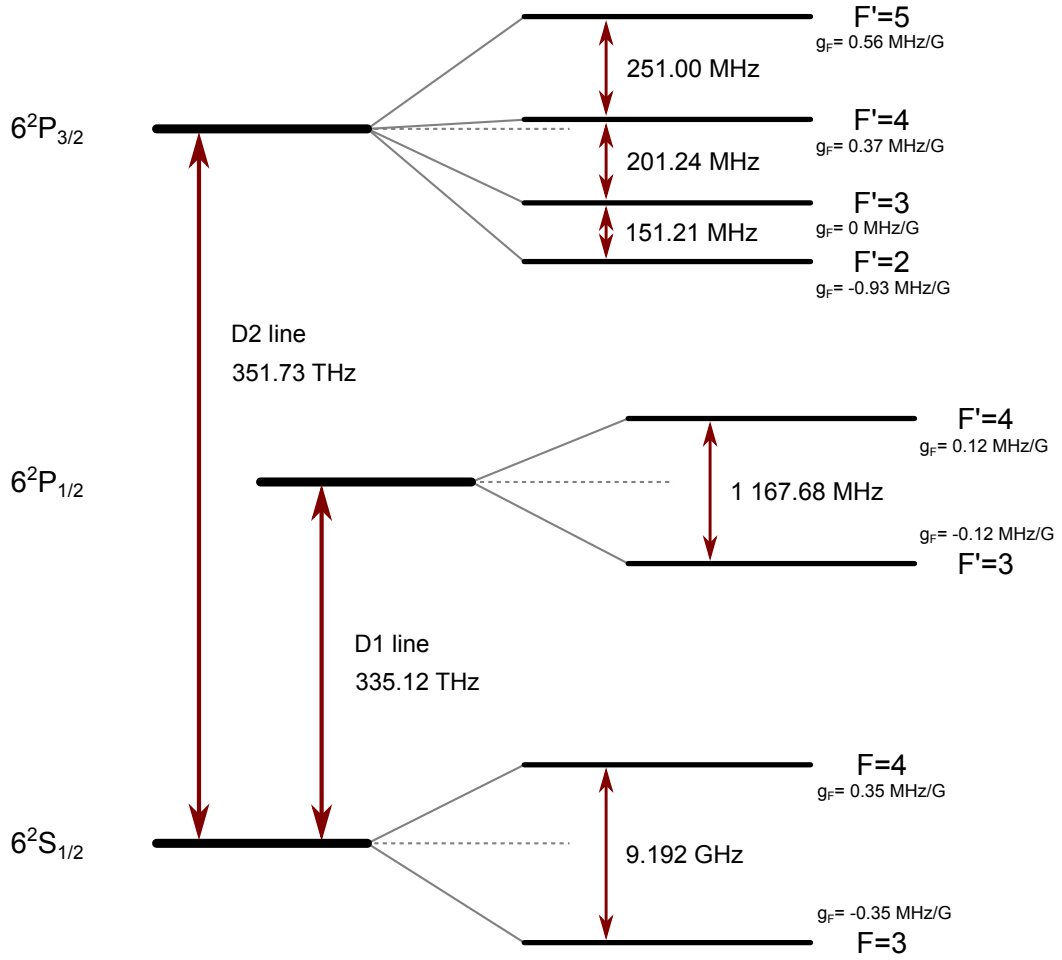
Figure 3.1: Level scheme of the D1 and D2 line of Cesium, including the transition frequencies between the respective energy levels and the Landé g-factors in units of $\mu_\text{B}/\hbar$ with the Bohr magneton μ_B.

nuclear spin $\mathbf{I}$, there is an additional substructure in the energy levels, the hyperfine structure, where the energy depends on the total angular momentum $\mathbf{F} = \mathbf{J} + \mathbf{I}$.

The atom used in our experiments is the only stable isotope of Cesium, with an atomic mass of 133 [47]. It has a nuclear spin of $I = 7/2$ and an electronic spin $S = 1/2$. Figure 3.1 shows the level scheme of atomic Cesium for the D1 and D2 line, including the relevant transition frequencies. The values of the depicted states are taken from [48, 49]. The hyperfine splitting of the ground state is defined to be exactly of this frequency as it is used for the current definition of the second. Here the atomic states are denoted in the Russel Saunders notation

$$n^{2S+1}L_J,$$

with the principal quantum number n. The transition frequency of the D1 line corresponds

to a free space wavelength of $\lambda \approx 894.6$ nm, while the transition frequency of the D2 line corresponds to $\lambda \approx 852.3$ nm.

From Fig. 3.1 one can see, that the fine structure splitting is large with a wavelength difference of about 42 nm. The hyperfine splittings, on the other hand, are several orders of magnitude smaller. The Hamiltonian describing the hyperfine structure reads [47, 50]

$$H_{\text{hfs}} = A_{\text{hfs}}\mathbf{I} \cdot \mathbf{J} + B_{\text{hfs}}\frac{3(\mathbf{I} \cdot \mathbf{J})^2 + \frac{3}{2}\mathbf{I} \cdot \mathbf{J} - I(I+1)J(J+1)}{2I(2I-1)J(2J-1)}, \tag{3.1}$$

leading to an energy shift of

$$\Delta E_{\text{hfs}} = \frac{1}{2}\hbar A_{\text{hfs}}G + \hbar B_{\text{hfs}}\frac{\frac{3}{2}G(G+1) - 2I(I+1)J(J+1)}{2I(2I-1)2J(2J-1)}. \tag{3.2}$$

Here $G = F(F+1) - I(I+1) - J(J+1)$, A_{hfs} is the magnetic dipole constant and B_{hfs} is the electric quadrupole constant. The values of A_{hfs} and B_{hfs} for the different states can be found in [47–49, 51].

3.1.1 Zeeman splitting

The Zeeman effect describes the splitting of a hyperfine level into several sub-components in the presence of a static magnetic field. It was first observed by Pieter Zeeman in 1896.

Each hyperfine level denoted by F contains $2F + 1$ magnetic sublevels, labeled with the magnetic quantum number m_{F} which is the projection of $\mathbf{F}$ onto the quantization axis. It is an integer number that can take the values $-F \leq m_{\text{F}} \leq F$. Without an external magnetic field the magnetic sublevels are degenerate. Once the atoms are subject to a static magnetic offset field this degeneracy is broken and the atom-field interaction is described by the Hamiltonian

$$\begin{align}
H_{\text{B}} &= -\boldsymbol{\mu} \cdot \mathbf{B} \tag{3.3}\\
&= \frac{\mu_{\text{B}}}{\hbar}g_{\text{J}}\mathbf{J} \cdot \mathbf{B} \tag{3.4}\\
&= \frac{\mu_{\text{B}}}{\hbar}g_{\text{F}}\mathbf{F} \cdot \mathbf{B}. \tag{3.5}
\end{align}$$

Here μ is the magnetic moment, μ_{B} is the Bohr magneton and $g_{J,F}$ are the Landé g-factors for the respective quantum number J or F. The values of the Landé factors have been measured and can be found in [47, 52, 53]. Equation 3.4 holds true if the magnetic field induced energy shift is small compared to the fine structure splitting. Similarly, Eq. 3.5 is valid if the energy shift caused by the magnetic field is small compared to the hyperfine energy splitting. In this case, H_{B} can be treated as a perturbation of H_{hfs}, yielding for the energy shift [54]

$$\Delta E_{\text{B}} = \mu_{\text{B}}\, g_{\text{F}}\, m_{\text{F}}, \tag{3.6}$$

if the direction of the magnetic field is taken as the quantization axis. The Landé g-factor g_{F} is given by [50]

$$g_{\text{F}} = g_{\text{J}}\frac{F(F+1) + J(J+1) - I(I+1)}{2F(F+1)}, \tag{3.7}$$

where

$$g_J = g_L \frac{J(J+1) + L(L+1) - S(S+1)}{2J(J+1)} + g_S \frac{J(J+1) + S(S+1) - L(L+1)}{2J(J+1)} 2J(J+1),$$

(3.8)

with the electronic orbital and spin g-factors $g_L \approx 1$ and $g_S \approx 2$, respectively. The value for g_F, given as the energy shift per Gauss and m_F level, can be found in Fig. 3.1.

3.1.2 AC Stark shift

The Stark effect, named after Johannes Stark who discovered it in 1914, describes the shift and splitting of the spectral lines of an atom caused by an electric field. In the case of a static electric field the interaction is referred to as DC Stark effect, whereas for alternating fields, e.g. optical fields, the effect is called AC Stark effect. The following derivation of the AC Stark interaction closely follows [50].

The classical light field considered here is of the form

$$\mathbf{E} = \frac{1}{2}\boldsymbol{\mathcal{E}} \exp\left(-i\omega t\right) + \text{c.c.},$$

(3.9)

where $\boldsymbol{\mathcal{E}} = \mathcal{E}\mathbf{e}$ is the electric field envelope, with amplitude $\mathcal{E}$ and field vector $\mathbf{e}$. Furthermore ω is the angular frequency of the electric field and c.c. is the abbreviation for complex conjugate. The operator describing the interaction between the light field and the atom in the dipole approximation is given by [50]

$$V_E = -\mathbf{E} \cdot \mathbf{d} = -\frac{1}{2}\mathcal{E}\mathbf{e} \cdot \mathbf{d} \exp\left(-i\omega t\right) - \text{c.c.},$$

(3.10)

with $\mathbf{d}$ being the operator for the electric dipole of the atom. Here we only consider light fields that are far detuned from resonance and result in a small shift of the eigenenergies compared to the fine structure splitting. The latter results in J being a good quantum number. The energy shift δE_a of the atomic state $|a\rangle$ can be calculated by treating V_E as a small perturbation. By applying second order perturbation theory the energy shift reads

$$\delta E_a = -\frac{|\mathcal{E}|^2}{4\hbar} \sum_b \text{Re}\left(\frac{|\langle b| \mathbf{e} \cdot \mathbf{d} |a\rangle|^2}{\omega_b - \omega_a - \omega - i\gamma_{ba}/2} + \frac{|\langle a| \mathbf{e} \cdot \mathbf{d} |b\rangle|^2}{\omega_b - \omega_a + \omega + i\gamma_{ba}/2} \right),$$

(3.11)

where $|a\rangle$ and $|b\rangle$ are atomic eigenstates with eigenenergies $\hbar\omega_a$ and $\hbar\omega_b$, respectively. The parameter $\gamma_{ba} = \gamma_a + \gamma_b$ gives the linewidth of the transition with the spontaneous decay rates γ_a and γ_b. The energy shift in Eq. 3.11 can be seen as an expectation value $\delta E_a = \langle a| V_{EE} |a\rangle$, with the operator for the AC Stark interaction [50]

$$V_{EE} = \frac{|\mathcal{E}|^2}{4} \left((\mathbf{e}^* \cdot \mathbf{d}) \, \mathcal{R}_+ \, (\mathbf{e} \cdot \mathbf{d}) + (\mathbf{e} \cdot \mathbf{d}) \, \mathcal{R}_- \, (\mathbf{e}^* \cdot \mathbf{d}) \right),$$

(3.12)

and

$$\mathcal{R}_\pm = -\frac{1}{\hbar} \sum_b \text{Re}\left(\frac{1}{\omega_b - \omega_a \mp \omega \mp i\gamma_{ba}/2} \right) |b\rangle \langle b|.$$

(3.13)

This effective interaction operator V_{EE} accurately describes the level shift as well as level mixing of degenerate and non-degenerate states and its derivation can be found in [55–58].

In order to obtain the internal eigenstates and eigenenergies of a multilevel atom interacting with an external light field one has to diagonalize the interaction Hamiltonian

$$H_{\text{int}} = H_{\text{hfs}} + V_{\text{EE}}, \tag{3.14}$$

with both the hyperfine interaction H_{hfs} and the AC Stark interaction V_{EE} perturbing the atomic energy levels. By restricting oneself to a single fine structure state $|nJ\rangle$ the AC Stark interaction operator can be written in terms of the hyperfine structure basis states $|nJFm_F\rangle$ as

$$V_{\text{EE}} = \sum_{Fm_FF'm_F'} V_{Fm_FF'm_F'} |nJFm_F\rangle \langle nJF'm_F'| . \tag{3.15}$$

The matrix element $V_{Fm_FF'm_F'}$ is given by [58]

$$
\begin{aligned}
V_{Fm_FF'm_F'} &= \frac{|\mathcal{E}|^2}{4} \sum_{\substack{K=0,1,2 \\ q=-K,...,K}} \alpha_{nJ}^K \{\mathbf{e}^* \otimes \mathbf{e}\}_{Kq} (-1)^{J+I+K+q-m_F} \\
&\times \sqrt{(2F+1)(2F'+1)} \begin{pmatrix} F & K & F' \\ m_F & q & -m_F' \end{pmatrix} \begin{Bmatrix} F & K & F' \\ J & I & J \end{Bmatrix} . \tag{3.16}
\end{aligned}
$$

In Eq. 3.16, we established the reduced dynamical polarizability with its real part

$$
\begin{aligned}
\alpha_{nJ}^K &= (-1)^{K+J+1} \sqrt{2K+1} \sum_{n'J'} (-1)^{J'} \begin{Bmatrix} 1 & K & 1 \\ J & J' & J \end{Bmatrix} |\langle n'J'| |\mathbf{d}| |nJ\rangle|^2 \\
&\times \frac{1}{\hbar} \text{Re} \left(\frac{1}{\omega_{n'J'nJ} - \omega - i\gamma_{n'J'nJ}/2} + \frac{(-1)^K}{\omega_{n'J'nJ} + \omega + i\gamma_{n'J'nJ}/2} \right), \tag{3.17}
\end{aligned}
$$

as well as the Wigner 3-j symbol in the second to last and the Wigner 6-j symbol in the last expression. The compound tensor components $\{\mathbf{e}^* \otimes \mathbf{e}\}_{Kq}$ are defined as

$$\{\mathbf{e}^* \otimes \mathbf{e}\}_{Kq} = \sum_{\mu,\mu'=\pm 1} (-1)^{q+\mu'} e_\mu e_{-\mu'}^* \sqrt{2K+1} \begin{pmatrix} 1 & K & 1 \\ \mu & -q & \mu' \end{pmatrix}, \tag{3.18}$$

including the spherical tensor components e_μ of the polarization vector $\mathbf{e}$. With the newly introduced dynamical polarizability, the AC Stark interaction operator can be rewritten as

$$V_{\text{EE}} = -\frac{|\mathcal{E}|^2}{4} \left(\alpha_{nJ}^s - i\alpha_{nJ}^v \frac{(\mathbf{e}^* \times \mathbf{e}) \cdot \mathbf{J}}{2J} + \alpha_{nJ}^T \frac{3((\mathbf{e}^* \cdot \mathbf{J})(\mathbf{e} \cdot \mathbf{J}) + (\mathbf{e} \cdot \mathbf{J})(\mathbf{e}^* \cdot \mathbf{J})) - 2\mathbf{J}^2}{2J(2J-1)} \right), \tag{3.19}$$
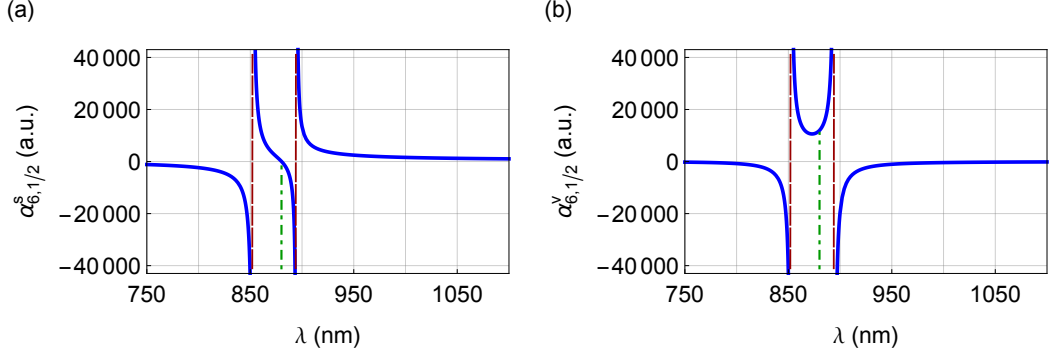
Figure 3.2: (a) Scalar ($\alpha_{6,1/2}^s$) and (b) vector ($\alpha_{6,1/2}^v$) polarizability of the $6^2S_{1/2}$ ground state of Cesium, taken from [50], versus wavelength λ. The dashed red line indicates the resonances at the D1 and D2 line transitions. The green dot-dashed line indicates the tune-out wavelength.

with the conventional dynamical scalar, vector and tensor polarizabilities $\alpha_{nJ}^s, \alpha_{nJ}^v$ and α_{nJ}^T, respectively. For an atom in the fine structure level $|nJ\rangle$ they are given by

$$
\begin{aligned}
\alpha_{nJ}^s &= \frac{1}{\sqrt{3(2J+1)}} \alpha_{nJ}^{K=0} \\
\alpha_{nJ}^v &= -\sqrt{\frac{2J}{(J+1)(2J+1)}} \alpha_{nJ}^{K=1} \\
\alpha_{nJ}^T &= -\sqrt{\frac{2J(2J-1)}{3(J+1)(2J+1)(2J+3)}} \alpha_{nJ}^{K=2}.
\end{aligned}
\tag{3.20}
$$

If the AC Stark interaction energy is small compared to the hyperfine splitting, then F is a good quantum number and the interaction operator can be written as [59]

$$
\begin{aligned}
V_{\mathrm{EE}} &= -\frac{|\mathcal{E}|^2}{4}\Bigg(\alpha_{nJF}^s - i\alpha_{nJF}^v \frac{(\mathbf{e}^* \times \mathbf{e}) \cdot \mathbf{F}}{2F} \\
&\quad + \alpha_{nJF}^T \frac{3\big((\mathbf{e}^* \cdot \mathbf{F})(\mathbf{e} \cdot \mathbf{F}) + (\mathbf{e} \cdot \mathbf{F})(\mathbf{e}^* \cdot \mathbf{F})\big) - 2\mathbf{F}^2}{2F(2F-1)} \Bigg).
\end{aligned}
\tag{3.21}
$$

The scalar part of V_{EE} in Eq. 3.21 only depends on $|\mathcal{E}|^2$ and leads to a global shift of all sublevels of a hyperfine level. The vector part only contributes for light fields which are at least partially elliptically polarized, as the cross product $(\mathbf{e}^* \times \mathbf{e})$ is zero for perfectly linear polarization. Furthermore, it is notable, that the tensor part vanishes for states with $J=1/2$, which is the case for, e.g., the ground state of Cesium and other alkali atoms.

The calculated scalar and vector parts of the dynamical polarizability are plotted in Fig. 3.2(a) and (b), respectively. The values for the transition energies and dipole matrix elements are taken from [50]. In both plots the resonances at a wavelength λ of $852\,\mathrm{nm}$ (D2 line) and $894\,\mathrm{nm}$ (D1 line) are visible, since the polarizability is discontinuous at these wavelengths. In between the

two resonances an interesting feature appears at $\lambda =$880.25 nm. At this wavelength, referred to as tune-out wavelength, the scalar part of the polarizability vanishes as the contributions of the D1 and D2 transition compensate each other. Only the vector part of the polarizability remains nonzero, with implications that will be discussed later on in this chapter.

3.2 Optical nanofiber-based two-color dipole trap

To trap the atoms close to the nanofiber and, thus, maximizing the coupling to the evanescent field while keeping the atoms from colliding with the fiber surface, we require an attractive as well as a repulsive potential acting on the atoms. The attractive potential can be realized employing a light field that is red-detuned with respect to the atomic resonance. As seen in Eq. 3.21 the AC Stark shift for a linearly polarized light field interacting with an alkaline atom depends only
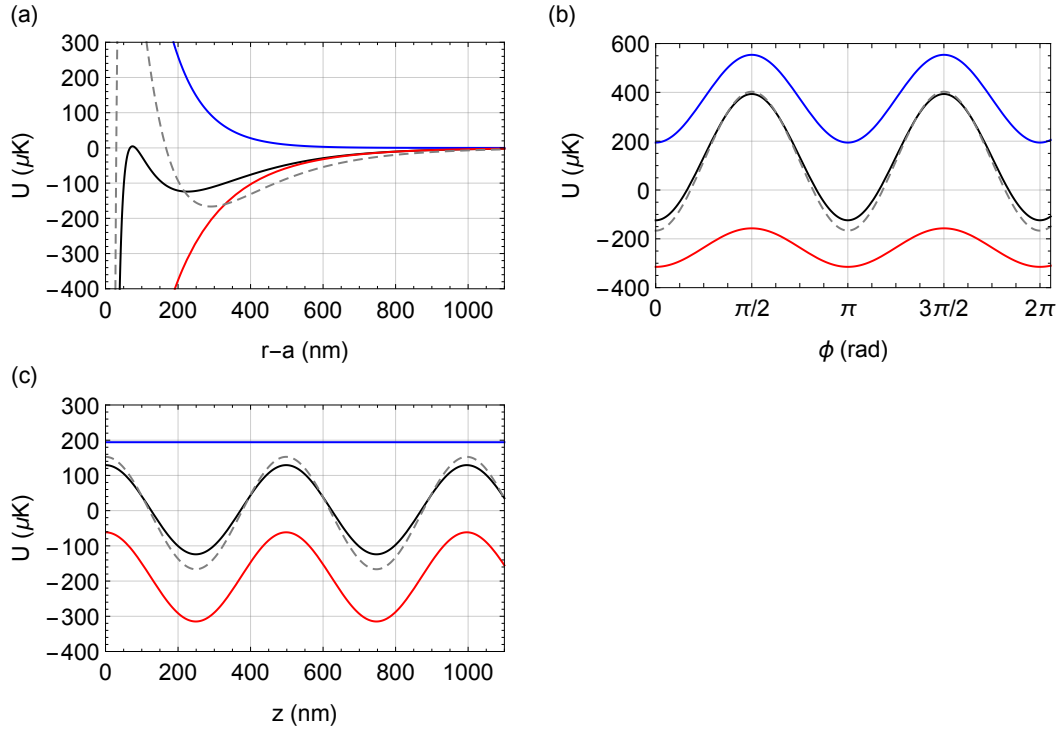

Figure 3.3: Potential U versus (a) radial distance r from the fiber surface at a, (b) azimuthal angle ϕ with respect to the x-axis and (c) axial position z along the nanofiber with arbitrary starting point for r and ϕ positions at the respective trap potential minimum. The solid lines in blue and red indicate the potential induced by the blue and red-detuned trapping light fields, respectively. The solid and dashed black lines indicate the total trapping potential, including van der Waals interaction, for two different sets of trapping laser powers. The main orientation of the quasi-linear polarization of the respective trapping light field is orthogonal to the other one. All parameters are indicated in the text and in Tab. 3.1.

on the light field intensity as well as the scalar part of the ground state polarizability. Since here the latter is positive for a wavelength larger than the wavelength at resonance, the atom will see a trapping potential for a spatially varying light field intensity. The repulsive potential is created by a blue-detuned light field sent through the fiber, with the scalar polarizability of the ground state being negative for this wavelength.

In Fig. 3.3(a) the radial dependence of the individual potentials induced by the blue-detuned (blue curve) and red-detuned (red curve) light fields are plotted for fixed azimuthal and axial positions. The total potential, which also takes the van der Waals potential into account, is depicted by the solid black curve. The parameters for the trapping lasers are given in Tab. 3.1. Since the radial extend of the evanescent field depends on the wavelength, the repulsive potential generated by the blue-detuned light approaches zero faster than the attractive potential stemming from the red-detuned light field. This results in a potential well with a depth of about $120\,\mu K$ and its minimum is located at about $220\,nm$ distance from the fiber surface. The dashed black line in Fig. 3.3(a) is the total potential calculated for higher powers of the trapping lasers, with parameters as given in Tab. 3.1. Here the trap is about $160\,\mu K$ deep with its minimum about $280\,nm$ away from the fiber surface.

The azimuthal confinement is realized by using quasi-linearly polarized trapping light fields that show an azimuthally asymmetric intensity distribution (see Fig. 2.3). With both trapping light fields being quasi-linearly polarized two potential wells will be formed on opposite sides of the fiber. To maximize the depth of the potential wells the trapping light field's main polarization axes are set to be orthogonal to each other. The red-detuned light field's polarization is aligned along the x-axis, therefore the atoms will be trapped along the x-axis at $y = 0$ as well. Figure 3.3(b) shows the azimuthal dependence of the potentials induced by red and blue-detuned lasers, in red and blue respectively, as well as the total potential in black. The parameters are the same as in Fig. 3.3(a), the radial position is at the minimum of the radial trap and the axial position is fixed. The azimuthal angle ϕ is given with respect to the x-axis. One can see that the atoms are trapped at $\phi = 0$ and $\phi = \pi$.

To achieve axial confinement two phase-stable red-detuned trap lasers are counter-propagating in the nanofiber, creating a standing wave. The atoms are now confined in the anti-nodes of the standing wave. This is illustrated in Fig. 3.3(c) where the individual potentials are shown in dependence of the axial position along the nanofiber. The radial and azimuthal position is at the respective trap minimum.

	Light field	Wavelength	Power	Quasi linear polarization
Config. 1	Red-detuned	$1064\,nm$	$2{\times}0.65\,mW$	along x-axis
solid line	Blue-detuned	$783\,nm$	$7\,mW$	along y-axis
Config. 2	Red-detuned	$1064\,nm$	$2{\times}1.25\,mW$	along x-axis
dashed line	Blue-detuned	$783\,nm$	$17.1\,mW$	along y-axis

Table 3.1: Parameters of trapping light fields used to calculate the curves in Fig. 3.3. These configurations are used in the experiments described in Ch. 5 and Ch. 6.

By combining all three techniques one achieves full 3D confinement of the Cesium atoms, which yields two 1D optical lattices on opposite sides of the nanofiber. At the precise minimum of the trapping potentials the atoms are only subject to the scalar part of the dynamical polarizability. The blue-detuned light field has its main polarization axis orthogonal to the plane in which the atoms are trapped, leading to a perfectly linear polarization at the position of the trap potential minimum, thus the vector part of the AC Stark shift vanishes. For the counterpropagating red-detuned light fields the longitudinal polarization components are anti-parallel and therefore compensate each other. Thus, the two red-detuned trapping light fields have no contribution to the vector light shift.

3.3 Fictitious magnetic fields

An important feature of the vector part of the AC Stark interaction operator in Eq. 3.21 is, that it can be treated as a fictitious magnetic field B_{fict}. The latter is interacting with the atoms as any conventional magnetic field would and can therefore be simply added to an external magnetic field [60]. The vector part of the interaction operator can now be rewritten to be of similar form as the Zeeman Hamiltonian in Eq. 3.5, giving ($\hbar = 1$)

$$
\begin{aligned}
V_{\text{EE,v}} &= i|\mathcal{E}|^2 \alpha^v_{nJF} \frac{(\mathbf{e}^* \times \mathbf{e}) \cdot \hat{\mathbf{F}}}{8F} \\
&= \mu_{\text{B}} g_{\text{F}} \hat{\mathbf{F}} \cdot \mathbf{B}_{\text{fict}},
\end{aligned} \tag{3.22}
$$

with

$$
\mathbf{B}_{\text{fict}} = \frac{\alpha^v_{nJF}}{8\mu_{\text{B}} g_{\text{F}} F} \left(\boldsymbol{\mathcal{E}}^* \times \boldsymbol{\mathcal{E}} \right). \tag{3.23}
$$

Here it is assumed that the effect of the fictitious magnetic field is small compared to the hyperfine splitting and, thus, F is a good quantum number. Given how the positive frequency envelope $\mathcal{E}$ enters Eq. 3.23, it becomes clear that the fictitious magnetic field is zero for purely linearly polarized light. Since the evanescent field of the fiber-guided fundamental mode can be elliptically polarized, as discussed in Ch. 2.2, the atoms can be subject to a fictitious magnetic field, depending on the position of the atom within the profile of the guided mode.

Figure 3.4 shows the magnitude and orientation of the fictitious magnetic field $\mathbf{B}_{\text{fict}}$ in the vicinity of the nanofiber. Here, the fictitious magnetic field is induced by the blue-detuned light field with its quasi linear polarization oriented along the y-axis. In Fig. 3.4(a) the x-component of $\mathbf{B}_{\text{fict}}$ is plotted as a contour plot in the x-y-plane. The color indicates the magnitude of $B_{\text{fict,x}}$ in Gauss. The positive sign of $B_{\text{fict,x}}$ means that the magnetic field vector points in positive x-direction and opposite for negative sign. For a light field with a wavelength of $783\,\text{nm}$ the magnetic field can reach values of up to $2.86\,\text{G/mW}$ at the surface of the nanofiber. Since the orientation of $\mathbf{B}_{\text{fict}}$ follows the ellipticity vector $\boldsymbol{\epsilon} = i(\boldsymbol{\mathcal{E}}^* \times \boldsymbol{\mathcal{E}})/|\boldsymbol{\mathcal{E}}|^2$, the fictitious magnetic field points in opposite directions on opposite sides of the nanofiber. In Fig. 3.4(b) the y-component of $\mathbf{B}_{\text{fict}}$ is shown for the same settings as in Fig. 3.4(a). Here the magnitude of $B_{\text{fict,y}}$ reaches up to $0.4\,\text{G/mW}$ at the surface of the nanofiber. These fictitious magnetic fields lead to a variety of effects (see e.g. [32, 46]). Two of those will be discussed in the following sections.
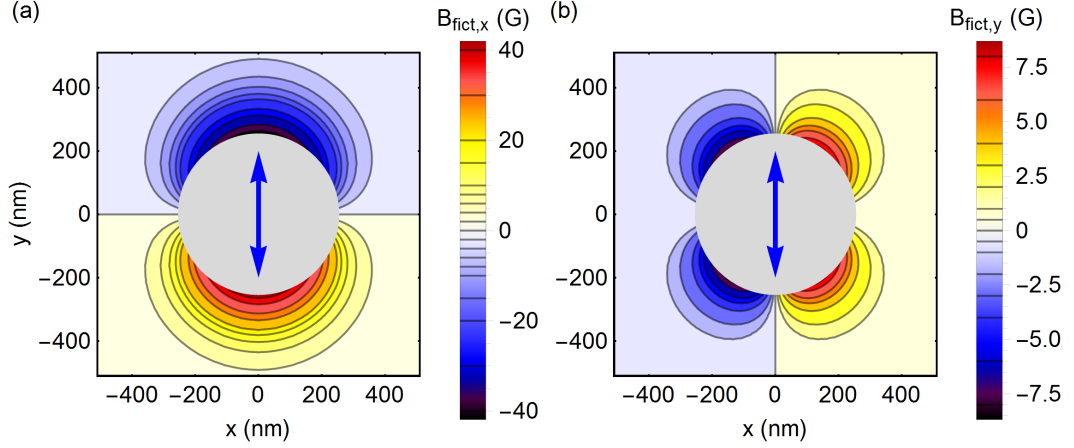
Figure 3.4: Contour plot showing (a) x-component and (b) y-component of the fictitious magnetic field $\mathbf{B}_{\text{fict}}$, generated by a fiber-guided quasi-linearly polarized light field with its main polarization as indicated by the blue double arrow in the center. The fictitious magnetic field is calculated for a light field with a wavelength of $783\,\text{nm}$ and a power of $17.1\,\text{mW}$. The colors indicate the magnitude of the fictitious magnetic field in Gauss. The positive (negative) sign of B_{fict} indicates that the field is parallel (anti-parallel) to the (a) x-axis or (b) y-axis. The gray disc in the center represents the nanofiber.

3.3.1 State-dependent potentials

As seen in Fig. 3.4 there is no fictitious magnetic field at the center of the trapping potential at $|x| \approx 540\,\text{nm}, y = 0\,\text{nm}$. However, there is a large gradient of $B_{\text{fict,x}}$ in azimuthal direction reaching more than $1000\,\text{G/mW/cm}$. Taking the direction of the local fictitious magnetic field $\mathbf{B}_{\text{fict}}$ as the quantization axis, the vector part of the AC Stark shift is diagonal in the m_F-basis ($\hat{F}_z\,|m_\text{F}\rangle = \hbar m_\text{F}\,|m_\text{F}\rangle$) and depends on the magnetic sublevels m_F of each hyperfine level F as [60]

$$V_{EE,v} = \mu_\text{B}\,g_\text{F}\,m_\text{F}\,B_{\text{fict}}. \tag{3.24}$$

In the vicinity of the potential minimum one can assume that the fictitious magnetic field is linear to the first order in azimuthal direction. Expanding the fictitious field in a Taylor series around $\phi = 0$ and only considering the linear term yields

$$V_{EE,v} = \mu_\text{B}\,g_\text{F}\,m_\text{F}\,\phi\,\frac{\partial B_{\text{fict}}}{\partial \phi}. \tag{3.25}$$

In Fig. 3.5 the azimuthal trapping potentials are plotted for different magnetic sublevels, indicated by different colors, in (a) for the $6S_{1/2}\ F = 3$ and in (b) for the $6S_{1/2}\ F = 4$ ground state. At the azimuthal position of the trapped atoms at $\phi = \{0, \pi\}$ there is no fictitious magnetic field, hence the magnetic sublevels are degenerate. This degeneracy is lifted for azimuthal positions of $\phi \neq \{0, \pm\pi\}$, where the atoms are subject to a non-zero fictitious magnetic field. The potential
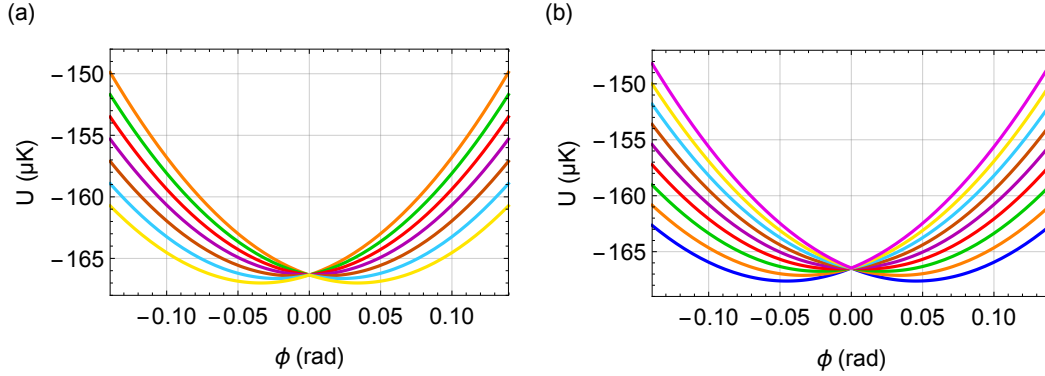
Figure 3.5: Azimuthal trapping potential U of the (a) $6S_{1/2}$ $F=3$ and (b) $6S_{1/2}$ $F=4$ ground state versus the azimuthal angle ϕ. The colors indicate the different m_F sublevels. The red-detuned and blue-detuned trap lasers have powers of $1.25\,\text{mW}$ and $17.1\,\text{mW}$ respectively. The trapping potential is calculated at a radial position of $540\,\text{nm}$ from the nanofiber axis.

wells for all sublevels except of $m_F=0$ are modified as the fictitious magnetic field leads to an increase or reduction of the energy of each sublevel according to the Landé g-factor.

Figure 3.6(a) shows the influence of an external magnetic field $B_{\text{ext},x} = 5\,\text{G}$ oriented along the x-axis on the azimuthal trapping potential of the $6S_{1/2}$ $F=4$ ground-state level. One can see, that the degeneracy of the ground-state sublevels is lifted. In addition the individual minima of the azimuthal trapping potentials are shifted along ϕ, where the magnitude of the shift depends on the considered m_F sublevel. This can be understood as the total magnetic field $B_x = B_{\text{ext},x} +$

Figure 3.6: (a) Azimuthal trapping potential U of the $6S_{1/2}$ $F=4$ ground-state versus the azimuthal angle ϕ for an external magnetic field $B_{\text{ext}} = 5\,\text{G}$ oriented along the x-axis. The dots mark the position of the potential minimum. (b) Azimuthal displacement of the trap potential minimum of each m_F sublevel shown in (a). All parameters as in Fig. 3.5. The colors indicate the different m_F sublevels.

$B_{\text{fict},x}$ decreases along positive ϕ and increases along negative ϕ. The azimuthal displacement of the trap minimum in dependence of the m_F sublevel is illustrated in Fig. 3.6(b).

3.3.2 Spin-motion coupling

In the previous section of this chapter we investigated the influence of the fictitious magnetic field on the trapping potential in the presence of an external magnetic field oriented parallel to the fictitious field. As seen in Fig. 3.6 this leads to a displacement of the trap potential minimum of each m_F sublevel. In this section we will investigate the case where the external magnetic field is oriented orthogonal to the fictitious field.

In this case the magnitude and orientation of the total magnetic field

$$\mathbf{B} = (B_{\text{fict}}, B_{\text{ext}}, 0)$$

vary spatially in the vicinity of the trapped atoms. The y component of the fictitious field is neglected in the following considerations. This variation of $\mathbf{B}$ can cause spin-flips for small external magnetic fields [60]. For large enough magnetic fields the spin-flip rate decreases with an increasing external magnetic field. If the latter is large compared to the fictitious magnetic field, the contribution of the fictitious field is negligible. As the atoms experience the same magnitude and orientation of magnetic field everywhere the atoms undergo no spin-flips any longer. The trapping potential experienced by atoms in the respective m_F sublevels is shown in Fig. 3.7. Using the same parameters as in Fig. 3.6, but with $B_{\text{ext},y} = 5\,\text{G}$ oriented along the y-axis, the azimuthal trapping potential of the $6S_{1/2}$ $F\!=\!4$ ground-state level shows practically no displacement any more [60]. The external magnetic field just lifts the degeneracy of the magnetic sublevels, but the trap minima are all very close to $\phi\!=\!\{0, \pm\pi\}$.

To give a quantitative description of the system one has to derive the Hamiltonian. Since the scalar part of the potential is not affected by magnetic fields it is sufficient to write down the
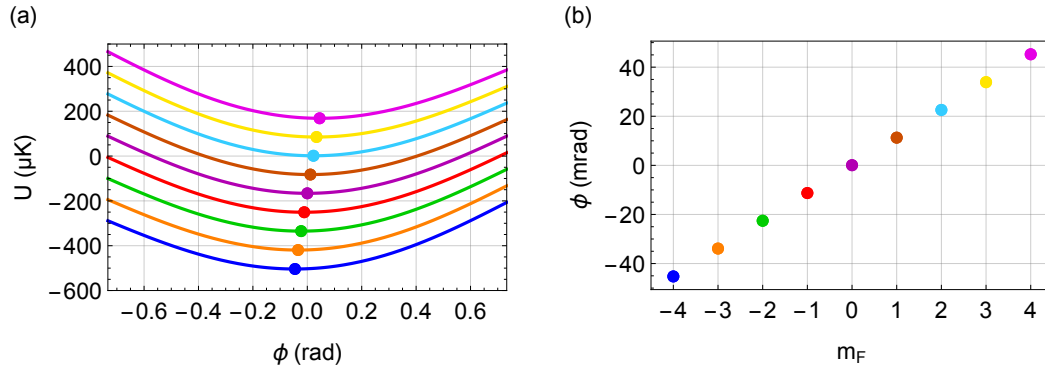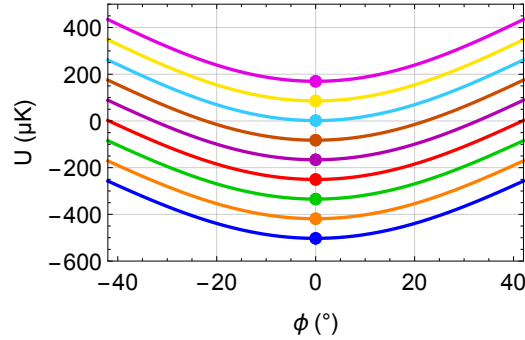

Figure 3.7: Azimuthal trapping potential U of the $6S_{1/2}$ $F\!=\!4$ ground-state versus the azimuthal angle ϕ for an external magnetic field $B_{\text{ext},y} = 5\,\text{G}$ oriented along the y-axis. The dots mark the position of the potential minimum. The colors indicate the different m_F sublevels. All parameters as in Fig. 3.6.

vector part which reads

$$
\begin{aligned}
V_{EE,v} &= \mu_B \, g_F \, \hat{\mathbf{F}} \cdot \mathbf{B} \\
&= \mu_B \, g_F \left(B_{\text{ext}} \hat{F}_y + \phi \frac{\partial B_{\text{fict}}}{\partial \phi} \hat{F}_x \right).
\end{aligned}
\tag{3.26}
$$

Here a linear expansion for the x-component of the fictitious magnetic field in azimuthal direction ϕ in the vicinity of the scalar potential minimum is used. For a quantization axis along the external magnetic field, i.e., along the y-axis, the left-hand term in Eq. 3.26 is diagonal in the $|m_F\rangle$-basis, defined such that

$$
\hat{F}_y \, |m_F\rangle = \hbar m_F \, |m_F\rangle .
$$

However, the right-hand term is not diagonal and m_F is not a good quantum number. The operator $\hat{F}_x$ can be rewritten using the ladder operators $\hat{F}_\pm$

$$
\hat{F}_x = \frac{1}{2} \left(\hat{F}_+ + \hat{F}_- \right),
\tag{3.27}
$$

with

$$
\hat{F}_\pm \, |m_F\rangle \propto |m_F \pm 1\rangle .
\tag{3.28}
$$

In the vicinity of the center of the azimuthal trapping potential we can neglect the curvature of the trap along ϕ, assume a harmonic potential solely along y and use

$$
B_{\text{fict}} \approx y \frac{\partial B_{\text{fict}}}{\partial y}.
\tag{3.29}
$$

The motion of the atom in the trap can be quantized as

$$
\hat{y} = \frac{y_0}{\sqrt{2}} \left(\hat{a} + \hat{a}^\dagger \right); \quad y_0 = \sqrt{\frac{\hbar}{m\omega_y}},
\tag{3.30}
$$

with the annihilation and creation operators a and $a^\dagger$, respectively, as well as the mass m and the trap frequency ω_y. Inserting Eq. 3.27, Eq. 3.29 and Eq. 3.30 into Eq. 3.26 the vector part of the potential reads

$$
V_{EE,v} = \mu_B \, g_F \left(B_{\text{ext}} \hat{F}_y + \frac{\partial B_{\text{fict}}}{\partial y} \frac{y_0}{\sqrt{8}} \left(\hat{a} + \hat{a}^\dagger \right) \left(\hat{F}_+ + \hat{F}_- \right) \right).
\tag{3.31}
$$

From Eq. 3.31 it becomes clear, that the second term causes spin-flips at the expense of adding or removing motional excitations in the azimuthal trapping potential. These spin-flips are enhanced at resonance, when the magnitude of the external magnetic field is such, that the energy splitting $\Delta = \mu_B \, g_F B_{\text{ext}}$ between adjacent m_F sublevels is equal to the trap frequency ω_y. Then, for the $6S_{1/2} \, F = 3$ ground state $\hat{a}\hat{F}_-$ lowers the motional state while removing a spin excitation, effectively moving the atom to a higher energy m_F level as $g_{F=3} < 0$. The term $\hat{a}^\dagger \hat{F}_+$ increases the motional state while adding a spin excitation resulting in the occupation of a lower energy m_F level. For the $6S_{1/2} \, F = 4$ ground state the effects of $\hat{F}_+$ and $\hat{F}_-$ on the eigenenergy are inverted compared to the case of $F = 3$, as $g_{F=4} > 0$.
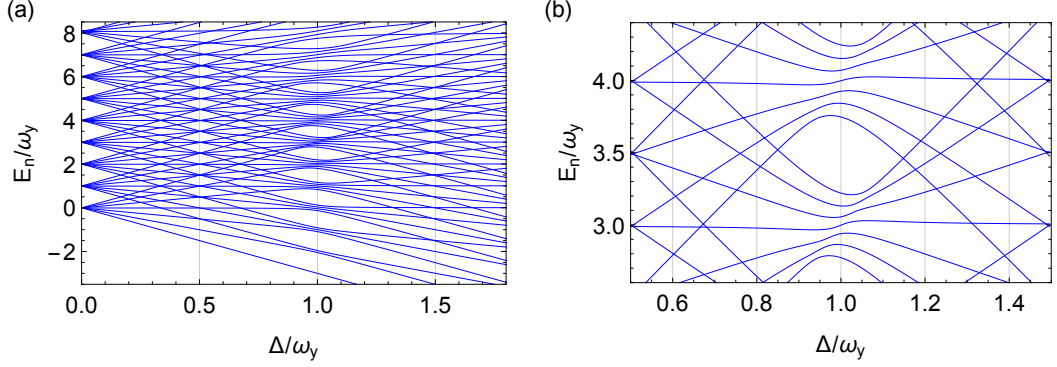
Figure 3.8: (a) Numerically computed eigenenergies E_n of the $6S_{1/2}$ $F=3$ ground-state versus the energy shift $\Delta = \mu_B \, g_F B_{\text{ext}}$ of the Zeeman levels which is proportional to the external magnetic field B_{ext}. The eigenenergies as well as the external magnetic field are normalized to the azimuthal trap frequency ω_y. (b) Zoom of the avoided crossings at $\Delta/\omega_y = 1$. For improved clarity the fictitious magnetic field gradient was reduced to $0.4\,\text{G}/\mu\text{m}$ for this plot instead of the calculated value of $1.4\,\text{G}/\mu\text{m}$.

In Fig. 3.8 the calculated eigenenergies of the system are plotted versus the magnitude of the external magnetic field. For this calculation the Hamiltonian

$$\hat{H} = \omega_y \hat{a}^\dagger \hat{a} + \mu_B \, g_F \left(B_{\text{ext}} \hat{F}_y + \frac{y_0}{\sqrt{2}} \left(\hat{a} + \hat{a}^\dagger \right) \frac{\partial B_{\text{fict}}}{\partial y} \hat{F}_x \right)$$

has been diagonalized numerically for different values of B_{ext}. The Zeeman effect causes an initial linear increase of the eigenenergies where the slope depends on the considered m_F level. For $\Delta \gg \omega_y$ the unperturbed states of the Hamiltonian can be identified as the individual m_F-states for each vibrational level. The perturbation by the F_x term in Eq. 3.31 causes a set of avoided crossings around resonance ($\Delta = \omega_y$) where the eigenenergies would be degenerate without the F_x coupling. The extent of the resonance depends on the strength of the F_x-coupling and, e.g., the fictitious field gradient. If $B_{\text{ext},y}$ is ramped adiabatically across the resonance, the atom will follow one energy branch, and both its spin and vibrational level will be altered.

Taking a closer look at the involved degenerate states $|n, m_F\rangle$ coupling at resonance one finds, that at an eigenenergy $E_q = (q - F)\omega_y$, with $q \geq 1$, they fulfill the condition

$$|n = q - i, m_F = F - i\rangle \quad \text{for} \quad 0 \leq i \leq \min(q, 2F). \tag{3.32}$$

This is also apparent in Fig. 3.8(a). At resonance only the state $|0, 3\rangle$ has an eigenenergy of $E_q = -3\omega_y$. For $E_q = -2\omega_y$ one finds $|0, 2\rangle$ as well as $|1, 3\rangle$, for $E_q = -\omega_y$ there are $|0, 1\rangle$, $|1, 2\rangle$ as well as $|2, 3\rangle$ and so on. The layout of the avoided crossings is such, that the energy order of the eigenstates is preserved. This means that, e.g., the eigenstate with the lowest energy before the resonance will be mapped to the eigenstate with the lowest energy after the resonance. Assuming, e.g., that the atoms are all in the motional ground state $n = 0$ initially and evenly

distributed across all m_F-states one can determine, for this special case, how the spin and phonon distributions will evolve, given that the magnetic field is increased adiabatically:

$$
\begin{aligned}
|n = 0, m_\mathrm{F} = 3\rangle &\rightarrow & |0, 3\rangle \\
|0, 2\rangle &\rightarrow & |1, 3\rangle \\
|0, 1\rangle &\rightarrow & |2, 3\rangle \\
|0, 0\rangle &\rightarrow & |3, 3\rangle \\
|0, -1\rangle &\rightarrow & |4, 3\rangle \\
|0, -2\rangle &\rightarrow & |5, 3\rangle \\
|0, -3\rangle &\rightarrow & |6, 3\rangle \,.
\end{aligned}
\tag{3.33}
$$

This simple model indicates, that the phonon distribution is mapped onto the spin distribution and vice versa. The atoms that were initially in the lowest energy motional state are in the lowest energy spin state after adiabatically crossing the resonance. Atoms in $F = 4$ ($F = 3$) that are in the motional ground state initially would be prepared in $m_\mathrm{F} = -4$ ($m_\mathrm{F} = 3$) after the resonance. During this mapping they are effectively heated up as higher motional states are now populated.

While this example explains the experimental findings reasonably well it is based on a very simplified model. It completely neglects higher order terms of the fictitious magnetic field. In addition it also does not consider the anharmonicity of the azimuthal trapping potential as well as the radial potential in general. Going into detail is beyond the scope of this thesis as the dynamics of the spin-motion coupling is still under investigation.

Experimental setup

The experimental setup was developed by multiple PhD students over the course of several years. A more detailed description of the whole setup can be found in the corresponding PhD theses [45, 61–63]. In the first section of this chapter a general overview regarding initial steps towards trapping of laser-cooled Cesium atoms in optical nanofiber based dipole traps will be given. This will be followed by a section with details about the optical setup and finally a section describing the probing of the atoms and the data acquisition.

4.1   Overview

Our experiment utilizes the nanofiber-mediated interaction between an optical field and neutral Cesium atoms. The nanofiber is produced in a heat and pull process out of a standard optical fiber[1] as described in Ch. 2. After the pulling process it is glued onto an aluminum mount, which is designed to enable good optical access to the nanofiber. The mount is placed in the center of a stainless steel vacuum chamber (see Fig. 4.1), which is required to minimize interactions between Cesium atoms and ambient air molecules. Furthermore, it reduces pollution of the nanofiber by dust particles. Both ends of the fiber exit the chamber via a Teflon feed-through. The vertical position of the nanofiber mount can be adjusted by an externally accessible micro-positioning screw. The Cesium atoms are supplied by dispensers, where they are stored in form of a stable solid body. By applying a current of between $4\,\mathrm{A}$ and $7\,\mathrm{A}$, the dispenser is heated up and the Cesium atoms are released. The higher the applied current the more Cesium atoms are released. To avoid coating the nanofiber with Cesium atoms, the dispensers are not in direct line of sight to the nanofiber.

The vacuum inside the chamber is maintained using an ion getter pump[2]. A pressure of $2.6 \times 10^{-9}\,\mathrm{mbar}$ is reached, measured using the current of the ion getter pump. The vacuum chamber features a total of eight viewports for optical access.

---

[1]Liekki Passive 6/125
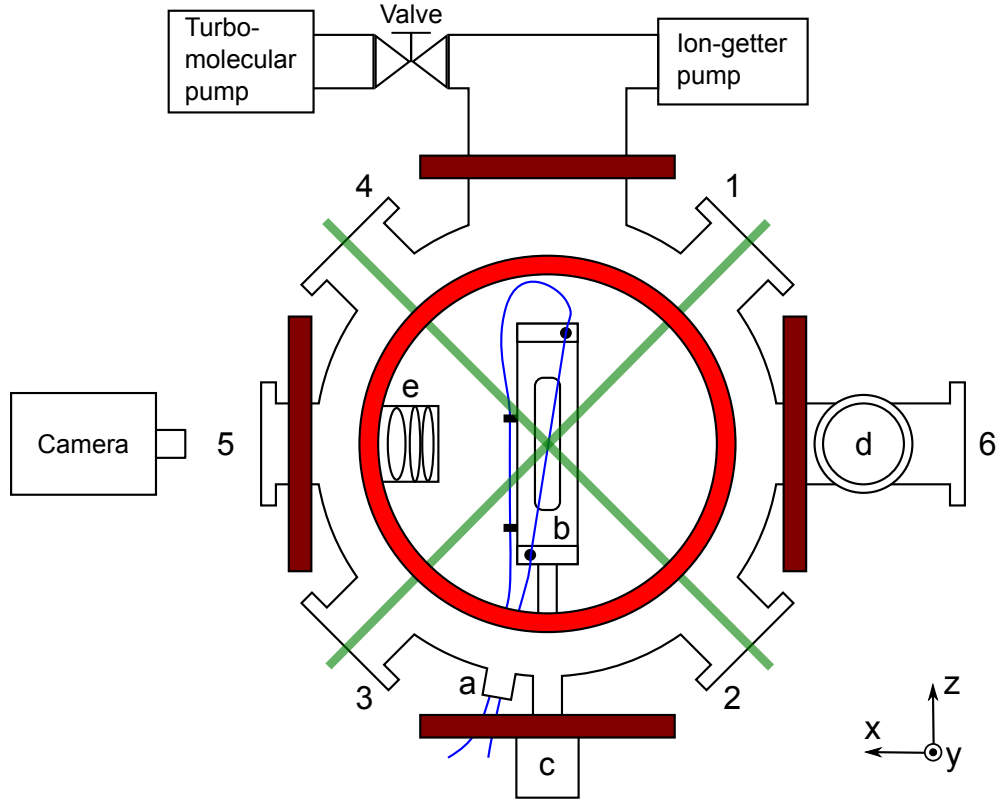[2]Varian Starcell 150 Dual

Figure 4.1: Sketch of the vacuum chamber and surroundings (top view). The unprocessed ends of the optical nanofiber (blue) enter the vacuum chamber through a Teflon feed-through a and is glued onto an aluminum mount b with the tapered section in the center of the mount. The latter can be positioned vertically along the y-axis using a micro-positioning screw c. The Cesium dispensers are placed inside a vertically extending tube d. The viewports are numbered 1 to 6, with two additional viewports, one at the top (7) and one at the bottom (8) of the chamber. The laser beams required to create the MOT enter the chamber through viewports 1 to 4 (green lines) as well as 7 and 8 (not shown). A camera can be used to observe the atoms and the fiber waist through viewport 5 using a microscope objective e for magnification. Viewport 6 can be used to add external light fields illuminating the fiber-coupled atoms. The red ring represents the external pair of copper coils above and below the aluminum mount used to create the magnetic field gradient required to create the MOT. The brown rectangles are coils used to apply homogeneous magnetic fields along x and z mainly to compensate stray magnetic fields.

In order to transfer the atoms into the fiber-based two-color dipole trap they are confined and cooled by a magneto optical trap (MOT) [18] first. The MOT is required as the temperature of the Cesium atoms after being emitted from the dispenser is too high to directly trap them in the optical dipole trap. To create a MOT a pair of parallel coils in anti-Helmholtz configuration provide the required quadrupole magnetic field. The necessary three orthogonal pairs of near-

resonant counter-propagating light fields enter the chamber through the viewports (numbered in Fig. 4.1).

The atoms are further cooled and eventually loaded into the nanofiber-based dipole trap via an optical molasses stage. Here the magnetic field is ramped down to zero and switched electronically to Helmholtz configuration. Additionally the detuning of the laser beams is increased while simultaneously reducing the power. This magnetic field, in addition to the field generated by two orthogonally oriented pairs of coils, is used to be able to compensate all external magnetic fields or apply a homogeneous magnetic field.

A typical nanofiber trap loading sequence consists of $1\,\mathrm{s}$ of loading the MOT, with the light fields at a total power of about $100\,\mathrm{mW}$ and red-detuned from resonance by about $10\,\mathrm{MHz}$. This is followed by about $200\,\mathrm{ms}$ of optical molasses stage. Here the detuning of the light fields is increased to about $60\,\mathrm{MHz}$ and the power reduced to about $20\,\mathrm{mW}$ in total.

After the atoms are loaded into the nanofiber trap, they are available for further manipulations. The typical lifetime of the atoms inside the trap is between $50\,\mathrm{ms}$ and $100\,\mathrm{ms}$.

4.2 Optical setup

In the experiments described in this thesis a multitude of lasers are required, which will be described in this section. For optical frequency and power modulation as well as switching the lasers on and off, acousto-optic modulators (AOM) are used.

For the initial MOT-phase of each experimental run a cooling laser (CO) red-detuned from the D2 line of Cesium at $852\,\mathrm{nm}$ wavelength is required, as described in chapter 4.1. The laser source is a commercial diode laser[3] in combination with a tapered amplifier[4] providing about $500\,\mathrm{mW}$ optical power. It is frequency locked via a Doppler-free Cesium saturation spectroscopy [64] to the $F = 4$ to $F' = 5$ transition of the D2-line and red-detuned from resonance by about $10\,\mathrm{MHz}$. Via a fiber port cluster[5], which is a device that combines several fiber couplers, wave plates and polarizing beam splitters, the CO is split into six beams. Using optical fiber patch cables, the CO beams are guided to special out-couplers[6] that set the polarization to circular and increase the beam $1/e^2$-diameter to about $1.5\,\mathrm{cm}$. The individual light fields are directed into the vacuum chamber through the viewports.

Due to off-resonant excitations the atoms can be transferred to the $F' = 4$ level instead of $F' = 5$ by CO, with a high probability to then decay to $F = 3$. Therefore a light field (RP) that optically repumps the atoms back to $F = 4$ is required. The laser is provided by a commercial laser diode[7] and frequency locked, using a polarization spectroscopy [64], to the $F = 3$ to $F' = 4$ transition of the D2-line. It is coupled into one port of the fiber port cluster such that it is out-coupled into two paths alongside the CO.

In order to trap the Cesium atoms in the vicinity of the nanofiber a two color dipole trap is used. It is realized by using a far red-detuned and a far blue-detuned fiber-coupled light field,

---

[3]Sacher Lasertechnik TEC500/P-850-0707-0627
[4]Sacher Lasertechnik TEC400/S852-0707-0178
[5]Schäfter & Kirchhoff fiber port cluster 1 to 6 for $852\,\mathrm{nm}$
[6]Schäfter & Kirchhoff fiber collimator 60FC-Q852-4-M75
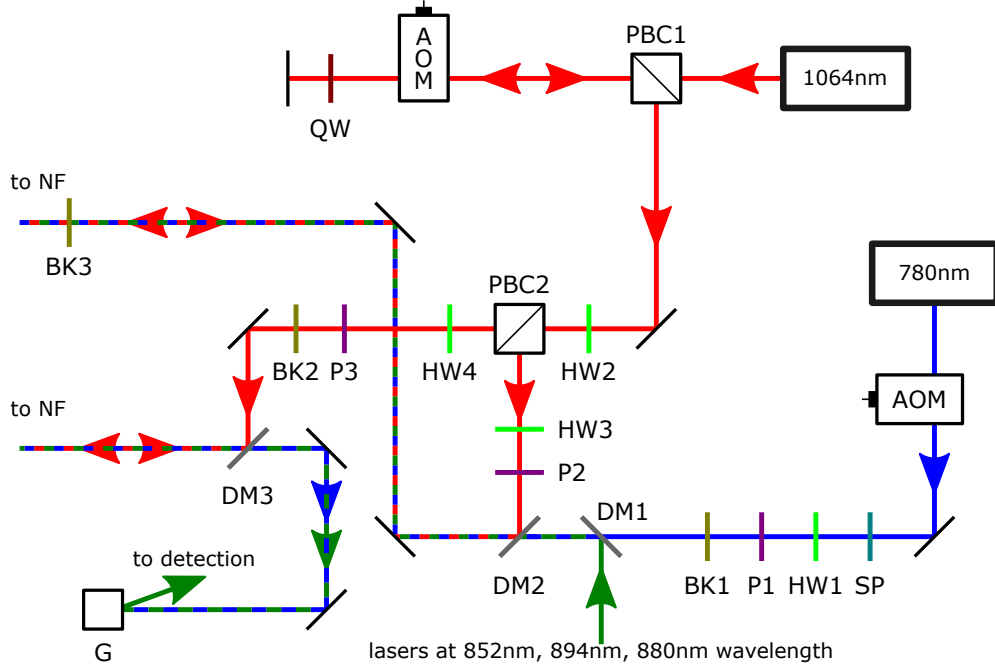[7]Sacher Lasertechnik Lynx TEC100/L-850-0707-0625

Figure 4.2: Sketch of the trap laser beam paths from their respective source to the optical nanofiber (NF) incoupling. In addition, the following optical components are shown: Berek compensator (BK), dichroic mirror (DM), volume bragg grating (G), half-wave plate (HW), polarizer (P), polarizing beam splitter cube (PBC), short pass filter (SP), quarter-wave plate (QW).

see chapter 3.2. Figure 4.2 shows a sketch of the trap laser setup. The blue-detuned light field is generated by a diode laser[8] at $783\,\text{nm}$ wavelength with about $150\,\text{mW}$ output power. To block any resonant amplified spontaneous emission background around the Cesium resonance, the light is filtered using a short pass filter (SP)[9]. For setting the polarization of the laser a half-wave plate (HW1) and a polarizer (P1) are used. To compensate any birefringence introduced by optical elements in the beam path as well as by the optical fiber a thin birefringent plate, here referred to as Berek compensator (BK1), is used.

The red-detuned light field is provided by a neodymium-doped yttrium aluminum garnet (Nd:YAG) crystal laser[10] at $1064\,\text{nm}$ wavelength with about $600\,\text{mW}$ maximum output power. In order to use the red-detuned light field in a standing wave configuration, it has to be split into two beams that are counter-propagating through the nanofiber. This is achieved by using a polarizing beam splitter cube (PBC2), where the power ratio can be adjusted by a half-wave plate (HW2). Both beam paths use a combination of polarizer (P2 and P3) and half-wave plate (HW3 and HW4) to adjust the polarization. Furthermore Berek compensators (BK2 and BK3)

---

[8]Toptica DL100/02479
[9]Asahi XIS 0810
[10]Spectra Excelsior 1064-650/650000

are deployed to compensate birefringence. Note that BK3 also affects the other lasers coupled into the nanofiber.

To probe the atoms trapped around the nanofiber, a light field resonant with the D2 line of Cesium at $852\,\mathrm{nm}$ wavelength, provided by a diode laser[11] mounted in Littrow configuration, is used. The polarization control is done similarly as for the trapping lasers and not shown in Fig. 4.2. To minimize heating and other perturbations during the probing of the atoms, the power of the light field is set to a few pW. Due to the strong confinement of the nanofiber guided light field the evanescent field offers a very high intensity already at low powers. This high intensities combined with the good coupling between the evanescent field and the atoms lead to low saturation powers of only a few hundred pW. Therefore such low powers in the pW range are sufficient for our experiments.

In the experiments presented in the following chapters, three additional light fields are used. The respective light sources operate at a wavelength of $894\,\mathrm{nm}$[12], $852\,\mathrm{nm}$[13] and $880\,\mathrm{nm}$[14]. All three are provided by laser diodes mounted in Littrow configuration and use the same method to control the polarization as was described for the other lasers above.

All light fields are coupled into the nanofiber via two fiber couplers. Therefore, the light fields need to be overlapped, which is done using dichroic mirrors DM1 and DM2. These mirrors are specifically designed to reflect a specific wavelength range while transmitting another. Here DM1 reflects (transmits) light with a wavelength above (below) $800\,\mathrm{nm}$ and DM2, as well as DM3, reflects (transmits) light with a wavelength above (below) $900\,\mathrm{nm}$. After passing the nanofiber the red-detuned light field is separated from the probing light field by DM2. The blue-detuned trapping laser generates photons in a wide wavelength range due to Raman scattering in the optical fiber. Most crucial in this context is the wavelength range around $852\,\mathrm{nm}$. Previous measurements indicate that one gets $0.04\,\mathrm{pW}$ per meter length and nanometer wavelength interval of Raman light at $852\,\mathrm{nm}$ wavelength for $1\,\mathrm{mW}$ of fiber-guided light at $783\,\mathrm{nm}$. By adding a volume-Bragg-grating[15] the background introduced by this effect is reduced. It has a full width half maximum spectral selectivity of $0.12\,\mathrm{nm}$ and is put right before coupling into the detection system. With this, it is ensured that only resonant light around $852\,\mathrm{nm}$ is directed towards the detector.

4.2.1 Fabry-Pérot bandpass filter

While using a volume-Bragg-grating as a narrow bandpass filter is sufficient for most experiments conducted with our setup, measurements on the order of single photons require an even better suppression of background or off-resonant light fields. A Fabry-Pérot cavity is a useful tool to improve the spectral selectivity, enabling narrow transmission windows with a full width at half maximum (FWHM) linewidth in the tens of MHz regime. In this experiment the Fabry-Pérot cavity is added in between the volume-Bragg-grating and the detector. The cavity itself

---

[11]Sacher Lasertechnik LION TEC500/P-850-0707-0626
[12]Thorlabs L904P010
[13]Spectra Diode Labs SDL-5401
[14]Eagleyard EYP-RWE-0860
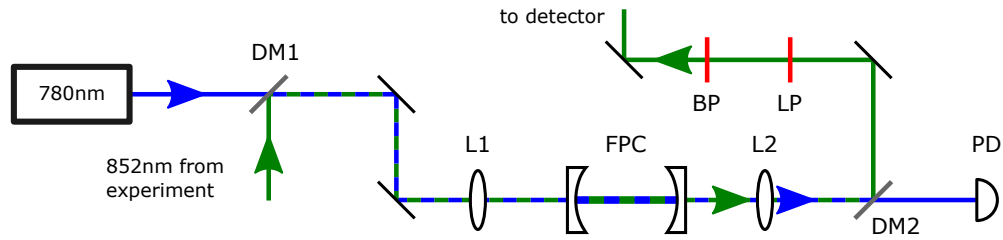[15]Optigrate RBG-582-94

Figure 4.3: Sketch of the Fabry-Pérot bandpass filter setup. The probing light field and the reference laser at 780 nm wavelength are overlapped at a dichroic mirror (DM1). Both light fields are coupled into the Fabry-Pérot cavity (FPC) via a lens L1. A second lens (L2) is used to collimate the light fields after leaving the cavity. At a second dichroic mirror (DM2) both light fields are separated again. While the reference laser is detected via a photodiode (PD), the probing light field is transmitted through a longpass (LP) and a bandpass filter (BP) and guided towards the detector.

consists of two parallel plano-concave mirrors[16], with a reflectivity of about 98.5 % each. For a precise alignment of the distance between the mirrors, one of them is mounted on a translation stage[17]. An additional piezo crystal enables one to stabilize the cavity for a constant performance of the system. The cavity is actively stabilized to a reference laser with a free space wavelength of 780 nm, that is coupled into the cavity alongside the probing light field. To this end, the cavity is locked to the transmission of the reference laser by adjusting the position of the second mirror. Since the probing light field and the reference laser do not have the same frequency, the reference laser is coupled into the cavity such, that a multitude of different modes can be excited. Now, one has to lock to a transmission peak of the reference laser that overlaps with the transmission peak of the probe light field in the fundamental mode.

A sketch of the bandpass filter setup is shown in Fig. 4.3. The reference light field at 780 nm wavelength is provided by a diode laser[18] that is locked on a Rubidium spectrum. The probing laser at 852 nm wavelength is guided from the experimental setup to the filter cavity setup via a standard optical fiber. Not shown in Fig. 4.3 is an optical isolator right after the fiber coupler used to minimize back-reflections towards the experimental setup. Both light fields are overlapped using a dichroic mirror[19] (DM1) and coupled into the cavity (FPC) via a coupling lens (L1)[20]. After passing the cavity, the light fields are are collimated by L2 and then separated by another dichroic mirror (DM2). The reference laser is detected by a photodiode (PD) that produces the error signal for stabilizing the cavity. The probing light field passes a longpass[21] (LP) and a bandpass[22] (BP) filter to remove any remaining reference laser light, that is reflected off the second dichroic mirror. After this purification steps the probing laser is forwarded to the detector.

---

[16]Lens-Optics PR780–1064nm/0°, Bk7, Radius -50 mm
[17]Thorlabs NF15AP25/M
[18]Thorlabs L785P090
[19]Thorlabs DMSP805
[20]Thorlabs LA1229-B, $f = 175$ mm
[21]Asahi XIL0840
[22]Semrock LL01-582-12.5

In its current configuration, the Fabry-Pérot filter cavity offers a full spectral range (FSR) of $16.4\,\mathrm{GHz}$, a linewidth of $(73.50 \pm 0.27)\,\mathrm{MHz}$ and a finesse of 233 ± 1. With this, the suppression of off-resonant frequencies is about $-43\,\mathrm{dB}$ and the overall background is reduced by a factor of 70. These values are achieved at an on-resonance transmission through the cavity of $(76.6 \pm 0.7)\,\%$.

4.2.2 Precision analysis and tuning of polarizations on the nanofiber waist

The nanofiber is produced out of a standard optical fiber which offers no inbuilt means to maintain a given polarization. By carefully mounting the fiber and stabilizing the temperature, changes of the fiber's birefringence can be reduced to a minimum. To compensate the unavoidable remaining birefringence a Berek compensator is used. Since the nanofiber is birefringent as well, the polarization can only be precisely adjusted for a small part of the taper region. A natural choice would be the region where the atoms are trapped.

For alignment of the light field's polarization at the taper region, the Rayleigh scattering of a fiber-guided light field, caused by, e.g., inhomogeneities in the silica fiber, is detected via a CCD camera [62]. The scatterers are assumed to be point like dipole emitters, meaning that the local polarization is conserved. The scattered light is collected via a system of lenses inside the vacuum chamber. On the outside of the chamber, a polarizing beam splitter cube ensures that only the transverse polarization component will be transmitted towards the CCD camera. Rotating a linear transverse polarization on the fiber waist then results in a sinusoidal variation of the detected intensity. By maximizing the visibility of the signal, the degree of linear polarization can be maximized as well. For an initial coarse alignment, it is sufficient to take the scattered light from the whole taper section into account.

For a more precise polarization adjustment, knowledge of the position of the trapped atoms along the taper section is necessary. This can be measured by sending a weak resonant light field through the fiber while the atoms are trapped. The resonant photons that are absorbed and re-emitted into free space are then detected using a sensitive CCD camera[23].

The result is shown in a two-dimensional color plot in Fig. 4.4. In the central plot, the number of detected photons per pixel is indicated by the color, ranging from blue (small number of photons) to red (large number of photons). The histograms on the left and bottom show the total counts for each line of pixels along the horizontal axis and vertical axis, respectively. The color plot shows the position of the trapped atoms in green and yellow. The red line represents the position of the MOT cloud and the nanofiber. From this, one can see that the atoms are trapped near the position where the MOT is formed in the vicinity of the nanofiber. By changing the settings of the magnetic compensation fields during the early molasses stage, the position as well as the spread of the trapped atomic ensemble can be influenced. This stems from the shift of the atomic cloud during the transition from the MOT stage to the molasses stage.

The magnetic compensation fields were adjusted such, that the extent of the atomic ensemble along the nanofiber is minimized while maintaining a reasonable number of trapped atoms. For these settings, the Rayleigh scattering measurements were repeated. To this end the polarization was rotated by a fixed angle and a two-dimensional image was taken with the CCD camera.
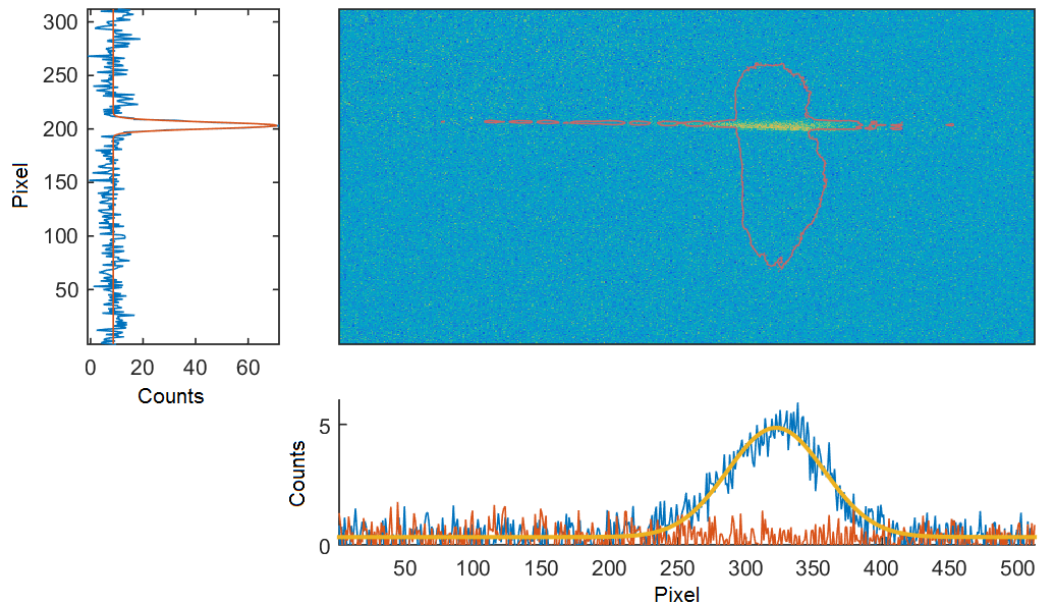
---

[23]Andor iXION Ultra

Figure 4.4: Flourescence image of the position of the nanofiber-trapped atoms in the vicinity of the nanofiber waist (center), and counts per pixel added horizontally (left) as well as vertically (bottom). The red contour indicates the position of the MOT and the outline of nanofiber, measured separately. The solid lines in the diagrams are Gaussian fits to the data.
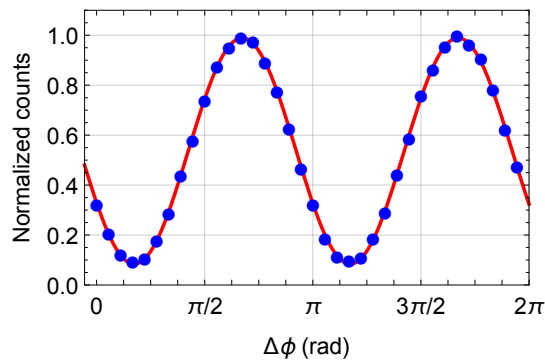

Figure 4.5: Photon counts detected by the camera at the position of the nanofiber-trapped atoms for a rotated linear polarization of a nanofiber-guided light field. Each data point in blue is the number of counts, normalized to the maximum number of photons, that are scattered from the nanofiber. Only the region where the atoms are trapped is taken into account. The number of counts is plotted over the angle of the main axis of the light field's linear polarization. The angle is given with respect to an arbitrary initial orientation. The solid line is a sinusoidal fit to the data points.

The photon counts were analyzed for the corresponding section of the taper region where the atoms are trapped. By repeating this procedure for several angles of the main axis of the light field's linear polarization in the transverse plane, the visibility can be determined. An example of the outcome of such a measurement is shown in Fig. 4.5. Here, the counts, normalized to the maximum number of counts, are plotted versus the angle of the principal axis of the linear polarization of the examined light field relative to an arbitrary initial orientation. Each data point is the number of detected photons that are emitted from the nanofiber normalized to the maximum number of photons observed. As mentioned above, only the region of the nanofiber where the atoms are trapped is taken into account. With an estimated visibility

$$\frac{\text{max counts} - \text{min counts}}{\text{max counts} + \text{min counts}}$$

of about $80\,\%$ and a sinusoidal distribution of the normalized counts, as indicated by the fit (solid line), the quality of the polarization adjustment is very good. The main limitation is probably a residual uncompensated birefringence stemming from the movement of the nanofiber and the solid angle of the camera.

4.2.3 Optical phase locked loop

Phase-coherent lasers are important tools for coherent quantum optic experiments. One of these experiments, that relies on electromagnetically induced transparency, will be presented in Ch. 5. In this experiment, the coherence time between the two optical fields that are required for EIT is a crucial parameter. To be able to maintain a fixed phase relation during the experiments, an optical phase locked loop is used. Ideally, it highly suppresses the phase noise and is able to handle large frequency fluctuations as well as compensating drifts, ensuring long-term stability. As the typical bandwidth of free running laser diodes is several MHz, a fast feedback loop with a bandwidth in the MHz range is necessary. To enable such fast control, the phase detector has to provide a fast response to fluctuations and a steep slope of the error signal. In addition, an equally fast actuator is required.

Both light fields used here are resonant with the D2 line of Cesium and operate in a master-slave configuration. The optical setup is sketched in Fig. 4.6. The master laser (Spectra) is locked to a Cesium polarization spectroscopy (PS). The polarization spectroscopy of the slave laser (Sacher Lion) is not used while the phase locked loop is in operation. Via the half-wave plate (HW3) in front of the polarization beam splitter cube (PBC3) the power of the light field forwarded into the spectroscopy branch can be set. The AOM in double-pass configuration changes the frequency of the light field before it enters the spectroscopy. This allows more flexibility when it comes to choosing the optimal locking point. The main part of the master laser power passes another AOM and is coupled into a commercial optical fiber (both not shown in Fig. 4.6) that is connected to the main part of the experimental setup. The second AOM provides the possibility to scan the master laser frequency. The AOM in the slave laser beam path allows scanning of the slave laser frequency. To keep a stable phase relation between both lasers even after passing their respective AOM, the latter get their driving radio frequency field from two
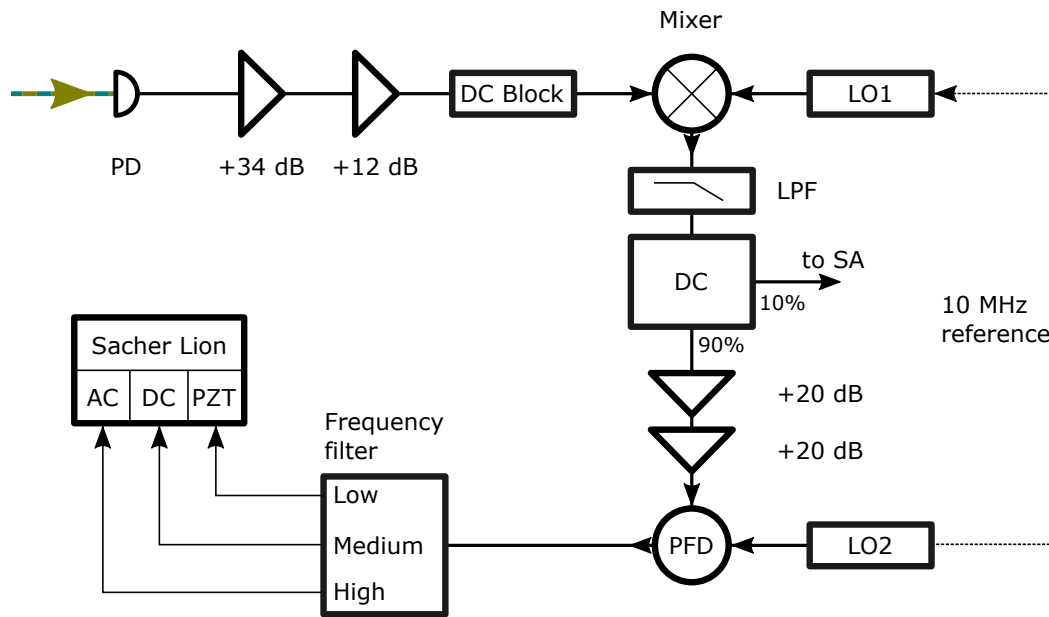
Figure 4.6: Sketch of the optical setup of the two phase locked lasers. Here the abbreviations have the following meaning: half-wave plate (HW), quarter-wave plate (QW), polarization spectroscopy (PS), polarization beam splitter cube (PBC), acousto optical modulator (AOM) and fast photodiode (PD).

sources that are phase-stable against each other. Here a direct digital synthesizer (DDS)[24] is used that can generate phase-stable sinusoidal signals with a frequency of up to $250\,\mathrm{MHz}$. Similar to the master laser, the main part of the slave laser light field is coupled into an optical fiber that is connected to the experimental setup.

Samples of both light fields are overlapped and mode matched using a 50/50 beam splitter cube and then detected via a fast photodiode[25]. Since the lasers are coupling the two ground states to the same excited state, respectively, they are detuned by the ground state hyperfine splitting of $9.192\,\mathrm{GHz}$. With the superimposed light fields on the detector, one observes a beat note at the difference frequency between the two light fields. The fast photodiode has a bandwidth of over $10\,\mathrm{GHz}$, enabling it to detect this beat signal. The non-interfering parts of the light fields are detected as a DC signal. In Fig. 4.7 a schematic of the processing of the beat signal after detection is shown. The signal from the fast photodiode is amplified using a $34\,\mathrm{dB}$ ultra low noise amplifier[26]. It is a bandpass amplifier with a frequency range from $8\,\mathrm{GHz}$ to $10\,\mathrm{GHz}$. A second amplifier[27] directly following after the low noise amplifier, adds another $12\,\mathrm{dB}$. The DC part of the signal is not of any use for the phase lock and can be removed using a DC-block. The

---

[24] Analog Devices AD9958
[25] EOT ET-4000 GaAs PIN detector
[26] Microsemi AUL-8010
[27] Minicircuits ZX60-14012L

Figure 4.7: Schematic of the photodiode signal processing. The signal is amplified and the non-oscillating parts are removed using a DC-Block. Afterwards it is frequency mixed with the output of a local oscillator (LO). To remove the sum frequency after the mixer the signal passes a low pass filter (LPF). The signal can be monitored by using a spectrum analyzer (SA) connected to a directional coupler (DC). After two additional amplification stages the phase is compared to a second local oscillator by a phase frequency detector (PFD). The output of the phase detector is divided into three paths covering differenz frequency ranges. The low frequency path is connected to the piezo element attached to the laser grating. The other paths manipulate the laser diode injection current.

remaining AC-signal is now mixed with the signal of a stable quartz oscillator[28] at 9.216 GHz. It is stabilized to an external 10 MHz reference signal. To mix both signals a, double balanced frequency mixer[29] is used. It only passes on the sum and the differential frequency, suppressing the input frequencies as well as higher harmonics. This step is required as most phase frequency detectors are only able to handle frequencies up to the MHz range.

A high rejection low pass filter[30] blocks the unused sum frequency signal. By connecting a spectrum analyzer to the 10 % output of the directional coupler the signal can be monitored. After further amplifying the signal with two amplifiers adding 20 dB each, the level of the signal is about 5 dBm. It is then fed into the phase frequency detector[31]. A RF signal generator[32] is used as the local oscillator for the detector and, in addition, provides the 10 MHz reference for

---

[28] Kuhne KU LO 92 PLL
[29] Minicircuits ZMX-10G
[30] Minicircuits VLFX-500
[31] Hittite HMC439QS16G
[32] Agilent N9310A

the previously mentioned quartz oscillator. The phase frequency detector outputs a voltage that is proportional to the phase difference between the two input signals.

The output voltage is divided into three control voltages via frequency filters. The low frequency ($< 100\,\mathrm{Hz}$) control voltage is forwarded to the piezo actuator that controls the tilt of the slave laser's grating. By changing the angle of the grating the length of the cavity changes, thus influencing the frequency at which the laser diode operates. The medium frequency ($< 100\,\mathrm{kHz}$) control voltage manipulates the injection current of the laser diode by utilizing the DC-coupled modulation input of the laser controller[33]. The bandwidth of this mode of control is limited by the inherent electronic bandwidth of the laser controller. These two modes of frequency control mainly serve to stabilize the laser to keep it within the range of the phase frequency detector. The high frequency ($< 10\,\mathrm{MHz}$) part of the control voltage is most important to achieve the required loop bandwidth and reduce the phase noise. The control voltage directly modulates the injection current via a Bias-T[34], that has a bandwidth of $100\,\mathrm{MHz}$. This phase lock system reduces the residual phase error of the laser system down to $0.04\,\mathrm{rad}^2$ between $100\,\mathrm{Hz}$ and $7.5\,\mathrm{MHz}$, resulting in an average phase deviation of about $200\,\mathrm{mrad}$.

4.3 Detection and data acquisition

This section describes the path from detecting the probing light field to collecting and processing the acquired data.

The main method to acquire information regarding the properties of the fiber-coupled atoms in this experiment is transmission spectroscopy. Here, the frequency of the probing laser is scanned over the $F = 4$ to $F' = 5$ transition of the D2-line. The power of the probing light field is on the order of a few pW, which equals to several million photons per second. To be able to precisely detect such relatively low photon numbers this experiment relies on a single photon counting module (SPCM). For each detected photon the SPCM generates a TTL pulse which is collected by a field programmable gated array (FPGA). The FPGA counts and sums up the TTL pulses that arrive in a specific time window, here referred to as bin size, of typically $10\,\mu\mathrm{s}$.

The resulting histogram is read out via a LabView program that is also used to display and process the acquired data. An example for the obtained histogram is shown in Fig. 4.8. The background at about 2 counts per bin is caused by the remaining Raman scattering of the blue-detuned trap laser. Starting at bin 50, bin 750 and bin 2500 the probing light field is switched on for $5\,\mathrm{ms}$ (500 bins) and scanned $\pm50\,\mathrm{MHz}$ around the frequency of the in-trap $F = 4$ to $F' = 5$ transition using an AOM. At resonance, the probing light field is completely absorbed by the atoms.

The observed transmission spectrum is shifted and broadened compared to a spectrum taken with free-space atoms in the MOT. The broadening is caused by the Zeeman sublevels as well as the tensor part of the AC Stark interaction, while the shift is mainly caused by the scalar part of the AC Stark interaction. By fitting the transmission spectrum $T(\Delta)$, using a saturated

---

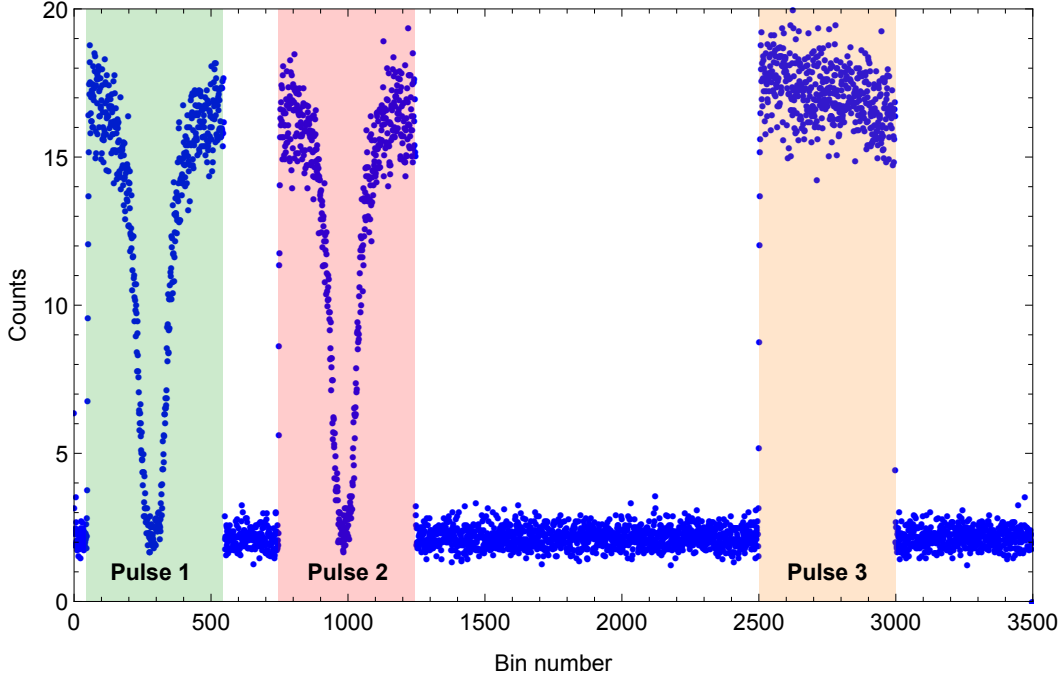[33] Sacher MLD-1000
[34] Sacher BT25-V2

Figure 4.8: Example for a raw transmission spectrum. There are three probing laser pulses starting at bin 50 in green, bin 750 in red and bin 2500 in orange, respectively. Each bin has a duration of $10\,\mu s$. The light field is scanned $\pm 50\,\mathrm{MHz}$ around the in-trap $F = 4$ to $F' = 5$ transition. Before the last pulse, all atoms were released from the trap.

Lorentzian line profile [29]

$$T(\Delta) = \exp\left(-\mathrm{OD}\,\frac{\Gamma^2}{\Gamma^2 + \Delta^2}\right), \tag{4.1}$$

the optical density (OD) can be directly extracted. Here Γ is the natural linewidth of the Cesium D2 transition for the nanofiber-trapped atoms and Δ is the detuning of the light field from the frequency of the in-trap $F = 4$ to $F' = 5$ transition of the D2 line. The OD depends on the number of trapped atoms, but also on the coupling strength between atoms and light field. This coupling is governed by the distance between atom and fiber as well as selection rules for the driven transition. This has to be taken into consideration when trying to infer an absolute number of trapped atoms from the optical density. For relative comparison between measurements with the same set of parameters this method is adequate, since the OD is still proportional to the number of atoms [45].

The first pulse on the left in Fig. 4.8, indicated by the green area, is taken right after the atoms are loaded into the fiber trap. It is used to measure the initial number of trapped atoms. This is necessary as there can be quite substantial fluctuations of the number of detected atoms for each experimental run. From the second pulse, indicated by the red area, one can infer the number of atoms left after preparation and manipulation of the trapped atoms. It determines the

outcome of the experiment. For the last pulse on the right, indicated by the orange area, the fiber based dipole trap was switched off, releasing all the trapped atoms. It is taken as a reference to incorporate power fluctuations of the probing laser due to, e.g., noise on the control voltage of the AOM. From these three peaks the ratio of the fitted OD of peak 2 and peak 1 is calculated. This ratio is the value used to quantify the outcome of the experiment.

The error bars that can be seen in the plots in Ch. 5 and Ch. 6 are calculated starting with the counting error of the SPCM. Assuming a Poisson distribution the error reads

$$\text{error} = \sqrt{\frac{\text{counts}}{\text{number of averages}}}. \tag{4.2}$$

These errors are employed as weights for the fit of the transmission spectrum, using the Lorentzian line profile in Eq. 4.1. Utilizing these weights, the fit determines the significance of each data point when calculating the OD. The uncertainties of each individual fit give the error bars depicted in the plots. For the plots where the ratio is shown, the error bars are calculated using error propagation with the errors of pulse 1 and pulse 2.

Slow-down and storage of fiber-guided light pulses

This chapter describes the path towards storing a weak classical light pulse in an ensemble of nanofiber-trapped Cesium atoms. The ability to store classical light pulses in so called optical memories is crucial for realizing all optical signal processing schemes. These memories are an intermediate step towards quantum memories, which are required for quantum information processing [65]. Quantum memories are, e.g., key elements of quantum repeaters [7], necessary for long distance quantum communication [9, 10]. The capacity to store optical light pulses has been shown, e.g., for rare-earth-doped crystals [66] as well as ultracold atoms in a free-space optical lattice [22] with storage times of about one minute. Regarding optical network-based applications fiber-integrated optical memories are preferable [67–69]. An experimental approach storing light pulses in a thermal Cesium vapor confined inside a hollow-core photonic-crystal fiber demonstrated storage times of about $30\,\text{ns}$ with an efficiency of about $27\,\%$ [68]. In another recent work it was demonstrated that photonic entanglement can be preserved during storage and retrieval in a cryogenically cooled erbium-doped fiber [69]. Storing nanofiber-guided light pulses done in a similar approach as will be described in this chapter, but without trapped atoms, has also been recently reported [70]. However, in their approach, only the probing light field was fiber-guided, all other light fields were free space.

The system presented in chapter 4 has the capability to significantly improve the performance of fiber-integrated quantum memories by suppressing decoherence mechanisms, such as movement of the atoms or coupling to the solid-state environment. This experiment relies on electromagnetically induced transparency (EIT), which will be further introduced in the following section. By carefully choosing specific parameters for the EIT scheme, the group velocity of a light pulse propagating through the atomic medium can be reduced to several ten meters per second. This can then be extended to storing and retrieving a classical light pulse. The first experimental realization of the latter in our system suffered from a number of limitations, which will be discussed in the final section of this chapter, together with some thoughts on possible improvements. The results presented in this chapter have been published in [31].

5.1 Electromagnetically induced transparency

When the frequency of a light field matches that of an atomic resonance, this resonant light field suffers high absorption. This effect can be avoided by using electromagnetically induced transparency (EIT). It is a well known effect [14] that can be understood as a destructive quantum interference of different possible transition paths between three distinct atomic energy states $|1\rangle$, $|2\rangle$ and $|3\rangle$. While the transition between $|1\rangle$ and $|2\rangle$ is forbidden, both are individually coupled to $|3\rangle$ via a probe and a control light field, respectively. In this system, the coupling to the excited state $|3\rangle$ is the only means of absorption. The strong control field with Rabi frequency Ω_c coherently couples states $|2\rangle$ to $|3\rangle$, effectively depumping $|2\rangle$. Similarly, the weak probe light field with Ω_p coherently couples state $|1\rangle$ to state $|3\rangle$.

One possible transition path for atoms initially in $|1\rangle$ is directly via the probe laser ($|1\rangle \rightarrow |3\rangle$) the other one is indirectly via the probe laser and control laser ($|1\rangle \rightarrow |3\rangle \rightarrow |2\rangle \rightarrow |3\rangle$). Here, the probability amplitude of the indirect path is equal to the probability amplitude of the direct path. As it is of opposite sign, this is leading to destructive interference. For a three-level atom there are several possible coupling schemes, of which the so called Λ-scheme, depicted in Fig. 5.1, is used in the experiment presented in this chapter.

One can gain a more detailed understanding of EIT when further examining the closely related physics of coherent population trapping (CPT) and the phenomenon of dark states. In CPT the atoms get transferred into a dark state where they are completely decoupled from the involved light fields. Considering the Λ-scheme from Fig. 5.1, the control field will optically pump atoms from $|2\rangle$ to $|1\rangle$ via $|3\rangle$. Likewise, the probe light field will optically pump atoms from $|1\rangle$ to $|2\rangle$ via $|3\rangle$. The total Hamiltonian of the system reads [14]
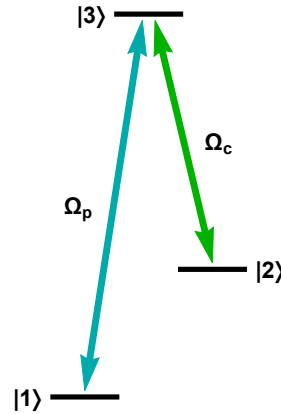
$$H = H_0 + H_{\text{int}}, \tag{5.1}$$

Figure 5.1: Basic scheme, referred to as Λ-scheme, suitable for EIT in a three or more level system. The transition between states $|1\rangle$ and $|2\rangle$ is dipole forbidden. Both states couple individually to $|3\rangle$ via light fields with a Rabi frequency Ω_p and Ω_c, respectively.

with the bare atomic Hamiltonian

$$H_0 = \hbar \sum_{i=1}^{3} \omega_i \left| i \right\rangle \left\langle i \right|, \tag{5.2}$$

and the atom-light interaction Hamiltonian

$$H_{\mathrm{int}} = -\frac{\hbar}{2} \begin{pmatrix} 0 & 0 & \Omega_{\mathrm{p}} e^{i\omega_{\mathrm{p}}t} \\ 0 & 0 & \Omega_{\mathrm{c}} e^{i\omega_{\mathrm{c}}t} \\ \Omega_{\mathrm{p}} e^{-i\omega_{\mathrm{p}}t} & \Omega_{\mathrm{c}} e^{-i\omega_{\mathrm{c}}t} & 0 \end{pmatrix}. \tag{5.3}$$

Here ω_i is the atomic state frequency, $\Omega_{\mathrm{p}} = d_{13} E_{\mathrm{p}} / \hbar$ as well as $\Omega_{\mathrm{c}} = d_{23} E_{\mathrm{c}} / \hbar$ are the Rabi frequencies of the respective light fields with the transition dipole moment d and the electric field amplitude E. The detuning of the probe and control light field frequencies ω_{p} and ω_{c}, respectively, from the atomic transition ω_{ij} is given by δ_{p} and δ_{c}. The eigenstates of this Hamiltonian are referred to as the dressed states of the system described by H. They are a superposition of the bare atomic eigenstates. Transforming H to a rotating frame with respect to the probe light field frequency ω_{p} and use the rotating wave approximation, neglecting fast oscillating terms, the eigenstates read for $\delta_{\mathrm{p}} = \delta_{\mathrm{c}} = 0$

$$\left| 0 \right\rangle = \frac{1}{\sqrt{\Omega_{\mathrm{c}}^2 + \Omega_{\mathrm{p}}^2}} \left(\Omega_{\mathrm{c}} \left| 1 \right\rangle - \Omega_{\mathrm{p}} \left| 2 \right\rangle \right) \tag{5.4}$$

$$\left| - \right\rangle = \frac{1}{\sqrt{2}} \left(\frac{1}{\sqrt{\Omega_{\mathrm{c}}^2 + \Omega_{\mathrm{p}}^2}} \left(\Omega_{\mathrm{p}} \left| 1 \right\rangle + \Omega_{\mathrm{c}} \left| 2 \right\rangle \right) - \left| 3 \right\rangle \right) \tag{5.5}$$

$$\left| + \right\rangle = \frac{1}{\sqrt{2}} \left(\frac{1}{\sqrt{\Omega_{\mathrm{c}}^2 + \Omega_{\mathrm{p}}^2}} \left(\Omega_{\mathrm{p}} \left| 1 \right\rangle + \Omega_{\mathrm{c}} \left| 2 \right\rangle \right) + \left| 3 \right\rangle \right). \tag{5.6}$$

From the equations above it is obvious that state $\left| 0 \right\rangle$ is a dark state, since it does not contain and couple to the excited state $\left| 3 \right\rangle$. The missing excitation path leads to an increasing number of atoms being coherently trapped in $\left| 0 \right\rangle$.

The main difference in the description of CPT and EIT is the ratio of the involved light fields Rabi frequencies. For CPT, they are of the same order of magnitude, while for EIT the control light field is much stronger than the probe light field. Considering $\Omega_{\mathrm{p}} \ll \Omega_{\mathrm{c}}$ in Eq. 5.4 to Eq. 5.6 results in

$$\left| 0 \right\rangle \approx \left| 1 \right\rangle \tag{5.7}$$

$$\left| - \right\rangle \approx \frac{1}{\sqrt{2}} \left(\left| 2 \right\rangle - \left| 3 \right\rangle \right) \tag{5.8}$$

$$\left| + \right\rangle \approx \frac{1}{\sqrt{2}} \left(\left| 2 \right\rangle + \left| 3 \right\rangle \right). \tag{5.9}$$

In this situation, the dark state $\left| 0 \right\rangle$ coincides with the atomic ground state $\left| 1 \right\rangle$, effectively decoupling it from the probe laser.

For a quantitative description of EIT, simulating the outcome of an experimental realization, a model including additional damping terms has to be used. The master equation in the Lindblad form is used to determine the time evolution of the atomic level's population and coherences. The atomic ensemble can be described using the density matrix ρ_{ij}, where the diagonal elements ($i = j$) gives the population and the off-diagonal elements ($i \neq j$) the coherences of the system. These coherences ρ_{ij} can be used to write down the polarization density

$$P_{\text{at}} = N d_{ij}\, \rho_{ij}, \tag{5.10}$$

induced in the atomic medium by the applied light fields driving a transition from $|i\rangle$ to $|j\rangle$. Here, N is the number of atoms and d_{ij} the dipole matrix element. Another way to express the polarization density is by using the electric susceptibility, that describes the linear response of the medium to near-resonant light with electric field E

$$P_{\text{at}} = \epsilon_0\, \chi_{\text{e}}\, E, \tag{5.11}$$

with the free space electric permittivity ϵ_0. Combining Eq. 5.10 and Eq. 5.11, one obtains for the susceptibility

$$\chi_{\text{e}} = \frac{N d_{ij}\rho_{ij}}{\epsilon_0 E} = \frac{N d_{ij}^2 \rho_{ij}}{\hbar \epsilon_0 \Omega}, \tag{5.12}$$

with the Rabi frequency $\Omega = d_{ij}E/\hbar$. As the ρ_{ij} are complex valued the susceptibility consists of a real and an imaginary part, with the real part being linked to the refractive index n and the imaginary part to the absorption A.

To calculate the dynamics of the density matrix, one has to solve the master equation in Lindblad form

$$\dot{\rho}_{ij}(t) = -\frac{i}{\hbar}\left[\hat{H}, \rho_{ij}(t)\right] + \mathcal{L}\left(\rho_{ij}(t)\right) \tag{5.13}$$

for the three-level system with the Hamiltonian $H = H_0 + H_{\text{int}}$. The dephasing and decoherence mechanisms of the system are taken into account using damping terms included in $\mathcal{L}(\rho_{ij}(t))$ reading [14]

$$
\begin{aligned}
\mathcal{L}\left(\rho_{ij}(t)\right) &= \frac{\gamma_{21}}{2}\left(2\sigma_{12}\rho\sigma_{21} - \sigma_{22}\rho - \rho\sigma_{22}\right) + \frac{\gamma_{31}}{2}\left(2\sigma_{13}\rho\sigma_{31} - \sigma_{33}\rho - \rho\sigma_{33}\right) + \\
&\quad + \frac{\gamma_{32}}{2}\left(2\sigma_{23}\rho\sigma_{32} - \sigma_{33}\rho - \rho\sigma_{33}\right),
\end{aligned} \tag{5.14}
$$

with $\sigma_{ij} = |i\rangle\langle j|$. The γ_{ij} are the coherence decay rates where γ_{31} and γ_{32} consist of the total spontaneous emission rate of state $|3\rangle$ and include dephasing. For γ_{21}, only dephasing is taken into account. With this, one obtains for the off-diagonal elements of $\dot{\rho}$ in Eq. 5.13

$$\dot{\rho}_{21} = i\rho_{21}\left(\frac{\gamma_{21}}{2i} + \omega_1 - \omega_2\right) + i\rho_{31}\frac{\Omega_{\text{c}}}{2}e^{i\omega_{\text{c}}t} - i\rho_{23}\frac{\Omega_{\text{p}}}{2}e^{-i\omega_{\text{p}}t} \tag{5.15}$$

$$\dot{\rho}_{31} = i\rho_{31}\left(\frac{\gamma_{31}}{2i} + \omega_1 - \omega_3\right) + i\rho_{21}\frac{\Omega_{\text{c}}}{2}e^{-i\omega_{\text{c}}t} + i(\rho_{11} - \rho_{33})\frac{\Omega_{\text{p}}}{2}e^{-i\omega_{\text{p}}t} \tag{5.16}$$

$$\dot{\rho}_{32} = i\rho_{32}\left(\frac{\gamma_{32}}{2i} + \omega_2 - \omega_3\right) + i\rho_{12}\frac{\Omega_{\text{p}}}{2}e^{-i\omega_{\text{p}}t} + i(\rho_{22} - \rho_{33})\frac{\Omega_{\text{c}}}{2}e^{-i\omega_{\text{c}}t}. \tag{5.17}$$

For the purpose of this work, only the atom's optical response to the probe field is of further interest. Therefore, only the solution of ρ_{31} will be considered regarding the susceptibility. As a starting condition, it is assumed that all atoms start in state $|1\rangle$ resulting in $\rho_{11} = 1$ and $\rho_{22} = \rho 33 = 0$. Expressing ρ_{31} in the rotating frame ($\tilde{\rho}_{31} = \rho_{31}\, e^{i\omega t}$) and including the two-photon detuning $\Delta = \delta_{\mathrm{p}} - \delta_{\mathrm{c}}$, with the probe and control light field detuning δ_{p} and δ_{c} respectively, Eq. 5.16 and Eq. 5.15 simplify to

$$\dot{\tilde{\rho}}_{21} = i\tilde{\rho}_{21}\left(\Delta - \frac{\gamma_{21}}{2i}\right) + i\tilde{\rho}_{31}\frac{\Omega_{\mathrm{c}}}{2} \tag{5.18}$$

$$\dot{\tilde{\rho}}_{31} = i\tilde{\rho}_{31}\left(\delta_{\mathrm{p}} + \frac{\gamma_{31}}{2i}\right) + i\tilde{\rho}_{21}\frac{\Omega_{\mathrm{c}}}{2} + i\frac{\Omega_{\mathrm{p}}}{2}. \tag{5.19}$$

This simplification includes the additional important assumption that we are in the weak probing limit where $\Omega_{\mathrm{p}} \ll \Omega_{\mathrm{c}}$. From the equations above, one can obtain the steady state solution of Eq. 5.19

$$\tilde{\rho}_{31} = \frac{\Omega_{\mathrm{p}}\,(2\Delta - i\gamma_{21})}{|\Omega_{\mathrm{c}}|^2 + (\gamma_{31} + 2i\delta_{\mathrm{p}})(\gamma_{21} + 2i\Delta)}. \tag{5.20}$$

By combining Eq. 5.12 with Eq. 5.20, one obtains for the linear susceptibility

$$\chi_{\mathrm{e}} = \frac{Nd_{ij}^2}{\epsilon_0 \hbar}\frac{(2\Delta + i\gamma_{21})}{|\Omega_{\mathrm{c}}|^2 + (\gamma_{31} + 2i\delta_{\mathrm{p}})(\gamma_{21} + 2i\Delta)}. \tag{5.21}$$

Figure 5.2: (a) Imaginary part of the susceptibility χ_{e} versus the probe light field's detuning δ_{p}. The solid line shows the absorption of a probe light field in the EIT regime, the dashed line shows the absorption in a two-level system, i.e., without the coupling laser. (b) Real part of the susceptibility χ_{e} versus the probe light field's detuning. The solid line shows the refractive index of the medium in the EIT regime, the dashed line shows the refractive index in a two-level system. In both graphs $\Delta = \delta_{\mathrm{p}}$ and $\gamma_{21} = 0$.

(a)

(b)
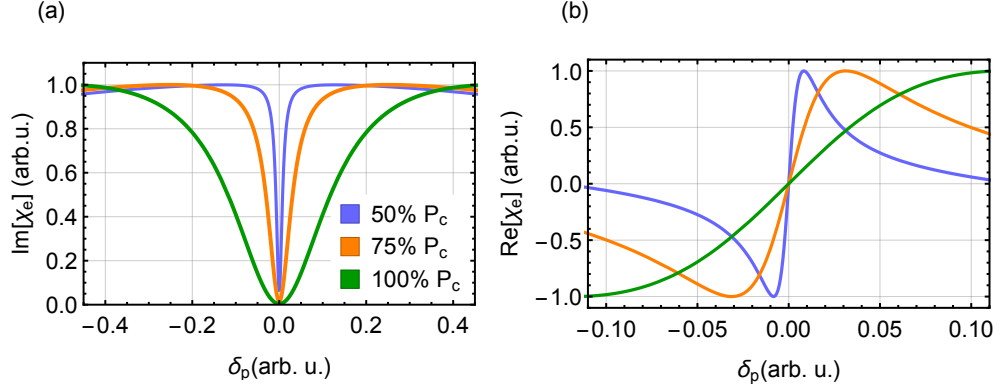
Figure 5.3: (a) Imaginary part of the susceptibility χ_e and (b) real part of the susceptibility χ_e versus the probe light field's detuning for three different control light field powers P_c. Parameters are the same as in Fig. 5.2 and P_c is given with respect to an arbitrary initial control field power.

Separating the term on the right into its real and imaginary parts, one obtains the dispersion and the absorption of the atomic medium. In Fig. 5.2, the imaginary part and the real part are plotted versus the probe light field's detuning for a resonant control light field. From the solid line in Fig. 5.2(a), one can directly see the narrow dip in the absorption around resonance where the probe light field does not couple to the atomic ensemble anymore. Figure 5.2(b) shows the refractive index n of the medium „seen" by the probe light field. The solid line shows a very steep variation of the refractive index, with implications that will be discussed later on in this chapter. A parameter that can be easily changed is the control light field power $P_c \propto \sqrt{\Omega_c}$. As evident from Fig. 5.3(a), a reduced P_c leads to a narrower EIT window in the probe light field's absorption spectrum. Figure 5.3(b) indicates that the reduction of P_c increases the steepness of the variation of the refractive index with the probe field detuning.

Experimental observation of EIT with a nanofiber-trapped atomic ensemble

A schematic of the experimental system is shown in Fig. 5.4(a). The running-wave trapping light field with a free-space wavelength of $783\,\mathrm{nm}$ has a power of $7\,\mathrm{mW}$, the standing-wave trapping light field at $1064\,\mathrm{nm}$ wavelength has a power of $0.65\,\mathrm{mW}$ per beam. The trapping potential consists of two diametric linear arrays of trapping sites along the nanofiber, located at a distance of about $225\,\mathrm{nm}$ from the fiber surface. Each trapping site contains at most one atom and offers sub-wavelength confinement in all three spatial dimensions [71]. These trap properties are highly advantageous because collisional broadening of atomic transitions is absent and motional dephasing is strongly suppressed.

The experiments demonstrated in this chapter are realized using the Cesium hyperfine levels shown in Fig. 5.4(c). The quantization axis is chosen to be along the applied homogeneous magnetic field $\mathbf{B}_{\mathrm{off}}$ indicated in Fig. 5.4(a) and (b). The Λ-scheme that is utilized for this implementation of EIT is formed with the two Zeeman ground states $|1\rangle = |F = 3, m_F = +3\rangle$ and
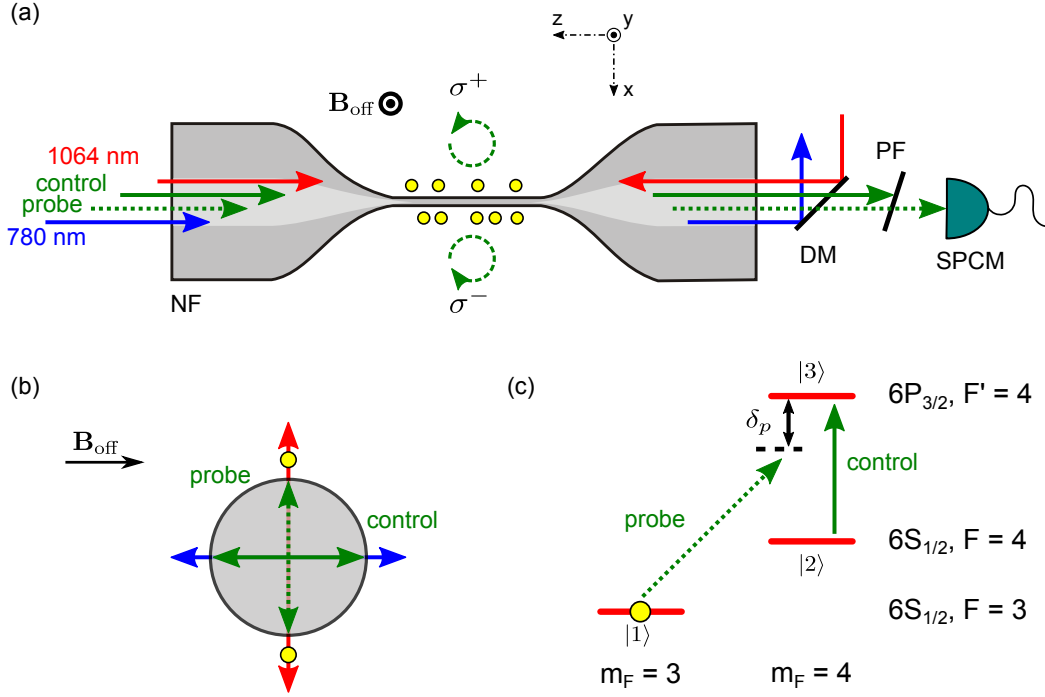
Figure 5.4: (a) Schematic of the experimental setup including the nanofiber (NF), the trapping, probe, and control laser fields, as well as the single-photon counting module (SPCM). The atoms are displayed as yellow discs. The polarization of the probe field above and below the nanofiber is indicated by the dashed circular arrows. The trapping light fields are coupled in and filtered out using dichroic mirrors (DM). A polarization filter (PF) in front of the SPCM separates the control laser from the probe light field. A homogeneous magnetic field $\mathbf{B}_{\mathrm{off}}$ is applied along the y-axis as indicated. (b) Cross-sectional view of the nanofiber, illustrating the orientations of the principal axes of quasi-linear polarizations of the nanofiber-guided fields. (c) Relevant Zeeman sublevels of the trapped Cesium atoms. The states $|1\rangle$, $|3\rangle$, and $|2\rangle$ form the Λ-system used in the experiments. The transitions driven by the probe (σ^+) and the control (π) laser fields are also indicated. This is only realized for atoms on one side of the fiber. On the other side of the fiber the probe light field is σ^- polarized. δ_{p} is the detuning of the probe field frequency from the $|1\rangle$ to $|3\rangle$ transition. The quantization axis is chosen along the direction of the magnetic field.

$|2\rangle = |F=4, m_F=+4\rangle$, as well as the Zeeman excited state $|3\rangle = |F'=4, m_{F'}=+4\rangle$ on the D2 Line. The probe field which couples the states $|1\rangle$ and $|3\rangle$ as well as the control field which couples the states $|2\rangle$ and $|3\rangle$ are launched into the nanofiber. They are co-propagating and are both quasi-linearly polarized in the nanofiber. The alignment of their principal polarization axes is as shown in Fig. 5.4(b). Two measures are taken to prevent the control light field to influence the detection of the probe light field. The first one is using a Glan-Thompson prism, that only transmits a specific linear polarization, aligned such that the control light field is maximally suppressed. The second is using a Fabry-Pérot filter cavity that acts as a very narrow bandpass filter,

51

see Ch. 4.2.1.

To drive the transitions as specified above, one can take advantage of the particular polarization properties of the nanofiber-guided light fields that are described in more detail in Ch. 2.2.1. At the position of the atoms, the control laser field is π-polarized. At the same time, the probe light field is almost perfectly σ^+-polarized above and σ^--polarized below the nanofiber, as seen in Fig. 5.4(a). The Zeeman shifts induced by $\mathbf{B}_{\text{off}}$ ensure that the probe light field almost exclusively couples to the atoms above the nanofiber [45, 46]. The control light field is always kept resonant with the $|2\rangle \rightarrow |3\rangle$ transition. The probe light field of frequency ω_p is phase-locked to the control light field, see Ch. 4.2.3, and detuned by $\delta_p = \omega_p - \omega_{31}$ from the $|1\rangle \rightarrow |3\rangle$ transition at frequency ω_{31}.

To show that this setup exhibits the expected behavior, the probe light field's transmission through the nanofiber under EIT conditions is measured. After loading atoms into the nanofiber-based trap in their $F = 3$ hyperfine ground state, the magnetic offset field is slowly increased from $0\,\text{G}$ to $26\,\text{G}$. Through the process of adiabatic magnetization, most of the atoms are prepared in the state $|1\rangle$ (see Ch. 3.3.2). Then, the probe and the control fields are switched on and the detuning δ_p is scanned over $60\,\text{MHz}$ within $500\,\mu\text{s}$. The transmission spectrum $T(\delta_p)$ is determined by measuring the transmitted power with and without atoms using a single photon counting module (SPCM) with a bin size of $1\,\mu\text{s}$. Figure 5.5(a) shows the resulting transmission spectrum for a control power of $P_c = 26\,\text{pW}$, the probe power is $P_p = 2.9\,\text{pW}$. One observes a narrow EIT transmission window with a full width at half maximum (FWHM) of about $300\,\text{kHz}$ and a maximum transmission of about $70\,\%$ at resonance. One can model the probe transmission as

$$T(\delta_p) = \left| h(\delta_p) \right|^2 , \tag{5.22}$$

with the transfer function [14]

$$h(\delta_p) = \exp\left(i\,\eta\,\chi_e(\delta_p)/2 \right) , \tag{5.23}$$

where χ_e is the susceptibility from Eq. 5.21. Here the quantity η is the resonant optical depth in the absence of a control field. The obtained fit function, shown as an orange line in Fig. 5.5(a), agrees well with the data. Fixing $\gamma_{31} = 2\pi\,6.4\,\text{MHz}$ based on independent measurements [46], one obtains $\gamma_{21} = 2\pi(49 \pm 18)\,\text{kHz}$, $\Omega_c = 2\pi(2.4 \pm 0.1)\,\text{MHz}$ and $\eta = 5.9 \pm 0.2$ as results from the fit procedure. Given the high absorption per atom of $3.8\,\%$ [72], the measured optical depth corresponds to the contribution of only 160 atoms in the state $|1\rangle$.

The value of γ_{21} matches the expectations based on previously done microwave spectroscopy on the ground state manifold [46] and is promising for light storage. Moreover, it is about one order of magnitude smaller than the measured width of the EIT window. The minimal achievable width of the transmission window is on the order of $\gamma_{21}/\sqrt{\eta}$ [14]. This is experimentally confirmed in Fig. 5.5(b), where the control power is set to $P_c = 0.33\,\text{pW}$. For this measurement $T(\delta_p)$ is determined for each detuning individually by recording the transmitted power of the probe light field during $10\,\mu\text{s}$. The power of the probe field, $P_p = 1.7\,\text{pW}$, is now comparable to the control field power. Therefore it is necessary to wait about $55\,\mu\text{s}$ after the probe and the control field have been switched on, until the atomic ensemble is pumped into the dark state [73]. A longer waiting time leads to no further change of the transmission spectrum. With this setup,
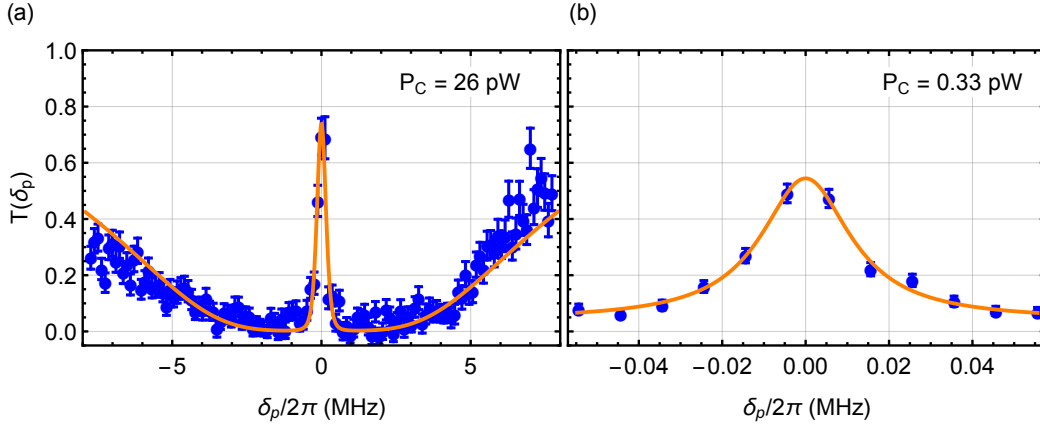
Figure 5.5: Transmission spectrum of the nanofiber-guided probe field under EIT conditions. (a) Transmission window featuring a width considerably smaller than the natural line width on an optically dense background. The control power here is $P_c = 26\,\text{pW}$ and the probe power is $P_p \approx 2.9\,\text{pW}$. The orange line is a fit to the data based on Eq. (5.22). The spectrum is averaged over 300 measurements. (b) For a smaller P_c of $0.33\,\text{pW}$, the observed transmission window is about 10 times narrower. The orange line is the result of a Lorentzian fit, which was used since the transfer function in Eq. (5.22) is only valid for $P_p \ll P_c$. Here, $P_p = 1.7\,\text{pW}$. Each data point is an average over 60 measurements.

it is possible to measure a transmission window with a Lorentzian FWHM of only $26\,\text{kHz}$ and a transmission of about $60\,\%$.

5.2 Slow light

The observed narrow EIT window implies a steep modulation of the refractive index n of the atomic medium around $\delta_p = 0$, as also seen in Fig. 5.2(b). It results in a significant reduction of the group velocity v_g of the probe pulse since it scales as [14]

$$v_g = \frac{d\omega_p}{dk_p} = \frac{c}{n + \omega_p \left(\frac{dn}{d\omega_p} \right)}. \tag{5.24}$$

This reduction of the group velocity of a resonant light field with only negligible losses is referred to as slow light [74]. In addition to the overall reduced group velocity, an optical pulse launched into the medium becomes spatially compressed in propagation direction [75] as long as the pulse is inside the medium. This effect is caused by the difference in propagation speed inside and outside the medium. Due to this compression, some part of the pulse's electromagnetic energy is stored as an excitation in the atoms, that travels in the medium alongside the pulse.
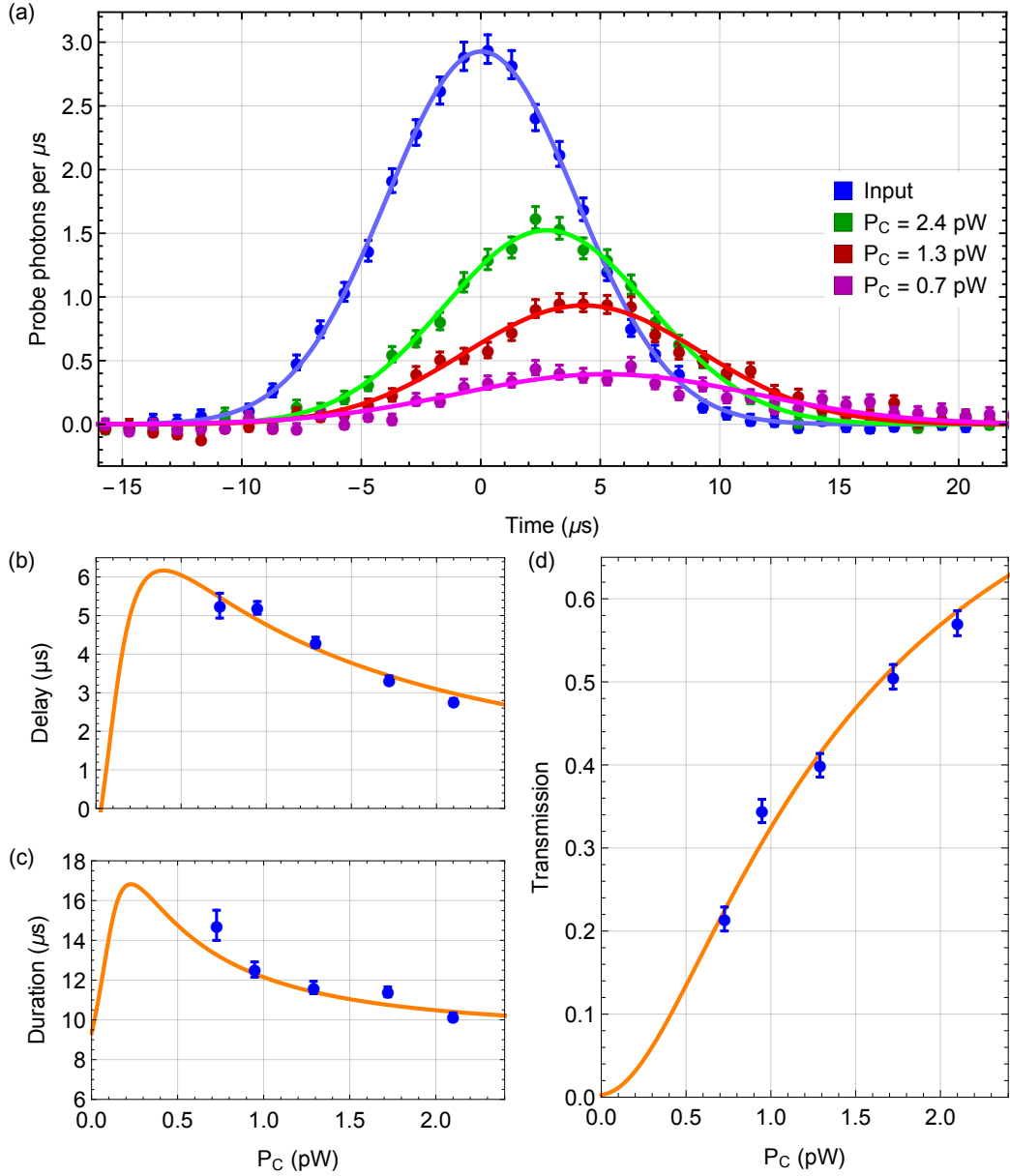
Figure 5.6: (a) Time traces of probe pulses transmitted through the atom–nanofiber system under EIT conditions. The solid lines are Gaussian fits to the data. Each point is the result of the average over 5 pulses per atomic ensemble and over 800 experimental runs. The bin size is $1\,\mu s$. The error bars are as in Fig. 5.5. (b) Pulse delay, (c) pulse duration, and (d) pulse transmission as a function of the control light field power P_c. The orange lines are the results of a global fit of the data sets in (b)–(d). The error bars here are the standard errors of the Gaussian fits.

For the scope of this work, studying the propagation of a resonant probe pulse through the nanofiber under EIT conditions is of great interest. To this end, a probe pulse with Gaussian temporal profile and a FWHM of $\tau = 9.4\,\mu$s is launched into the nanofiber. The pulse contains on average about 30 photons, corresponding to a peak power of $0.7\,$pW. The duration of the pulse was chosen such, that it spectrally fits into the EIT window, while still having a good signal to nose ratio. The recorded transmitted probe pulse is then compared to a reference pulse taken in the absence of trapped atoms. This is repeated five times with each ensemble of atoms and for 800 experimental runs, yielding a total of 4000 averages. The results are shown in Fig. 5.6(a) for a selection of control field powers P_c. Here, the data points show the number of detected probe photons per time bin of $1\,\mu$s. The solid lines are Gaussian fits to the experimental data. From this figure, it is already visible that the pulses are delayed with respect to the reference pulse.

This measurement is then repeated for several different values of P_c. For each power, the delay, duration (FWHM) and transmission of the probe pulse are inferred using a Gaussian fit, see Fig. 5.6(b), (c) and (d), respectively. One can observe that for decreasing P_c the delay of the pulse increases. At the same time, the transmitted power is reduced and the pulse FWHM increases. This behavior fully matches the expectations for this system. The spectral width of the EIT window is reduced with decreasing P_c. The associated steeper modulation of the refractive index leads to smaller group velocities, made visible by the increased delay. At the same time, an increasing part of the pulse spectrum is outside of the EIT window. This leads to both, absorption and distortion, of the transmitted probe pulse.

One can simulate the experiment using the transfer function $h(\delta_p)$ in Eq. (5.23). Here the optical depth η, a common scaling factor for all control field Rabi frequencies Ω_c, and γ_{21} are left as adjustable parameters. Fitting the outcome of the simulation to the experimental data yields the orange solid lines in Fig. 5.6(b)–(d). The agreement with the data is very good for $\gamma_{21} = 2\pi(20 \pm 2)\,$kHz, $\Omega_c = 2\pi(353 \pm 26)\,$kHz at $P_c = 1\,$pW and $\eta = 6.0 \pm 0.7$. The value for γ_{21} is consistent with the analysis in Fig. 5.5(a) and the value for Ω_c is close to the prediction of about $290\,$kHz considering $P_c = 1\,$pW. Given these parameters, one can expect that even longer delays can be observed by lowering P_c while simultaneously increasing the pulse duration. This is confirmed by launching pulses of duration $\tau = 93\,\mu$s into the medium with $P_c = 0.33\,$pW. In this case, one finds a delay of $(22 \pm 1)\,\mu$s at a transmission of $(13.6 \pm 0.5)\,\%$. Given the length of the atomic sample of about $1\,$mm, this corresponds to a group velocity of only about $50\,$m/s.

5.3 Storage of weak coherent pulses

The slow light technique can be readily extended to storage and on-demand retrieval of light pulses. In order to stop the pulse, the control power is reduced to zero while the light propagates through the medium. Once the control field is switched off, the electromagnetic field energy is completely converted into a spin-wave excitation within the atomic ensemble. The retrieval of the light pulse is triggered by switching the control field back on. To circumvent the increased pulse absorption that occurs when the width of the EIT window decreases with reduced P_c, it is necessary to ramp down P_c adiabatically [11]. The capability of this system for storage and on-demand retrieval is experimentally verified for a probe light pulse with a FWHM of $\tau = 0.2\,\mu$s that contains 0.8 photons on average and is launched into the nanofiber. This short pulse allows a
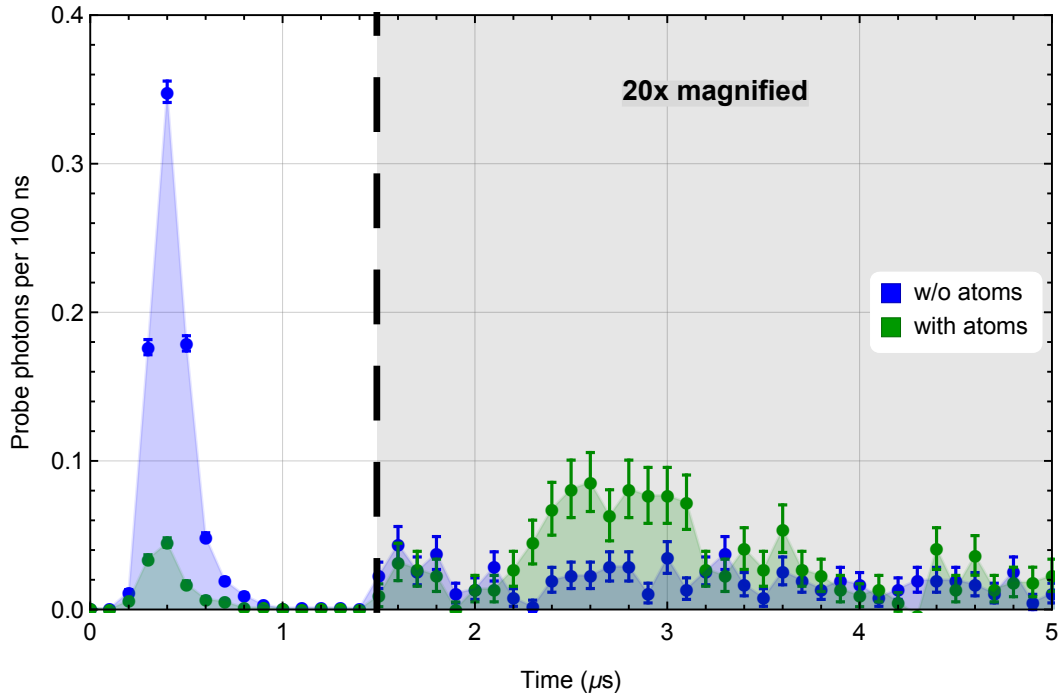
Figure 5.7: Storage of light in a nanofiber-trapped ensemble of cold atoms. A pulse of duration $\tau = 0.2\,\mu\text{s}$ is launched into the nanofiber and stopped inside the atomic medium by reducing the control laser power P_c to zero. After $1\,\mu\text{s}$, P_c is increased to its initial value, and the pulse is retrieved and recorded by the SPCM. Here, $B_{\text{off}} = 15\,\text{G}$, the bin size is $100\,\text{ns}$, and the data is averaged over 55 pulses per atomic ensemble and over 1600 experimental runs (2400 for reference).

reasonable signal to noise ratio. The control power P_c is ramped down linearly within $1\,\mu\text{s}$, while the probe pulse propagates through the atomic ensemble. After a holding time of another $1\,\mu\text{s}$, P_c is ramped up again to its initial value. The stored pulse is then released from the medium and detected with the SPCM. This procedure is repeated 55 times with each atomic ensemble and for 1600 experimental runs, giving a total of 88 000 averages. The resulting time trace is shown in Fig. 5.7. The reference pulse is recorded in a similar manner by repeating the same experiment without trapped atoms. From the figure it can be seen, that the light pulse is indeed retrieved with about $2\,\mu\text{s}$ delay with respect to the reference pulse. The small leakage, indicated by the small green peak on the left, is caused by imperfect polarizations and a limited optical density. The measured combined storage and retrieval efficiency of this memory is $(3.0 \pm 0.4)\,\%$.

5.4 Limitations and possible improvements

Under ideal conditions, and in particular in the absence of decoherence, the maximum attainable storage and retrieval efficiency depends only on the optical depth η [76]. In order to identify

the limiting factors for the efficiency for our settings, the experiment is simulated according to [76]. This model assumes that the probe pulse is a quantum field described by $\mathcal{E}$ with optical polarization P that is mapped onto a spin-wave excitation described by S upon entering the medium. After leaving the medium, S is transferred back to the outgoing optical mode $\mathcal{E}$. This model allows one to calculate the full time trace of the pulse which is partially directly transmitted, and partially stored and retrieved. To this end, the equations of motion for this system need to be solved [76]

$$\partial_t \mathcal{E}(z,t) = ig\sqrt{N}P(z,t) - c\partial_z \mathcal{E}(z,t) \tag{5.25}$$

$$\partial_t P(z,t) = -(\gamma + i\delta)P(z,t) + ig\sqrt{N}\mathcal{E}(z,t) + i\Omega_c S(z,t) \tag{5.26}$$

$$\partial_t S(z,t) = i\Omega_c P - \gamma_s S(z,t). \tag{5.27}$$

Here N is the atom number, c the speed of light, z the coordinate along the fiber axis, g the atom-photon coupling, δ the detuning from the excited state, γ the polarization decay rate and γ_s the spin-wave decay rate. In addition to the measured value of η, the parameter $\gamma_s = \gamma_{21} = 2\pi\,20\,\text{kHz}$ is taken as inferred from the data in Fig. 5.6, and $\gamma = \gamma_{31} = 2\pi\,6.4\,\text{MHz}$ as before. The simulation result is shown in Fig. 5.8(a) (solid green line). It accurately reproduces the measured time trace of the probe pulse for $\Omega_c(t = 0) = 2\pi\,2.24\,\text{MHz}$. Given the value of $P_c(t = 0)$ used, however, the calculation results in $\Omega_c \approx 2\pi\,0.6\,\text{MHz}$. The discrepancy between these two values is not yet fully understood and might be caused by a drift of the experimental conditions after the calibration of the power of the control field inside the nanofiber. Given the very good agreement between the measured and the simulated time traces, however, it is still feasible to use the simulation to identify the mechanisms that decrease the memory efficiency.

The simulations show, that this reduction is due to contributions from ground-state decoherence, insufficient control power, and a non-optimal control field ramp. The lack of control field
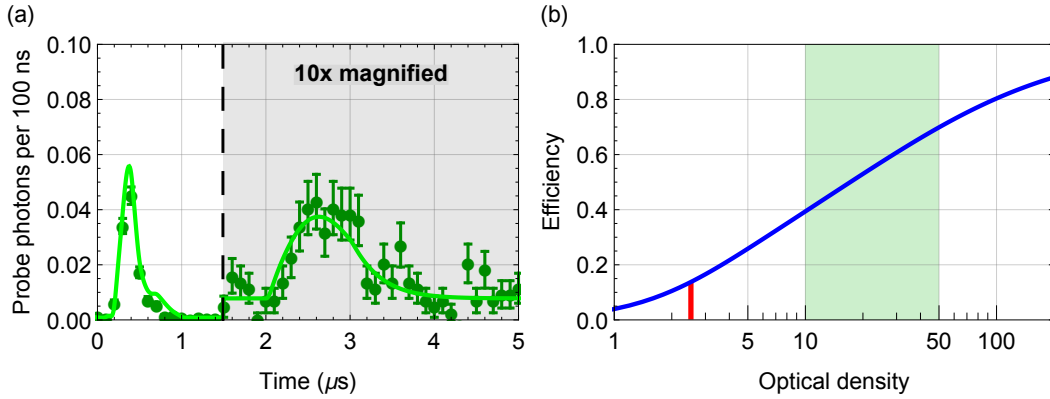
Figure 5.8: (a) Simulation of the experiment (solid line) fitted to the experimental data (green data points) from Fig. 5.7. (b) Calculated attainable storage and retrieval efficiency in dependence of the number of nanofiber-trapped atoms. The solid red line marks the optical density achieved during this experiment. The green area marks the range of optical densities that are within the reach of the current experimental setup.
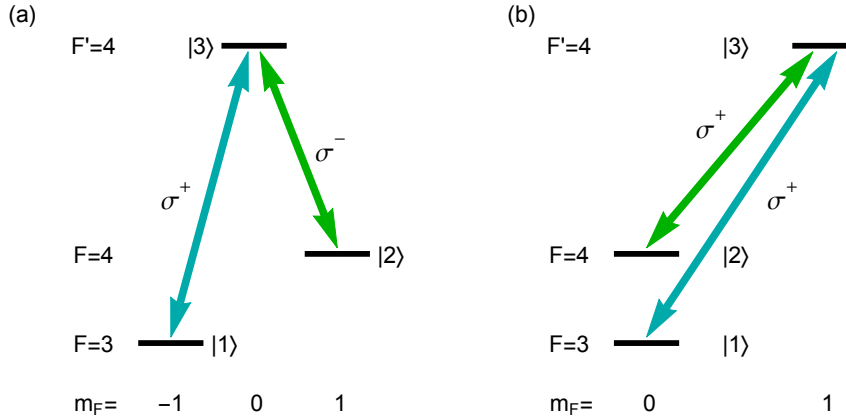
Figure 5.9: Examples for EIT on the clock transition.

power and the non-optimal ramp were caused by assumptions we made at that time, that turned out to be inaccurate. The control field power can be directly increased. To optimize the control field ramp, an arbitrary function generator can be added to be able to generate more involved control field ramps. Concerning decoherence, it has been shown that the magnetic field-insensitive $m_F = 0$ hyperfine ground state exhibits coherence times on the order of a millisecond in this experimental setup [77]. To transfer atoms to this Zeeman state they can be optically pumped using a laser resonant on the D1-line of Cesium, polarized perpendicular to the plane where the atoms are trapped [45]. Two possible realizations of EIT incorporating the clock transition are shown in Fig. 5.9.

Additional cooling of the trapped atoms, e.g., based on microwave sideband-cooling, as well as techniques to cancel the trap-induced differential light shifts of the ground states can bring further improvements. To increase the maximally achievable efficiency, the number of trapped atoms needs to be raised. Figure 5.8(b) shows the dependency of the efficiency on the optical density. At an optical density of $\eta = 2.4$, as it was during this experiment, the optimal efficiency is 13%. For optical densities that are within the reach of this experiment (green area in the figure) an efficiency of up to 70% is expected. The optical depth of the atomic ensemble could be increased by, e.g., loading more atoms into the trap via a larger spatial overlap of the initial cold atom cloud and the nanofiber.

In order to operate an optical memory in the quantum regime, low noise operation is an essential requirement. The waveguide-geometry in combination with the large optical depth per atom in this nanofiber-based system allows one to work with only a couple hundred atoms. This is a low number when compared to typical free-space experiments, that require orders of magnitude more atoms. This smaller number of atoms reduces read-out noise that would originate from imperfect atomic state preparation. In the work presented in this chapter, classical light pulses containing less than one photon on average were stored and retrieved. This indicates that the noise characteristics of the presented optical memory should also allow one to store quantum information and entanglement.

Microwave manipulation of nanofiber trapped atoms

For atoms confined in optical microtraps, elliptical polarization components of the required trapping light fields give rise to Zeeman state-dependent energy shifts [78]. This effect is equivalent to the interaction of a fictitious magnetic field with the trapped atoms. A spatially varying ellipticity of the light field introduces a gradient of the light induced fictitious magnetic field along the direction of atomic motion. The spatial variation of the light field's ellipticity is an inherent feature of optical microtraps due to the strong confinement of the trapping light fields [79,80]. So far, this is usually considered to be detrimental, as it potentially leads to dephasing, reduced efficiencies in optical pumping or additional heating [81]. This chapter focuses on investigating and exploiting the effects that come with the existence of these state-dependent trapping potentials in our system. To this end, we use the coupling between the external degree of freedom, in form of the motional state, and the internal degree of freedom, in form of the hyperfine level and the respective Zeeman state. It is described in more detail in chapter 3.3. First, this coupling will be utilized to get a very good estimate for the azimuthal temperature of the nanofiber-trapped atoms using microwave spectroscopy. This will be followed by introducing two methods to manipulate the state-dependence of the trapping potential. Equipped with the tools demonstrated so far, a cooling scheme based on microwave sideband cooling can be realized. All results presented in this work have been published in [32].

6.1 Microwave spectroscopy as a probe for nanofiber-trapped atoms

The experimental setup used for the measurements presented in this chapter is schematically shown in Fig. 6.1. The running-wave field with a free-space wavelength of $783\,\text{nm}$ has a power of $17.1\,\text{mW}$, the standing-wave field at $1064\,\text{nm}$ wavelength has a power of $1.25\,\text{mW}$ per beam. The trapping potential consists of two diametric linear arrays of individual trapping
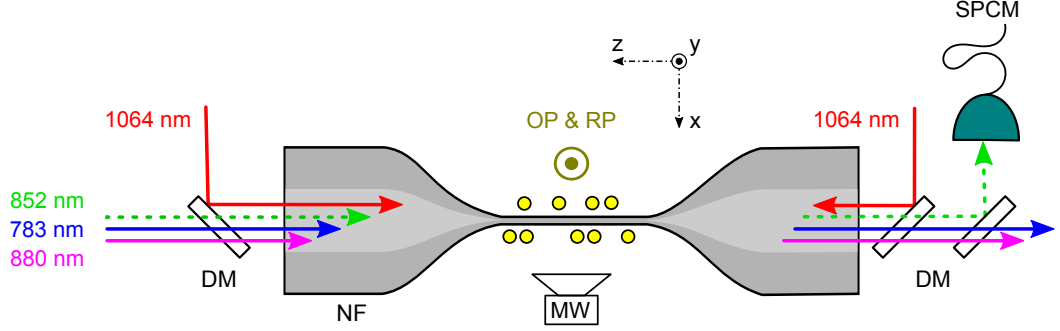
Figure 6.1: Schematic of the experimental setup including the nanofiber (NF), the light fields and the single-photon counting module (SPCM). OP and RP indicate external light fields for optical pumping (OP) and repumping (RP). The microwave (MW) can be used to drive transitions between the ground state manifolds.

sites along the nanofiber, located at a distance of about $290\,\mathrm{nm}$ from the nanofiber surface. By applying a microwave field at a frequency close to the hyperfine splitting between the $F = 3$ and $F = 4$ ground state manifolds, one can drive transitions from a state $|g\rangle = |F, m_F, n\rangle$ to $|e\rangle = |F', m_F', n'\rangle$. Here, m_F is the projection of the total angular momentum $\mathbf{F}$ onto the quantization axis, n the respective quantum number for the vibrational state, and the prime index indicates the final state of the microwave transition. The transition strength depends on the effective Rabi-frequency $\Omega_{n,n'}$ given by

$$\hbar\Omega_{n,n'} = \langle F', m_F', n'| \hat{V}_{\mathrm{MW}} |F, m_F, n\rangle . \tag{6.1}$$

The microwave coupling Hamiltonian $\hat{V}_{\mathrm{MW}} = \hat{V}_{\mathrm{AF}} \exp(ik\hat{x})$ can be described by the atom-field interaction Hamiltonian $\hat{V}_{\mathrm{AF}} \propto \hbar\Omega_{\mathrm{R}}/2$ with the bare coupling Rabi frequency Ω_{R}. With this Eq. 6.1 becomes

$$\hbar\Omega_{n,n'} = \langle F', m_F'| \hat{V}_{\mathrm{AF}} |F, m_F\rangle \langle n'| \exp(ik\hat{x}) |n\rangle = \hbar\,\Omega_{\mathrm{R}}\,C_{n,n'}. \tag{6.2}$$

The factor

$$C_{n,n'} = \langle n'| exp(ik\hat{x}) |n\rangle \approx \langle n'|n\rangle \tag{6.3}$$

in Eq. 6.2 is the Franck-Condon factor [82]. As the momentum transfer k is small for microwave photons, with a wavelength λ_{MW} several orders of magnitude larger than the spatial extend of $|n\rangle$, it is neglected here. To be able to analytically calculate the $C_{n,n'}$, the trapping potential in azimuthal direction is approximated by a 1-dimensional harmonic oscillator. For the trapping potential, as well as for the harmonic oscillator, the vibrational levels $n' \neq n$ are orthogonal, hence $C_{n,n'} = \delta_{n,n'}$ for transitions between two identical potentials. In our system, the trapping potentials of the individual Zeeman levels are displaced due to the fictitious magnetic field caused by the blue-detuned running wave trap laser. As a result, the overlap between the wave functions for $|n'\rangle$ and $|n\rangle$ is not necessarily zero for $n' \neq n$. For a 1-dimensional harmonic
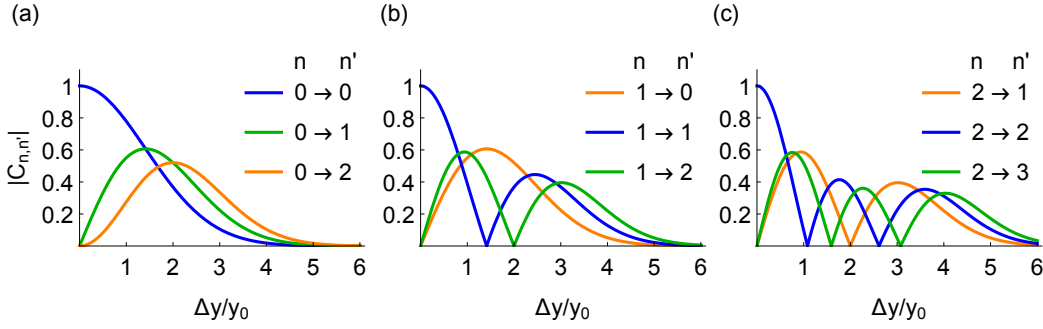
Figure 6.2: Frank-Condon factors $|C_{n,n'}|$ versus displacement Δy normalized to characteristic oscillator length y_0 for (a) $n = 0 \to n = \{0, 1, 2\}$ {blue, green, orange}, (b) $n = 1 \to n = \{0, 1, 2\}$ {orange, blue, green} and (c) $n = 2 \to n = \{1, 2, 3\}$ {orange, blue, green} transitions.

oscillator, the eigenfunctions $|n\rangle$ in the spatial representation are given by

$$\psi_n(y) = \frac{\mathcal{H}_n(y/y_0)}{\sqrt{2^n n! \sqrt{\pi} y_0}} \exp\left(-\frac{y^2}{2y_0^2}\right), \text{ with } y_0 = \sqrt{\frac{\hbar}{m\omega_y}}. \tag{6.4}$$

This equation includes the azimuthal trap frequency ω_y, atom mass m, characteristic oscillator length y_0 and Hermite polynomials $\mathcal{H}_n$. The Franck-Condon factor for a harmonic potential then becomes [83, 84], for $n' \geq n$,

$$C_{n,n'} = (-1)^{\Delta n} \exp\left(-\frac{|\eta|^2}{2}\right) \sqrt{\frac{n!}{n'!}} \eta^2 (i\eta^*)^{\Delta n} \mathcal{L}_n^{\Delta n}. \tag{6.5}$$

Here, $\Delta n = n' - n$, the $\mathcal{L}_p^{(m)}$ are associated Laguerre polynomials, and η is an effective Lamb-Dicke parameter,

$$\eta = \frac{\Delta y}{\sqrt{2} y_0}, \tag{6.6}$$

with the displacement Δy between the individual trap potentials. Plotting the calculated Frank-Condon factors $C_{n,n'}$ versus the displacement Δy, one sees that their evolution depends on the initial vibrational level. Figure 6.2 shows this for three examples starting at $n = \{0, 1, 2\}$ in (a),(b) and (c), respectively, for different $\Delta n = n' - n$. The displacement is normalized to the characteristic oscillator length y_0. The blue lines represent the Frank-Condon factors for $\Delta n = 0$, green lines indicate the $\Delta n = +1$ transitions and orange lines show the $C_{n,n'}$ for $\Delta n = +2$ in (a) and $\Delta n = -1$ in (b) as well as (c). These graphs clearly indicate, that for higher initial vibrational levels the Frank-Condon factors for the carrier transition decrease faster, while the maximum of the sideband occurs already for lower displacements. From this, it becomes clear that ensembles with higher temperatures, and therefore increased population in higher vibrational states, also have an increased number of different Frank-Condon factors

for the same displacement. Thus, there will be an inhomogeneous broadening of the Rabi frequency when driving microwave transitions. Another observation from Fig. 6.2 is, that the Frank-Condon factor becomes zero for specific combinations of displacement and vibrational level. For example, looking at Fig. 6.2(b) and $\Delta y/y_0 = 2$, the Frank-Condon factor is zero for $n = 1 \rightarrow n' = 2$, while other $C_{n,n'}$ are still of finite value.

Since the $C_{n,n'}$ for $n \neq n'$ are, however, mostly not zero for displaced trapping potentials, one can drive microwave transitions not only on the carrier transition ($n = n'$), but also on a transition ending at a higher or lower vibrational level n'. Thus, scanning the frequency of a microwave pulse around a specific transition between Zeeman levels of the two ground states and inferring the number of transferred atoms N_e, one can observe sidebands emerging for detunings higher and lower than the carrier frequency. The effects regarding the Frank-Condon factors mentioned above lead to unequal contributions of different vibrational states to the microwave spectrum. The frequency spacing between the sidebands and the carrier corresponds to the energy spacing between the adjacent vibrational levels, which is proportional to the azimuthal trap frequency ω_y. For an ideal harmonic oscillator in a thermal state the amplitude $A_{n\pm1}$ of the sidebands for the transition $n \rightarrow n \pm 1$ can be used to estimate the temperature of the atomic ensemble. Assuming that the width of the sidebands is a lot smaller than the trap frequency and the microwave transition is not saturated, the sideband amplitude is proportional to the mean number of motional excitations $\langle n \rangle$ [85]

$$\frac{\langle n \rangle}{\langle n \rangle + 1} = \frac{A_{n-1}}{A_{n+1}}. \tag{6.7}$$

Rearranging Eq. 6.7 one finds, that $\langle n \rangle$ is given by

$$\langle n \rangle = \frac{A_{n-1}}{A_{n+1} - A_{n-1}}. \tag{6.8}$$

The temperature T can be calculated assuming a Bose-Einstein distribution

$$\langle n \rangle = \left(\exp\left(\frac{\hbar \omega_y}{k_B T} \right) - 1 \right)^{-1}, \tag{6.9}$$

with the Boltzmann constant k_B. This simple calculation gives very good results for low $\langle n \rangle$. Reliable estimations for higher $\langle n \rangle$ get increasingly difficult as the Amplitudes of the sidebands $A_{n\pm1}$ converge. The colder the atomic ensemble, the more atoms are in the motional ground state, where no $n \rightarrow n - 1$ transition exists and therefore $A_{n-1} \rightarrow 0$.

To be able to infer more information from microwave spectra and slightly improve the precision of ensemble temperature measurements, a more involved model can be adopted. Here, we chose an optical Bloch equation model. Its set of equations can be derived from the master equation in Lindblad form

$$\dot{\rho}(t) = -\frac{i}{\hbar} \left[\hat{H}, \rho(t) \right] + \mathcal{L}(\rho(t)) \tag{6.10}$$

and give the time evolution of the density operator $\rho(t)$ for the simulated system with the Hamiltonian $\hat{H}$. The function $\mathcal{L}(\rho(t))$ contains the dipole decoherence rate γ_d, other decoherence

mechanisms, i.e. decay between the levels $|g\rangle$ and $|e\rangle$, are neglected here. To keep computational demands low, we assume the system to be composed of several independent two level atoms, with the ground and excited state being in a specific vibrational state of a 1-dimensional harmonic oscillator $|n\rangle$ and $|n'\rangle$ respectively. The two states $|g, n\rangle$ and $|e, n'\rangle$ are coupled by a microwave field which is described by V_{AF}. The Hamiltonian expressed in the rotating frame of the microwave frequency is then given by

$$\hat{H} = H_0 + V_{\text{AF}} = \begin{pmatrix} n\,\omega_{\text{y}} & \frac{\Omega_{n,n'}}{2} \\ \frac{\Omega_{n,n'}}{2} & n'\omega_{\text{y}} - \delta \end{pmatrix}, \tag{6.11}$$

with δ being the detuning of the microwave with respect to the bare transition frequency. Inserting Eq. 6.11 in Eq. 6.10, the individual equations for $\dot{\rho}(t)$ read ($\hbar = 1$)

$$\dot{\rho}_{ee}(t) = i \sum_{n,n'} \left[\frac{\Omega_{n,n'}}{2} \left(\rho_{eg}(t) - \rho_{ge}(t) \right) \right], \tag{6.12}$$

$$\dot{\rho}_{gg}(t) = -i \sum_{n,n'} \left[\frac{\Omega_{n,n'}}{2} \left(\rho_{eg}(t) - \rho_{ge}(t) \right) \right], \tag{6.13}$$

$$\dot{\rho}_{ge}(t) = -\sum_{n,n'} \left[\left(\gamma_d - i((n' - n)\,\omega_\phi + \delta) \right) \rho_{ge}(t) - i \frac{\Omega_{n,n'}}{2} \left(\rho_{ee}(t) - \rho_{gg}(t) \right) \right], \tag{6.14}$$

$$\dot{\rho}_{eg}(t) = -\sum_{n,n'} \left[\left(\gamma_d + i((n' - n)\,\omega_\phi - \delta) \right) \rho_{eg}(t) + i \frac{\Omega_{n,n'}}{2} \left(\rho_{ee}(t) - \rho_{gg}(t) \right) \right]. \tag{6.15}$$

Here, ρ_{ij} denotes the matrix elements of the density operator ρ. The sum over n, n' ensures that all possible combinations of vibrational states in $|g\rangle$ and $|e\rangle$ respectively are taken into account.

In order to obtain the total number of atoms N_e in the excited state, the respective density matrix element ρ_{ee} has to be referenced to the initial thermal population with the thermal occupation probability $p_n(T)$ given by

$$p_n(T) = \frac{1}{Z} \exp\left(-\frac{n\hbar\omega_y}{k_B T}\right), \text{ with } Z = \left(1 - \exp\left(-\frac{\hbar\omega_y}{k_B T}\right)\right)^{-1} \tag{6.16}$$

being the partition function. Via this thermal occupation probabilities, the ensemble temperature enters the fit model.

All in all, the free parameters for the fit are the ensemble temperature T, trap frequency ω_ϕ, bare Rabi frequency Ω_{R}, displacement Δy and dipole decoherence rate γ_{d}.

Until now, the trapping potential was considered to be a harmonic potential. This assumption is justified for small $\langle n\rangle$ (low temperature). For larger $\langle n\rangle$ the potentials deviate, as the harmonic potential gradient keeps increasing while the real trapping potential is finite in depth. The motional wave-functions obtained for both potentials are shown in Fig. 6.3(a) and (b), where (a) shows the approximated harmonic potential and (b) the anharmonic trapping potential, each with a selection of eigenfunctions $\psi_n(y)$, vertically separated by their eigenenergies. The depicted potentials are cuts along the y-axis at a x position corresponding to the radial trap minimum.
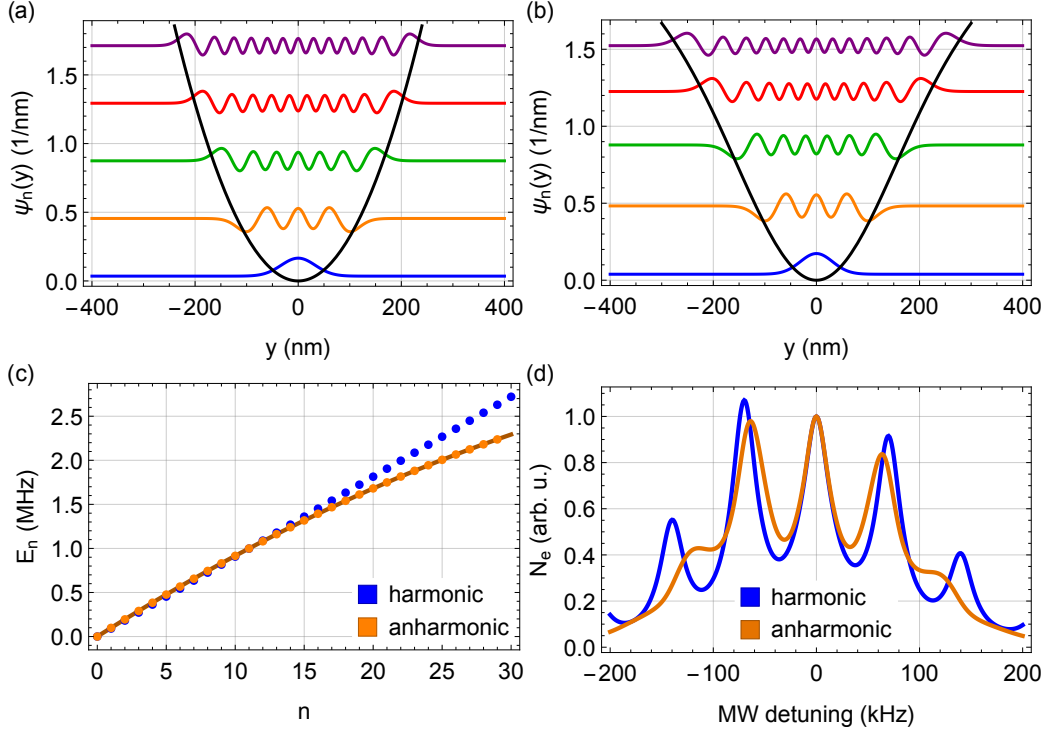
63

Figure 6.3: (a) Harmonic and (b) anharmonic trap potential (black) including eigenfunctions $\psi_n(y)$ for $n = \{0, 6, 12, 18, 24\}$ in {blue, orange, green, red, purple}. (c) Energy for a 1-dimensional harmonic (blue) and a 1-dimensional anharmonic (orange) trap potential. The solid orange line is a fit to the orange data points using $E_n = (\alpha n + \beta n^2)\,\omega_y$. (d) Simulated spectrum for harmonic potential (blue) and anharmonic potential (orange), for a microwave pulse length of $80\,\mu s$; other parameters as indicated in the text.

In Fig. 6.3(c), the respective eigenenergies of the nth vibrational state for the harmonic potential and the dipole trap potential are plotted. One can see that the energy levels of the trapping potential's bound states start to deviate from those of a harmonic potential for higher vibrational levels. Using a polynomial of order two to model the energy, $E_n = (\alpha n + \beta n^2)\,\omega_y$, the calculated anharmonicity of the trap can be taken into account. Fitting this model to the numerically calculated energies (solid line in Fig. 6.3(a)) gives for the fit parameters $\alpha = 1.013$ and $\beta = -0.0123$. In Fig. 6.3(d) a simulated spectrum for the pure harmonic potential (blue curve) is compared to a spectrum including the anharmonicity (orange curve), for fit parameters taken from previous experimental realizations ($T = 20\,\mu K$, $\omega_y = 70\,kHz$, $\Omega_R = 10\,kHz$, $\Delta y/y_0 = 0.56$, $\gamma_d = 10.7\,kHz$ and a microwave pulse length dt $= 80\,\mu s$). In the figure one can see the carrier transition at resonance and the first and second order sidebands detuned by $\pm\omega_y$ for the harmonic potential. The anharmonicity affects the spectrum as it leads to a broadening of the sidebands. Since the spacing between vibrational states is not equidistant for an anharmonic potential, the resonance frequency of a given $\Delta n \neq 0$ transition depends on the initial vibrational state. As the spectrum

is composed of the sum of all transitions, which have now slightly different frequencies, the sidebands are broadened. Comparing the spectra for a harmonic and an anharmonic potential, one notices that the spacing between the sidebands and the carrier is reduced for the anharmonic potential, especially when considering higher order sidebands. This change of the apparent trap frequency is a result of the reduced energy difference between the vibrational levels in an anharmonic potential. For increasing ensemble temperatures, the assumption of a harmonic trapping potential becomes less accurate as the occupation probability for higher vibrational levels increases.

6.2 Manipulating the state-dependence of the trapping potential

As discussed in the previous section, the visibility of the sidebands in the microwave spectra relies on the displacement between the trap potential minima of different Zeeman states and, thus, on the overlap between the wave-functions of unequal vibrational levels.

The displacement can be quantitatively obtained by approximating the full nanofiber trapping potential as a 1-dimensional harmonic oscillator. Calculating the total trapping potential U_T including the azimuthal harmonic potential U_H and the fictitious magnetic field $\mathbf{B}_f$, but excluding external offset fields, gives

$$U_T = U_H + \boldsymbol{\mu}\mathbf{B}_f = \frac{1}{2}m\,\omega_y^2\,\phi^2 R^2 + \mu_B\,g_F(F_x B_{fx} + F_y B_{fy}). \qquad (6.17)$$

Here, R is the radial distance from the nanofiber axis, g_F the Landé factor for the fine-structure level F and μ_B the Bohr magneton. Neglecting the contributions of $B_{fy}(\ll B_{fx})$ and assuming that $F_x\,|F,m\rangle = m_F\,|F,m\rangle$ is a good quantum number without an offset magnetic field, this simplifies to

$$\begin{aligned} U_T &= \frac{1}{2}m\,\omega_y^2\,\phi^2 R^2 + \mu_B\,g_F\,F_x B_f \\ &= \frac{1}{2}m\,\omega_y^2\,\phi^2 R^2 + \mu_B\,g_F\,m_F B_f. \end{aligned} \qquad (6.18)$$

Introducing $y = R\phi$, for small angles ϕ, one gets

$$U_T = \frac{1}{2}m\,\omega_y^2\,y^2 + \mu_B\,g_F\,m_F B_f. \qquad (6.19)$$

To get the minimum of the potential, its derivative is set to zero

$$\frac{\partial U_T}{\partial y} = m\,\omega_y^2\,y + \mu_B\,g_F\,m_F\frac{\partial B_f}{\partial y} = 0, \qquad (6.20)$$

yielding for the displacement, relative to the unperturbed harmonic potential,

$$\Delta y = -\frac{\mu_B\,g_F\,m_F\,b_f}{m\,\omega_y^2}, \text{ with } b_f = \frac{\partial B_f}{\partial y}. \qquad (6.21)$$

As evident from Eq. 6.21, the displacement of the azimuthal trap potentials depends, among others, on the considered Zeeman state and the gradient of the fictitious magnetic field. To

observe this experimentally, microwave spectra are used and analyzed. They are taken by using a square microwave pulse at a given frequency to transfer atoms in a specific Zeeman state from $F = 4$ to $F = 3$. The pulse duration is chosen to maximize the transfer efficiency on the carrier transition. The remaining atoms in $F = 4$ are removed by applying a push-out laser beam. The frequency of the microwave is scanned in equidistant steps. For each microwave frequency, the number of transferred atoms is estimated by measuring the absorption of a weak fiber-coupled light field resonant with the D2-line cycling transition $F = 4$ to $F' = 5$.

Since every residual fictitious magnetic field at the position of the atoms has the potential to spoil the quality of the spectra, careful adjustments are indispensable. Those residual fictitious field can, e.g., lead to the atoms on both sides being exposed to different total magnetic fields [46], causing a broadening or splitting in the microwave spectrum. Most critical in this context is the alignment of the trap laser polarizations as well as the power balance of the laser in standing wave configuration. In the optimal case, the fully quasi-linear polarizations of the trapping lasers are orthogonal and the powers of the two counter-propagating and co-polarized lasers generating the standing wave are equal. These parameters were optimized to achieve the minimal width of the peaks in the microwave spectra.

The experimental observation of the effect of the respective Zeeman state on the displacement, for a microwave detuning given with respect to the indicated $|F = 3, m_F\rangle$ to $|F = 4, m_F\rangle$ transition, as depicted in Fig 6.4(a), is shown in Fig. 6.4(b). The atom number N_e is normalized to the amplitude of the carrier. To be able to observe sidebands, an offset magnetic field $B_o = 1.56$ G was applied at an angle of $66.5°$. For more details on the magnetic offset field see
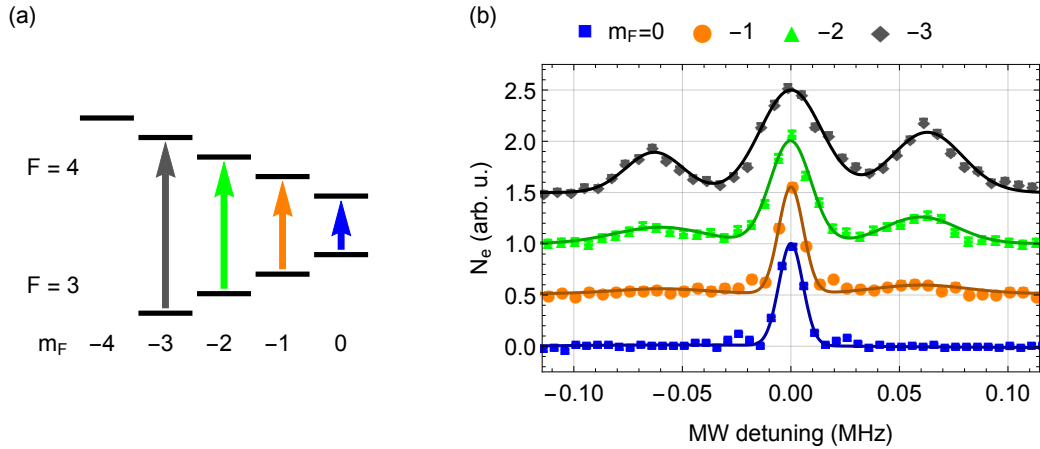
Figure 6.4: (a) Reduced level scheme for the ground-state manifold of Cs, the colored arrows indicate the driven microwave transition corresponding to the data points on the right. (b) measured microwave spectra for different π transitions starting at $m_F = 0$ (blue), $m_F = -1$ (orange), $m_F = -2$ (green) and $m_F = -3$ (black). The microwave detuning is given with respect to the carrier transition, N_e is normalized to the carrier amplitude. For better visibility, a vertical offset of 0.5 was added between the spectra. The fit (solid lines) is a sum of three Gaussian functions.

the paragraph below. For $m_\mathrm{F} = 0$, the microwave spectrum only shows one local maximum at the carrier transition. For $m_\mathrm{F} \neq 0$, two additional peaks appear, i.e., sidebands for $n \to n \pm 1$. The sideband on the left with negative microwave detuning corresponds to the $n \to n - 1$ transition. For higher m_F, the sidebands get more pronounced. This behavior corresponds to what was expected from Eq. 6.21 for small displacements Δy. For each microwave spectrum a fit consisting of the sum of three Gaussian functions (solid lines in Fig. 6.4(a)) can be used to estimate the amplitude $A_{\pm 1}$ of the sidebands, as well as their spectral shift with respect to the carrier.

In the following paragraphs, two possibilities to control the displacement, e.g. by manipulating the gradient of the fictitious magnetic field, will be discussed.

6.2.1 External magnetic field

The state dependence of the trapping potentials is caused by the gradient b_f of the x-component of the fictitious magnetic field B_f in azimuthal direction ϕ. A large homogeneous offset field B_0 along an axis orthogonal to the fictitious magnetic field can suppress the effective gradient b_e of the total magnetic field. A first estimation of the influence of the offset field in the x-y-plane can be given by looking at the total magnetic offset field $\mathbf{B}_\mathrm{T}$

$$\mathbf{B}_\mathrm{T} = \begin{pmatrix} B_0 \cos(\vartheta) + B_\mathrm{f} \\ B_0 \sin(\vartheta) \end{pmatrix} \Rightarrow B_\mathrm{T} = \sqrt{(B_0 \cos(\vartheta) + B_\mathrm{f})^2 + (B_0 \sin(\vartheta))^2}, \qquad (6.22)$$

with the angle ϑ between the x-axis and the vector of the offset magnetic field, see Fig. 6.5(a). Rearranging terms and using the Taylor series for $\sqrt{1 + x}$ for small x, translating to $B_0 \gg B_\mathrm{f}$ in this context, yields

$$B_\mathrm{T} \approx B_0 + B_\mathrm{f} \cos(\vartheta) + \frac{B_\mathrm{f}^2}{2B_0}. \qquad (6.23)$$

With this, the effective azimuthal gradient b_e becomes

$$b_\mathrm{e} = \frac{\partial B_\mathrm{T}}{\partial \phi} \propto b_\mathrm{f} \cos(\vartheta). \qquad (6.24)$$

Figure 6.5(b) shows microwave spectra for three settings for the angle ϑ of the magnetic offset field B_T. The microwave detuning is given with respect to the $|F = 4, m_\mathrm{F} = -4\rangle$ to $|F = 3, m_\mathrm{F} = -3\rangle$ transition. The atom number N_e is normalized to the amplitude of the carrier. For a magnetic field along the y-axis ($\vartheta = 90°$), the displacement of the azimuthal trap potential minimum vanishes. In this case, the wave functions of the vibrational states are orthogonal and the Franck-Condon factors are zero for $\Delta n \neq 0$ transitions. This is confirmed by the blue data points in Fig. 6.5(b), where only one local maximum is visible, indicating the carrier transition with $\Delta n = 0$. For $\vartheta = 73°$, the effective gradient increases and with it the displacement of the trap minima. This results in two additional local maxima in the microwave spectrum emerging for the orange data points in Fig. 6.5(b), representing sidebands. The sideband on the right with positive microwave detuning corresponds to the $n \to n - 1$ transition. By decreasing ϑ to $66°$ (green data points in Fig. 6.5(b)), the displacement and consequently the height of the sidebands increases further. The solid lines in Fig. 6.5(b) are fits to the data points, where each fit consists
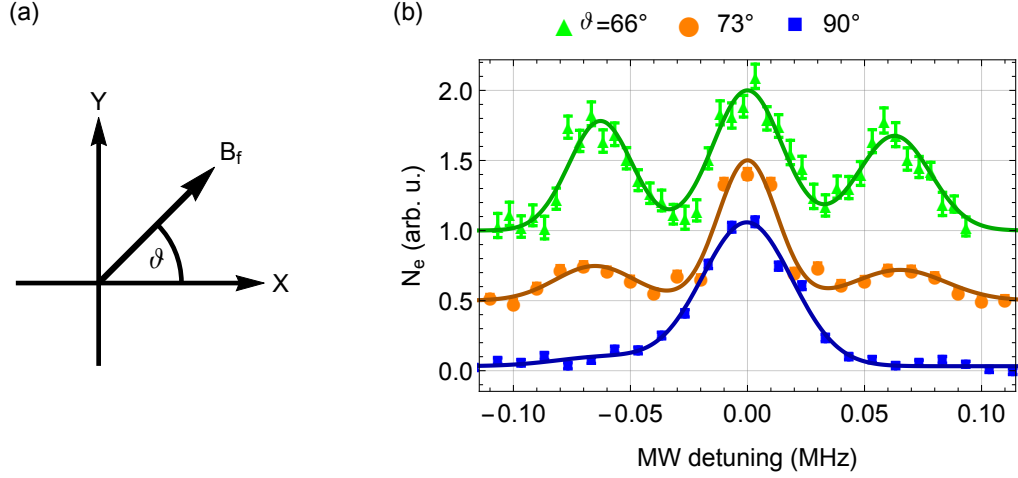
Figure 6.5: (a) Sketch of the offset magnetic field orientation. (b) measured microwave spectra for different angles of the offset magnetic field, $\vartheta = 90°$ (blue), $\vartheta = 73°$ (orange) and $\vartheta = 66°$ (green). The microwave detuning is given with respect to the carrier transition $|F=4, m_F=-4\rangle$ to $|F=3, m_F=-3\rangle$, N_e is normalized to the carrier amplitude. For better visibility, a vertical offset of 0.5 was added between the spectra. The fit (solid lines) is a sum of three Gaussian functions.

of the sum of three Gaussian functions. As in the previous paragraph the fits can be used to infer the amplitude $A_\pm$ and the spectral shifts of the sidebands.

Due to technical limitations in the current experimental setup, smaller angles than $66°$ can not be achieved while keeping the same total magnetic field. All further experiments were carried out at an offset magnetic field angle of $66°$, giving the largest experimentally achievable displacement at sufficient offset field strength.

The tuning of the trap laser polarizations had to be redone for every field angle. To this end, microwave spectra were taken for different settings of the trapping light fields polarizations and power balances of the light field in standing wave configuration. The parameters were optimized to achieve narrow peaks in the microwave spectra.

6.2.2 Additional light field

Another possibility to manipulate the displacement is using a fiber-coupled light field operating at the tune-out wavelength of about $880\,\text{nm}$. As the scalar component of the Stark shift vanishes for the ground state at this wavelength, the trap is, to the first order, not influenced by this additional light field. Similarly to the trapping light at $783\,\text{nm}$ wavelength, it features a fictitious magnetic field. Contrary to the trapping light field, the tune-out light field has an opposite sign of α_v (see chapter 3.1). By applying the tune-out light field, co-propagating with the trap laser and with the same quasi linear polarization inside the nanofiber, a partial compensation of the trap laser induced fictitious magnetic field is achievable. As the magnitude of the fictitious magnetic
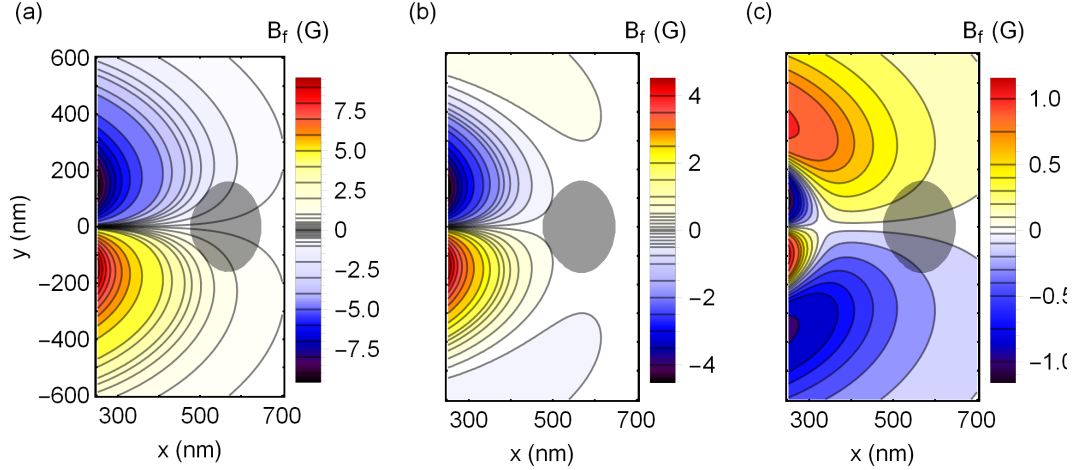
Figure 6.6: Contour plot of the x-component of the effective fictitious magnetic field B_f in the transverse plane around the nanofiber, induced by the trapping light field and the tune-out light field. The center of the nanofiber is at $x = y = 0$. The power of the tune-out light field is (a) $0\,\mathrm{mW}$, (b) $0.35\,\mathrm{mW}$ and (c) $0.6\,\mathrm{mW}$, respectively. The extent of the trap potential at $35\,\mathrm{\mu K}$ is indicated by the gray area. In the white area, the residual fictitious magnetic field is reduced to $|B_\mathrm{f}| < 0.025\,\mathrm{G}$. The following equipotential lines are at $|B_\mathrm{f}| = \{0.1\,\mathrm{G}, 0.2\,\mathrm{G}, 0.3\,\mathrm{G}, 0.4\,\mathrm{G}, 0.5\,\mathrm{G}, 0.75\,\mathrm{G}$ and $1\,\mathrm{G}\}$.

field scales with the light field power, this can be used to tune the compensation. In Fig 6.6, the calculated x-component of the effective fictitious magnetic field B_f due to the trap laser and the tune-out light field in the transverse plane is shown for different powers of the tune-out light field. For comparison, the fictitious magnetic field induced solely by the trapping light field is shown in Fig. 6.6(a). Since the radial extent of the individual fictitious fields differ, the compensation to a residual fictitious field smaller than $0.025\,\mathrm{G}$ is limited to a specific region, indicated by the white area in the contour plots. Atoms with a temperature of up to $35\,\mathrm{\mu K}$ are confined to a region depicted by the gray area. The fictitious field is well compensated within the range of movement of the atoms for a tune-out power of $0.35\,\mathrm{mW}$. A higher power leads to an overcompensation, where one can create an increasingly narrow corridor where $B_\mathrm{f} \approx 0$. Thus, this additional light field allows one to tailor the gradient of the fictitious magnetic field in the vicinity of the nanofiber-trapped atoms.

Figure 6.7(a) shows the calculated x-component of the effective fictitious magnetic field in azimuthal direction ϕ. The atoms are trapped at $\phi = \{0, \pi\}$. The green curve represents the situation without a tune-out light field. For $0.2\,\mathrm{mW}$ tune-out power (orange line), the effective fictitious field is expected to be reduced and for $0.35\,\mathrm{mW}$ (blue line) it is almost completely suppressed. The calculated tune-out light field power for the used trap configuration required to fully compensate the effect of the trap laser is calculated to be about $0.36\,\mathrm{mW}$.

In Fig. 6.7(b), microwave spectra for different applied tune-out laser powers are shown. The microwave detuning is given with respect to the $|F=4, m_\mathrm{F}=-4\rangle$ to $|F=3, m_\mathrm{F}=-3\rangle$ transi-
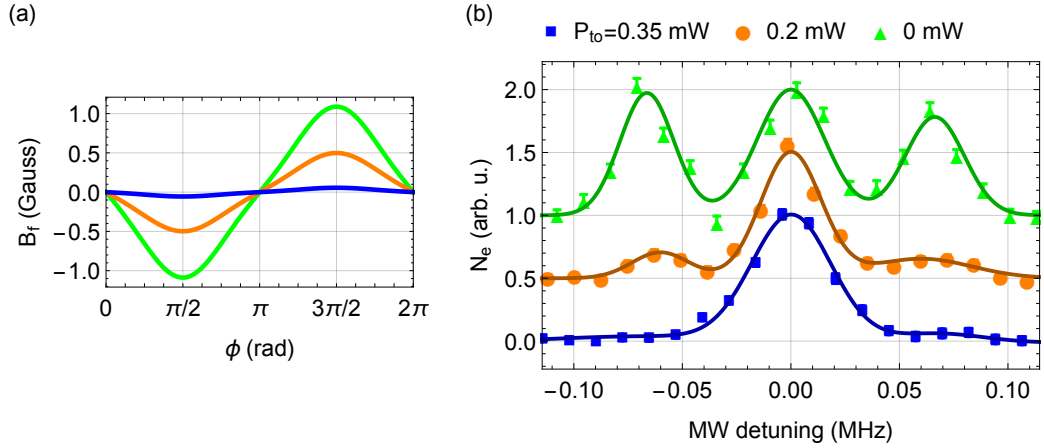
69

Figure 6.7: (a) x-component of the residual fictitious magnetic field B_f in dependence of the azimuthal position ϕ. The colors indicate the power of the tune-out light field corresponding to the data on the right. (b) measured spectra for different tune-out light field powers, $P_{to} = 0\,\text{mW}$ (green), $P_{to} = 0.2\,\text{mW}$ (orange) and $P_{to} = 0.35\,\text{mW}$ (blue). The microwave detuning is given with respect to the carrier transition $|F=4, m_F=-4\rangle$ to $|F=3, m_F=-3\rangle$, N_e is normalized to the carrier amplitude. For better visibility, a vertical offset of 0.5 was added between the spectra. The fit (solid lines) is a sum of three Gaussian functions.

tion. The atom number N_e is normalized to the amplitude of the carrier. The green data points show the microwave spectrum without tune-out laser. Here, one can observe three distinct local maxima which are the carrier transition and one sideband on each side of the carrier. All three peaks are almost equal in height. Applying $0.2\,\text{mW}$ of tune-out laser power (orange data points in Fig. 6.7(b)) reduces the height of the sidebands compared to the carrier. For this tune-out laser power, the fictitious magnetic field in the vicinity of the trapped atoms is already significantly reduced. For a tune-out laser power of $0.35\,\text{mW}$ (microwave spectrum with blue data points), there is only one local maximum visible, being the carrier transition. For this tune-out power, the fictitious field at the position of the atoms is almost completely compensated.

In all three figures Fig. 6.4 to Fig. 6.7, the fit underestimates the frequency spacing between the sidebands with values between $60\,\text{kHz}$ and $65\,\text{kHz}$. The calculated trap frequency is about $\omega_y = 70\,\text{kHz}$. This discrepancy can be explained by the anharmonicity of the trapping potential, see chapter 6.1. The temperature of the atomic ensemble can be estimated via the ratio of the amplitude of the sidebands $A_{n\pm1}$, see Eq. 6.8. In the cases presented so far the relevant sidebands have almost equal amplitude, meaning that $\langle n \rangle \gg 1$.
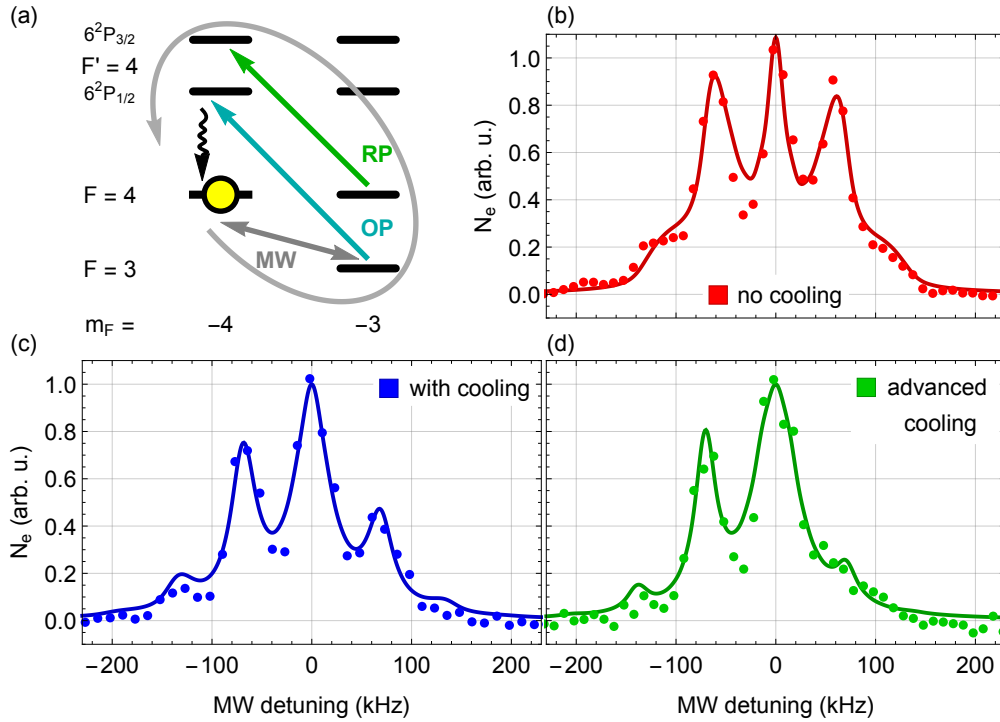
Figure 6.8: (a) Single cooling cycle with the microwave coupling (MW), a light field (OP) on the D1 line for optical pumping and a light field (RP) on the D2 line to repump atoms in $|F=4, m_{\mathrm{F}}=-3\rangle$. (b-d) Measured spectra (b) without cooling, (c) with 200 cooling cycles and (d) with 200 cooling cycles plus 30 additional cycles without RP. Solid lines are fits to the optical Bloch equation model (Eq. 6.15), the microwave detuning is with respect to the $|F=4, m_{\mathrm{F}}=-4\rangle \rightarrow |F=3, m_{\mathrm{F}}=-3\rangle$ transition. The atom number N_{e} is normalized to the amplitude of the carrier.

6.3 Microwave sideband cooling

One possibility to reduce the temperature of the atomic ensemble is to implement microwave sideband cooling. This is achievable for the azimuthal degree of freedom where sidebands, corresponding to the atomic motion in the azimuthal trapping potential, can be resolved in the microwave spectra. A single cooling cycle is sketched in Fig. 6.8(a), with the atoms initially in $|F=4, m_{\mathrm{F}}=-4\rangle$. It starts with a $20\,\mu\mathrm{s}$ long microwave pulse (MW) on the $n \rightarrow n-1$ sideband with bare Rabi frequency around $2\pi \times 40\,\mathrm{kHz}$. The atoms are then optically pumped back to the initial state using a σ^--polarized external light-field resonant on the $F=3 \rightarrow F'=4$ transition of the D1 line at $894\,\mathrm{nm}$ wavelength, labeled OP. During the optical pumping, the atoms have a finite probability of about $10\,\%$ to spontaneously decay into $|F=4, m_{\mathrm{F}}=-3\rangle$. Those atoms are re-integrated into the cooling cycle with a σ^--polarized external repumping

	ω_y (kHz)	Ω_R (kHz)	γ_d (kHz)
no cooling	70 ± 1.2	11 ± 0.7	6 ± 1
200 cycles	71 ± 1	11 ± 1	10 ± 1.6
200+30 cycles	71 ± 1.4	12 ± 0.5	8.6 ± 1.3

Table 6.1: Parameters of the cooling model obtained from the fit to the experimental data in Fig. 6.8

.

field, labeled RP, resonant on the $F = 4 \rightarrow F' = 4$ transition of the D2 line. Both OP and RP are on for $10\,\mu s$. To pump all atoms out of $F = 3$, OP is left on for additional $10\,\mu s$. If both lasers are perfectly σ^--polarized, all microwave transferred atoms should end up in the state $|F = 4, m_F = -4\rangle$, which is a dark state for the involved light fields.

The data points in Fig. 6.8(b) and (c) show microwave spectra with and without 200 cooling cycles, respectively. The spectra are normalized to the height of the carrier. The cooling results in a relative reduction of A_{n-1}, as expected. The model for fitting introduced in chapter 6.1 reproduces well the shape of the spectra, both without and with cooling. The obtained values for ω_y, Ω_R and γ_d agree well with expectations, and within the error they are the same for both data sets, see Tab. 6.1. Regarding the obtained data points with cooling, the fitted displacement $\Delta q/y_0 = 0.56 \pm 0.06$ is in perfect agreement with the calculated value of 0.56. Here $\Delta q = \Delta y - \Delta y'$ denotes the displacement between the two microwave coupled states, which are displaced by Δy and $\Delta y'$ respectively. Without cooling, the fit gives $\Delta q/y_0 = 0.34 \pm 0.02$. This discrepancy is attributed to the fact that hotter atoms are on average further away from the fiber [29], where the potential along ϕ is less confining. Equation 6.21 indicates that Δy scales with $1/R$, while y_0 scales with R, hence $\Delta q/y_0 \propto 1/R^2$. Finally, the fit allows one to extract a mean excitation number of $\langle n \rangle = 10 \pm 2$ before, and $\langle n \rangle = 1.4 \pm 0.3$ after cooling, corresponding to an initial and final temperature of around $35\,\mu K$ and $6\,\mu K$, respectively.

In order to explain why lower temperatures could not be reached, the background heating rate in the system was measured by introducing a variable waiting time after the last cooling cycle. Figure 6.9(a) shows the acquired $\langle n \rangle$ versus the waiting time. The heating rate of $0.34 \pm 0.06\,\mathrm{quanta/ms}$ is inferred from the linear fit (solid line), and compares well to previous estimates of $0.24\,\mathrm{quanta/ms}$ [45]. Since the cooling cycle supposedly removes one phonon per $40\,\mu s$ this heating rate should not be a substantial limitation regarding the minimal temperature that can be reached. Similarly the finite efficiency of the microwave pulse between $60\,\%$ and $70\,\%$ is not expected to be a significant constraint to the cooling efficiency. The main limitation, however, is identified to be excessive photon scattering during optical pumping and repumping. For technical reasons, the co-propagating OP and RP beams are at an angle of about $30°$ with respect to the offset magnetic field. This circumstance sets an upper limit on the degree of σ^- polarization that can be reached at the position of the atoms. As a consequence, the state $|F = 4, m_F = 4\rangle$ is not the desired dark state. This hypothesis can be confirmed by adding 30 cooling cycles where the RP light is off. With this, a mean excitation number of $\langle n \rangle = 0.3 \pm 0.1$ was obtained translating to a temperature of about $2\,\mu K$, which is close to the motional ground state, see Fig. 6.8(d). This reduction in temperature comes at the expense of loosing about $30\,\%$
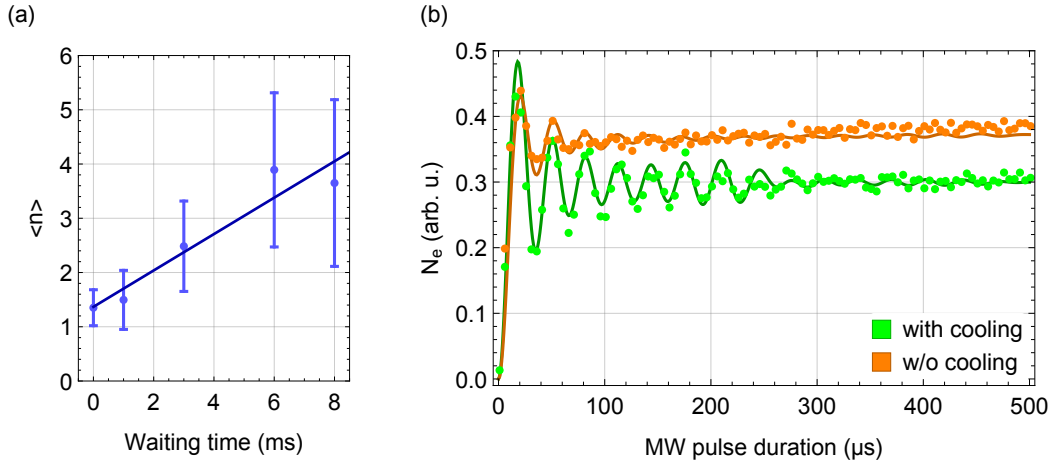
Figure 6.9: (a) Mean excitation number $\langle n \rangle$ over waiting time after the last cooling cycle. The solid line is a linear fit to the data points. The error bars are the uncertainties of the fit. (b) Measured Rabi oscillations for no cooling (orange) and 200 cooling cycles (green) on the $|F=4, m_F=-4\rangle \rightarrow |F=4, m_F=-3\rangle$ carrier transition. The solid lines are fits to the optical Bloch equation model.

of the atoms to other m_F states, where they can not contribute to the cooling cycle. However, assuming a thermal distribution, the absolute number of atoms in $|F=4, m_F=4\rangle$ that are in the motional ground state has increased.

Another indication of successful cooling are microwave driven Rabi oscillations between the states $|F=3, m_F=-3\rangle$ and $|F=4, m_F=-4\rangle$. They were recorded by applying a microwave pulse of variable duration on the carrier transition once without cooling and once after 200 cooling cycles. Figure 6.9(b) shows the transferred population as a function of pulse duration. Without cooling (orange data points), the Rabi oscillations are heavily damped because all the motional states involved have different Frank-Condon factors and, therefore, their own effective Rabi frequency. After 200 cooling cycles (green data points), the mean phonon number is reduced and only few motional states contribute, thus, the Rabi oscillations are less damped. The solid lines are fits to the optical Bloch equations model, that yield the same temperatures as the fits of the microwave spectra in Fig. 6.8(b) and (c).

The presented cooling technique allows one to reach azimuthal temperatures close to the motional ground state and can be a helpful tool for several applications, when extended to all three motional degrees of freedom. Those applications include experiments with atoms in optical microtraps as well as studies of self-organization [86, 87] and lateral light forces [88–91] for atoms close to waveguides. Furthermore it has the potential to provide well-defined starting conditions for loading atoms into surface-induced potentials [92] or for investigating collapse and revival dynamics in nanofiber-based traps [93].

CHAPTER 7

Summary

In this thesis, two effects stemming from the interaction between nanofiber-guided light fields and nanofiber-trapped atoms were investigated experimentally.

In the beginning, I briefly introduced optical nanofibers. In this context, I explained the production of the tapered optical fibers and gave a short overview on deriving the fiber-guided modes as well as the polarization properties in the evanescent field surrounding the nanofiber. In this section, I focused on the existence of a longitudinal polarization component that leads to almost fully circular polarization for a quasi-linearly polarized fiber-coupled light field. The orientation of the circular polarization is inverted on opposite sides of the fiber. These polarization properties have been used in the past to, e.g., side-selectively prepare the atoms in a specific Zeeman state [46], or demonstrate asymmetric scattering of photons, that were spontaneously emitted by the nanofiber-trapped atoms, into counter-propagating nanofiber-guided modes [94].

The following chapter covered the atom-light interaction of neutral Cesium atoms with the evanescent field of a nanofiber-coupled light field. Here, I briefly discussed the AC Stark shift and how we utilize it to trap the Cesium atoms in a nanofiber-based two-color dipole trap. Furthermore, I described how the combination of the effects of the vector part of the AC Stark shift and the polarization properties of the evanescent field lead to the emergence of fictitious magnetic fields, that act on the atoms the same way as real magnetic offset fields. If the fictitious magnetic field is combined with an external offset field that is oriented along the fictitious field, the azimuthal trapping potential minimum is spatially shifted, where the magnitude of the shift depends on the occupied Zeeman substate.

In the third chapter, I explained the main parts of the experimental setup used for the measurements presented in this thesis. I briefly described the vacuum setup as well as the optical setup. In this section, I gave more detailed information about a Fabry-Pérot bandpass filter we used to separate two light fields that are only about $9\,\mathrm{GHz}$ apart. Furthermore, I explained our method to precisely analyze and tune the polarization of the fiber-guided field in the nanofiber waist, which is based on detecting Rayleigh scattering via a sensitive CCD camera. After a section about an optical phase locked loop, required for our experiments regarding electromagnetically induced transparency (EIT), I introduced our detection and data acquisition system.

In the first chapter regarding the experiments conducted in the course of my PhD, I describe the path towards storing a fiber-guided light pulse in an ensemble of cold atoms. This experiment relies on EIT to gain access to the steep variation of the refractive index occurring at resonance. This variation can be utilized to decrease the group velocity of a light pulse propagating through the atomic ensemble and ultimately stop the light pulse within the medium. In this experiment we demonstrated an EIT window with a width in the kHz range, while maintaining a high transmission. Using this narrow EIT window, we were able to reduce the group velocity of a Gaussian shaped light pulse down to about $50\,\mathrm{m/s}$. Finally, we achieved storage of a light pulse for $2\,\mathrm{\mu s}$ with a combined storage and retrieval efficiency of about $3\,\%$.

In the last chapter, I described the second major experiment that is part of my work as a PhD student. This experiment aimed at exploring the effect of fictitious magnetic field induced state-dependent potentials on the nanofiber-trapped atoms. The state-dependent potentials lead to a Zeeman state and hyperfine level dependent spatial shift of the azimuthal trapping potential. Due to this spatial shift, the Franck-Condon factors for microwave transitions between the two ground states are nonzero, even for unequal phonon levels of the initial and final state. This gives rise to sidebands in a microwave spectrum, that are shifted from the central carrier frequency by the azimuthal trap frequency. The relative amplitude of the red- and the blue-detuned sidebands can be used to infer the temperature of the atomic ensemble. I presented three possibilities to tune the state dependency by preparing the atoms in specific Zeeman states, changing the angle of the external magnetic offset field and applying an additional fiber-guided light field at the tune-out wavelength. By driving microwave transitions on the sideband that removes phonons from the system, in combination with subsequent optical repumping, the temperature of the ensemble can be reduced. We were able to demonstrate in our system that this method can be used to reduce the mean excitation number from about $\langle n \rangle = 10$ to about $\langle n \rangle = 1.4$ after 200 consecutive cooling cycles. The main limitation of the cooling efficiency was found to be excessive photon scattering during optical repumping. By adapting the cooling cycle to take this into account we were able to reach a mean excitation number of $\langle n \rangle = 0.3$, corresponding to about $80\,\%$ of the atoms in the motional ground state of the azimuthal trapping potential.

Outlook

At the current state, there are two paths that can be followed with this setup regarding the presented experiments. One would be continuing with storage of photons in the nanofiber trapped ensemble of cold atoms, the other one would be to further investigate the spin-motion coupling present in this system.

An open research topic for the first path, apart from the already mentioned improvements of the storage and retrieval efficiencies, as well as adapting the experiment to store quantum information and entanglement, would be nonlinear optics with single photons. Due to the usually very weak nonlinear susceptibilities of materials, one typically requires high intensities to observe the interaction of two light fields. The scheme described in [95] is based on the use of EIT and slow light to observe the interaction of two weak light pulses, even down to the single photon level. The atomic levels involved are shown in Fig. 7.1(a). A weak light field Ω_1 and a strong control field Ω_2 couple the states $|A1\rangle$ and $|A2\rangle$, respectively, to the excited state $|A3\rangle$

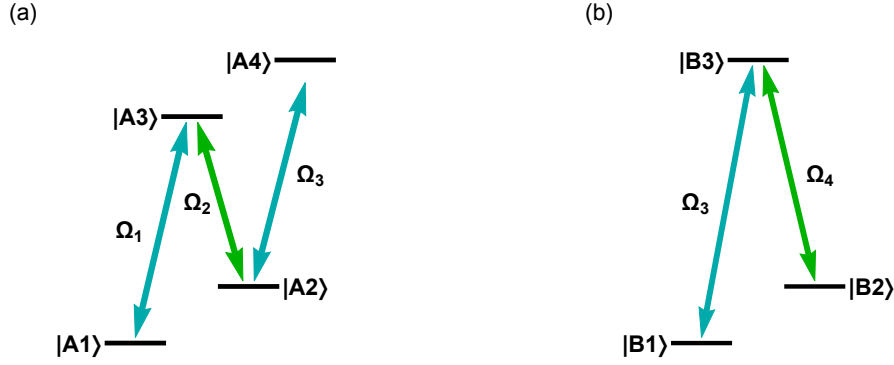**Figure 7.1:** (a) Weak light field Ω_1 and strong control field Ω_2 couple $|A1\rangle$ and $|A2\rangle$ to $|A3\rangle$. A second weak light field Ω_3 is detuned from the $|A2\rangle$ to $|A4\rangle$ transition and used to manipulate the refractive index experienced by Ω_1. (b) Λ-scheme with a weak light field Ω_3 and a control field Ω_4 used to reduce the group velocity of Ω_3 to maximize the interaction time with Ω_1.

in a typical Λ-scheme. As also shown in this thesis, the light field Ω_1 will be transmitted with low losses and a reduced group velocity. By adding a second weak light field Ω_3 that is detuned from resonance with the transition $|A2\rangle$ to $|A4\rangle$, the induced Stark shift of $|A2\rangle$ influences the the refractive index that is experienced by the light field Ω_1. This behavior leads to cross-phase modulation [75, 96]. To maximize the interaction time, the group velocity of the light field Ω_3 has to be reduced by having it interact with a second strong light field Ω_4 in a Λ-scheme consisting of a different set of levels as shown in Fig. 7.1(b). Implementing this, it should be possible for the light field Ω_1 to undergo a nonlinear phase shift that can be controlled by the light field Ω_3. A possible use of cross-phase modulation mediated by EIT is described in [97, 98] where its potential for realizing a controlled NOT gate for all-optical quantum computing is examined. The presented scheme can also be utilized for all-optical switching [99].

The spin-motion coupling model, briefly discussed in Ch. 3.3.2, still needs experimental verification and has to be extended to, e.g., include the radial degree of freedom. At this stage, we assume this coupling to be responsible for the preparation of the majority of the trapped atoms in the outermost Zeeman substate after ramping up a homogeneous external magnetic field along y. To be able to confirm our model, we need to infer the initial Zeeman state distribution without an external magnetic field applied. Since it is not possible to spectrally discern the Zeeman substates without a sufficiently high external magnetic field we have to „switch off" the spin motion coupling while increasing the magnetic field. One possibility to do so is to switch on the external magnetic field non-adiabatically, i.e., faster than the timescale of the spin-flips. Another possibility, indicated by first simulations, might be to apply an external magnetic field parallel to the fictitious magnetic field first and then one perpendicular to it.

Apart from elucidating the origin of the extraordinary „self" state preparation we observe, spin-motion coupling can also be used as an alternative cooling scheme. It utilizes the proposed exchange between the motional state and the spin state of the trapped atoms. Adiabatically

increasing the external magnetic field presumably leads to the already mentioned preparation of the atoms in the lowest energy Zeeman substate at the expense of increasing the phonon number. Decreasing the external magnetic field adiabatically leads to the opposite effect. If the atoms are prepared in a low-energy internal state, passing the resonance leads to higher energetic Zeeman sublevels being populated while the phonon number decreases. Implementing this in a cooling cycle, the basic model presented in this thesis hints that the trapped atoms can be cooled down to the motional ground state, with only one light field for optical pumping and without driving microwave transitions.

Bibliography

[1] C.H. Bennett and G. Brassard. Quantum cryptography: Public key distribution and coin tossing. *Proceedings of IEEE International Conference on Computers, Systems and Signal Processing*, pages 175–179, 1984.

[2] Nicolas Gisin, Grégoire Ribordy, Wolfgang Tittel, and Hugo Zbinden. Quantum cryptography. *Rev. Mod. Phys.*, 74:145–195, Mar 2002.

[3] M. A. Nielsen and I. L. Chuang. *Quantum Computation and Quantum Information*. Cambridge University Press, Cambridge, England, 2000.

[4] H. J. Kimble. The quantum internet. *Nature*, 453(7198):1023–1030, Jun 2008.

[5] D. Dieks. Communication by epr devices. *Physics Letters A*, 92(6):271 – 272, 1982.

[6] W. K. Wootters and W. H. Zurek. A single quantum cannot be cloned. *Nature*, 299(5886):802–803, Oct 1982.

[7] H.-J. Briegel, W. Dür, J. I. Cirac, and P. Zoller. Quantum repeaters: The role of imperfect local operations in quantum communication. *Phys. Rev. Lett.*, 81:5932–5935, Dec 1998.

[8] M. Żukowski, A. Zeilinger, M. A. Horne, and A. K. Ekert. "event-ready-detectors" bell experiment via entanglement swapping. *Phys. Rev. Lett.*, 71:4287–4290, Dec 1993.

[9] Nicolas Sangouard, Christoph Simon, Hugues de Riedmatten, and Nicolas Gisin. Quantum repeaters based on atomic ensembles and linear optics. *Rev. Mod. Phys.*, 83:33–80, Mar 2011.

[10] L.-M. Duan, M. D. Lukin, J. I. Cirac, and P. Zoller. Long-distance quantum communication with atomic ensembles and linear optics. *Nature*, 414(6862):413–418, Nov 2001.

[11] M. Fleischhauer and M. D. Lukin. Dark-state polaritons in electromagnetically induced transparency. *Phys. Rev. Lett.*, 84:5094–5097, May 2000.

[12] M. Fleischhauer, S.F. Yelin, and M.D. Lukin. How to trap photons? storing single-photon quantum states in collective atomic excitations1. *Optics Communications*, 179(1–6):395 – 410, 2000.

[13] M. Fleischhauer and M. D. Lukin. Quantum memory for photons: Dark-state polaritons. *Phys. Rev. A*, 65:022314, Jan 2002.

[14] Michael Fleischhauer, Atac Imamoglu, and Jonathan P. Marangos. Electromagnetically induced transparency: Optics in coherent media. *Rev. Mod. Phys.*, 77:633–673, Jul 2005.

[15] M. D. Eisaman, A. Andre, F. Massou, M. Fleischhauer, A. S. Zibrov, and M. D. Lukin. Electromagnetically induced transparency with tunable single-photon pulses. *Nature*, 438(7069):837–841, Dec 2005.

[16] T. Chaneliere, D. N. Matsukevich, S. D. Jenkins, S.-Y. Lan, T. A. B. Kennedy, and A. Kuzmich. Storage and retrieval of single photons transmitted between remote quantum memories. *Nature*, 438(7069):833–836, Dec 2005.

[17] Han Zhang, Xian-Min Jin, Jian Yang, Han-Ning Dai, Sheng-Jun Yang, Tian-Ming Zhao, Jun Rui, Yu He, Xiao Jiang, Fan Yang, Ge-Sheng Pan, Zhen-Sheng Yuan, Youjin Deng, Zeng-Bing Chen, Xiao-Hui Bao, Shuai Chen, Bo Zhao, and Jian-Wei Pan. Preparation and storage of frequency-uncorrelated entangled photons from cavity-enhanced spontaneous parametric downconversion. *Nat Photon*, 5(10):628–632, Oct 2011.

[18] Harold J. Metcalf and Peter van der Straten. *Laser Cooling and Trapping*. Springer-Verlag, 1999.

[19] D. M. Stamper-Kurn, M. R. Andrews, A. P. Chikkatur, S. Inouye, H.-J. Miesner, J. Stenger, and W. Ketterle. Optical confinement of a bose-einstein condensate. *Phys. Rev. Lett.*, 80:2027–2030, Mar 1998.

[20] S. R. Granade, M. E. Gehm, K. M. O'Hara, and J. E. Thomas. All-optical production of a degenerate fermi gas. *Phys. Rev. Lett.*, 88:120405, Mar 2002.

[21] Immanuel Bloch. Ultracold quantum gases in optical lattices. *Nat. Phys.*, 1(1):23–30, Oct 2005.

[22] Y. O. Dudin, L. Li, and A. Kuzmich. Light storage on the time scale of a minute. *Phys. Rev. A*, 87:031801, Mar 2013.

[23] Hidetoshi Katori, Masao Takamoto, V. G. Pal'chikov, and V. D. Ovsiannikov. Ultrastable optical clock with neutral atoms in an engineered light shift trap. *Phys. Rev. Lett.*, 91:173005, Oct 2003.

[24] Nicolas Schlosser, Georges Reymond, Igor Protsenko, and Philippe Grangier. Sub-poissonian loading of single atoms in a microscopic dipole trap. *Nature*, 411(6841):1024–1027, Jun 2001.

[25] Y. R. P. Sortais, H. Marion, C. Tuchendler, A. M. Lance, M. Lamare, P. Fournet, C. Armellin, R. Mercier, G. Messin, A. Browaeys, and P. Grangier. Diffraction-limited optics for single-atom manipulation. *Phys. Rev. A*, 75:013406, Jan 2007.

[26] T. Wilk, A. Gaëtan, C. Evellin, J. Wolters, Y. Miroshnychenko, P. Grangier, and A. Browaeys. Entanglement of two individual neutral atoms using rydberg blockade. *Phys. Rev. Lett.*, 104:010502, Jan 2010.

[27] X. L. Zhang, L. Isenhower, A. T. Gill, T. G. Walker, and M. Saffman. Deterministic entanglement of two neutral atoms via rydberg blockade. *Phys. Rev. A*, 82:030306, Sep 2010.

[28] A. M. Kaufman, B. J. Lester, M. Foss-Feig, M. L. Wall, A. M. Rey, and C. A. Regal. Entangling two transportable neutral atoms via local spin exchange. *Nature*, 527:208, 2015.

[29] E. Vetsch, D. Reitz, G. Sagué, R. Schmidt, S. T. Dawkins, and A. Rauschenbeutel. Optical interface created by laser-cooled atoms trapped in the evanescent field surrounding an optical nanofiber. *Phys. Rev. Lett.*, 104:203603, May 2010.

[30] A. Goban, K. S. Choi, D. J. Alton, D. Ding, C. Lacroûte, M. Pototschnig, T. Thiele, N. P. Stern, and H. J. Kimble. Demonstration of a state-insensitive, compensated nanofiber trap. *Phys. Rev. Lett.*, 109(3):033603, 2012.

[31] C. Sayrin, C. Clausen, B. Albrecht, P. Schneeweiss, and A. Rauschenbeutel. Storage of fiber-guided light in a nanofiber-trapped ensemble of cold atoms. *Optica*, 2(4):353–356, Apr 2015.

[32] B. Albrecht, Y. Meng, C. Clausen, A. Dareau, P. Schneeweiss, and A. Rauschenbeutel. Fictitious magnetic-field gradients in optical microtraps as an experimental tool for interrogating and manipulating cold atoms. *Phys. Rev. A*, 94:061401, Dec 2016.

[33] Florian Warken. *Ultradünne Glasfasern als Werkzeug zur Kopplung von Licht und Materie.* PhD thesis, Rheinische Friedrich-Wilhemls-Universtität Bonn, 2007.

[34] A. Thimothy Birks and Youwei W. Li. The shape of fiber tapers. *Journal of Lightwave Technology*, 10(4):432–438, 1992.

[35] Ariane Stiebeiner. *Nanofiber-based spectroscopy of organic molecules.* PhD thesis, Johannes Gutenberg-Universität Mainz, 2013.

[36] R. Garcia-Fernandez, W. Alt, F. Bruse, C. Dan, K. Karapetyan, O. Rehband, A. Stiebeiner, U. Wiedemann, D. Meschede, and A. Rauschenbeutel. Optical nanofibers and spectroscopy. *Applied Physics B*, 105(1):3–15, 2011.

[37] J. E. Hoffman, S. Ravets, J. A. Grover, P. Solano, P. R. Kordell, J. D. Wong-Campos, L. A. Orozco, and S. L. Rolston. Ultrahigh transmission optical nanofibers. *AIP Advances*, 4(6):–, 2014.

[38] Florian Warken, Arno Rauschenbeutel, and Thomas Bartholomäus. Fiber pulling profits from precise positioning. *Photonics Spectra*, 42(3), 2008.

[39] A. Stiebeiner, R. Garcia-Fernandez, and A. Rauschenbeutel. Design and optimization of broadband tapered optical fibers with a nanofiber waist. *Optics Express*, 18(22):22677–22685, 2010.

[40] Christian Wuttke. *Thermal excitations of optical nanofibers measured with a fiber-integrated Fabry-Pérot cavity*. PhD thesis, Johannes Gutenberg Universität Mainz, 2013.

[41] A. W. Snyder and J. D. Love. *Optical Waveguide Theory*. Chapman and Hall, New York, 1983.

[42] Amnon Yariv. *Optical Electronics in Modern Communications*. Oxford University Press, Inc., New York, 5th edition, 1997.

[43] John David Jackson. *Classical Electrodynamics*. John Wiley & Sons, Inc, 3rd edition, 1999.

[44] Fam Le Kien, V. I. Balykin, and K. Hakuta. Angular momentum of light in an optical nanofiber. *Phys. Rev. A*, 73:053823, May 2006.

[45] R. Mitsch. *Interaction and manipulation of nanofiber-trapped atoms with spin–orbit coupled light*. PhD thesis, Technische Universität Wien, 2014.

[46] R. Mitsch, C. Sayrin, B. Albrecht, P. Schneeweiss, and A. Rauschenbeutel. Exploiting the local polarization of strongly confined light for sub-micrometer-resolution internal state preparation and manipulation of cold atoms. *Phys. Rev. A*, 89:063829, Jun 2014.

[47] E. Arimondo, M. Inguscio, and P. Violino. Experimental determinations of the hyperfine structure in the alkali atoms. *Rev. Mod. Phys.*, 49:31–75, Jan 1977.

[48] Robert J. Rafac and Carol E. Tanner. Measurement of the ^{133}Cs$6p^2P_{1/2}$ state hyperfine structure. *Phys. Rev. A*, 56:1027–1030, Jul 1997.

[49] Carol E. Tanner and Carl Wieman. Precision measurement of the hyperfine structure of the ^{133}Cs $6P_{3/2}$ state. *Phys. Rev. A*, 38:1616–1617, Aug 1988.

[50] Fam Le Kien, Philipp Schneeweiss, and Arno Rauschenbeutel. Dynamical polarizability of atoms in arbitrary light fields: general theory and application to cesium. *EPJ D*, 67(5):92, 2013.

[51] Th. Udem, J. Reichert, R. Holzwarth, and T. W. Hänsch. Absolute optical frequency measurement of the cesium d_1 line with a mode-locked laser. *Phys. Rev. Lett.*, 82:3568–3571, May 1999.

[52] Peter J. Mohr and Barry N. Taylor. Codata recommended values of the fundamental physical constants: 1998. *Rev. Mod. Phys.*, 72:351–495, Apr 2000.

[53] Daniel A. Steck. Cesium d line data. available online at http://steck.us/alkalidata (revision 2.1.4, 23 December 2010). accessed 20 October 2016.

[54] Alan Corney. *Atomic and Laser Spectroscopy*. Oxford University Press, 1997.

[55] Robert W. Schmieder. Matrix elements of the quadratic stark effect on atoms with hyperfine structure. *American Journal of Physics*, 40(2):297–311, 1972.

[56] Abbas Khadjavi, Allen Lurio, and W. Happer. Stark effect in the excited states of rb, cs, cd, and hg. *Phys. Rev.*, 167:128–135, Mar 1968.

[57] N. L. Manakov, V. D. Ovisiannikov, and L. P. Rapoport. Atom in a laser field. *Physics Reports*, 141(6):320–433, 03 1986.

[58] P. Rosenbusch, S. Ghezali, V. A. Dzuba, V. V. Flambaum, K. Beloy, and A. Derevianko. ac stark shift of the cs microwave atomic clock transitions. *Phys. Rev. A*, 79:013404, Jan 2009.

[59] Ivan H. Deutsch and Poul S. Jessen. Quantum control and measurement of atomic spins in polarization spectroscopy. *Optics Communications*, 283(5):681 – 694, 2010. Quo vadis Quantum Optics?

[60] Fam Le Kien, P. Schneeweiss, and A. Rauschenbeutel. State-dependent potentials in a nanofiber-based two-color trap for cold atoms. *Phys. Rev. A*, 88:033840, Sep 2013.

[61] G. Sague. *Cold atom physics using ultra-thin optical fibres*. PhD thesis, Friedrich-Wilhelms-Universität Bonn, 2008.

[62] E. Vetsch. *Optical Interface Based on a Nanofiber Atom-Trap*. PhD thesis, Johannes Gutenberg-Universität Mainz, 2010.

[63] D. Reitz. *Coherent manipulation of nanofiber-trapped atoms*. PhD thesis, Johannes Gutenberg Universität Mainz, to be published.

[64] Wolfgang Demtröder. *Laserspektroskopie 2*. Springer Spektrum, 6th edition, 2013.

[65] Alexander I. Lvovsky, Barry C. Sanders, and Wolfgang Tittel. Optical quantum memory. *Nat Photon*, 3(12):706–714, Dec 2009.

[66] Georg Heinze, Christian Hubrich, and Thomas Halfmann. Stopped light and image storage by electromagnetically induced transparency up to the regime of one minute. *Phys. Rev. Lett.*, 111:033601, Jul 2013.

[67] M. Bajcsy, S. Hofferberth, V. Balic, T. Peyronel, M. Hafezi, A. S. Zibrov, V. Vuletic, and M. D. Lukin. Efficient all-optical switching using slow light within a hollow fiber. *Phys. Rev. Lett.*, 102:203902, May 2009.

[68] M. R. Sprague, P. S. Michelberger, Champion T. F. M., England D. G., Nunn J., Jin X.-M., Kolthammer W. S., Abdolvand A., Russell P. St. J., and Walmsley I. A. Broadband single-photon-level memory in a hollow-core photonic crystal fibre. *Nat Photon*, 8(4):287–291, Apr 2014. Letter.

[69] Erhan Saglamyurek, Jeongwan Jin, Varun B. Verma, Matthew D. Shaw, Francesco Marsili, Sae Woo Nam, Daniel Oblak, and Wolfgang Tittel. Quantum storage of entangled telecom-wavelength photons in an erbium-doped optical fibre. *Nat Photon*, 9(2):83–87, Feb 2015. Letter.

[70] B. Gouraud, D. Maxein, A. Nicolas, O. Morin, and J. Laurat. Demonstration of a memory for tightly guided light in an optical nanofiber. *Phys. Rev. Lett.*, 114:180503, May 2015.

[71] E. Vetsch, S. T. Dawkins, R. Mitsch, D. Reitz, P. Schneeweiss, and A. Rauschenbeutel. Nanofiber-based optical trapping of cold neutral atoms. *IEEE Journal of Selected Topics in Quantum Electronics*, 18(6):1763–1770, Nov 2012.

[72] Fam Le Kien and A. Rauschenbeutel. Propagation of nanofiber-guided light through an array of atoms. *Phys. Rev. A*, 90:063816, Dec 2014.

[73] E. Arimondo. Coherent population trapping in laser spectroscopy. *Progress in Optics*, 35:257 – 354, 1996.

[74] A. Kasapi, Maneesh Jain, G. Y. Yin, and S. E. Harris. Electromagnetically induced transparency: Propagation dynamics. *Phys. Rev. Lett.*, 74:2447–2450, Mar 1995.

[75] S. E. Harris and Lene Vestergaard Hau. Nonlinear optics at low light levels. *Phys. Rev. Lett.*, 82:4611–4614, Jun 1999.

[76] Alexey V. Gorshkov, Axel André, Mikhail D. Lukin, and Anders S. Sørensen. Photon storage in Λ-type optically dense atomic media. ii. free-space model. *Phys. Rev. A*, 76:033805, Sep 2007.

[77] D. Reitz, C. Sayrin, R. Mitsch, P. Schneeweiss, and A. Rauschenbeutel. Coherence properties of nanofiber-trapped cesium atoms. *Phys. Rev. Lett.*, 110:243603, Jun 2013.

[78] Claude Cohen-Tannoudji and Jacques Dupont-Roc. Experimental study of zeeman light shifts in weak magnetic fields. *Phys. Rev. A*, 5:968–984, Feb 1972.

[79] Konstantin Y. Bliokh and Franco Nori. Transverse and longitudinal angular momenta of light. *Phys. Rep.*, 592:1–38, 2015.

[80] Peter Lodahl, Sahand Mahmoodian, Søren Stobbe, Philipp Schneeweiss, Jürgen Volz, Arno Rauschenbeutel, Hannes Pichler, and Peter Zolleritsch. Chiral quantum optics. to be published, 2016.

[81] A. M. Kaufman, B. J. Lester, and C. A. Regal. Cooling a single atom in an optical tweezer to its quantum ground state. *Phys. Rev. X*, 2(4):041014, 2012.

[82] Leonid Förster, Michał Karski, Jai Min Choi, Andreas Steffen, Wolfgang Alt, Dieter Meschede, Artur Widera, Enrique Montano, Jae Hoon Lee, Worawarong Rakreungdet, and Poul S. Jessen. Microwave control of atomic motion in optical lattices. *Phys. Rev. Lett.*, 103(23):233001, 2009.

[83] D. J. Wineland and Wayne M. Itano. Laser cooling of atoms. *Phys. Rev. A*, 20:1521–1540, Oct 1979.

[84] K. E. Cahill and R. J. Glauber. Ordered expansions in boson amplitude operators. *Phys. Rev.*, 177:1857–1881, Jan 1969.

[85] D. J. Wineland, Wayne M. Itano, J. C. Bergquist, and Randall G. Hulet. Laser-cooling limits and single-ion spectroscopy. *Phys. Rev. A*, 36:2220–2232, Sep 1987.

[86] D. E. Chang, J. I. Cirac, and H. J. Kimble. Self-organization of atoms along a nanophotonic waveguide. *Phys. Rev. Lett.*, 110:113606, Mar 2013.

[87] Tobias Grießer and Helmut Ritsch. Light-induced crystallization of cold atoms in a 1d optical trap. *Phys. Rev. Lett.*, 111:055702, Aug 2013.

[88] Stefan Scheel, Stefan Yoshi Buhmann, Christoph Clausen, and Philipp Schneeweiss. Directional spontaneous emission and lateral casimir-polder force on an atom close to a nanofiber. *Phys. Rev. A*, 92:043819, Oct 2015.

[89] Francisco J. Rodriguez-Fortuno, Nader Engheta, Alejandro Martinez, and Anatoly V. Zayats. Lateral forces on circularly polarizable particles near a surface. *Nat. Commun.*, 6:8799, Nov 2015.

[90] Sergey Sukhov, Veerachart Kajorndejnukul, Roxana Rezvani Naraghi, and Aristide Dogariu. Dynamic consequences of optical spin–orbit interaction. *Nat. Photon.*, 9(12):809–812, 2015.

[91] Farid Kalhor, Thomas Thundat, and Zubin Jacob. Universal spin-momentum locked optical forces. *Appl. Phys. Lett.*, 108(6), 2016.

[92] D E Chang, K Sinha, J M Taylor, and H J Kimble. Trapping atoms using nanoscale quantum vacuum forces. *Nat. Commun.*, 5:4343, jul 2014.

[93] Fam Le Kien, K. Hakuta, D. Reitz, P. Schneeweiss, and A. Rauschenbeutel. Quantum dynamics of an atom orbiting around an optical nanofiber. *Phys. Rev. A*, 87:063607, Jun 2013.

[94] R. Mitsch, C. Sayrin, B. Albrecht, P. Schneeweiss, and A. Rauschenbeutel. Quantum state-controlled directional spontaneous emission of photons into a nanophotonic waveguide. *Nat. Commun.*, page 5:5713, 2014.

[95] M. D. Lukin and A. Imamoğlu. Nonlinear optics and quantum entanglement of ultraslow single photons. *Phys. Rev. Lett.*, 84:1419–1422, Feb 2000.

[96] H. Schmidt and A. Imamoglu. Giant kerr nonlinearities obtained by electromagnetically induced transparency. *Opt. Lett.*, 21(23):1936–1938, Dec 1996.

[97] Jeffrey H. Shapiro. Single-photon kerr nonlinearities do not help quantum computation. *Phys. Rev. A*, 73:062305, Jun 2006.

[98] Julio Gea-Banacloche. Impossibility of large phase shifts via the giant kerr effect with single-photon wave packets. *Phys. Rev. A*, 81:043823, Apr 2010.

[99] Chi-Ching Lin, Meng-Chang Wu, Bor-Wen Shiau, Yi-Hsin Chen, Ite A. Yu, Yong-Fan Chen, and Ying-Cheng Chen. Enhanced all-optical switching with double slow light pulses. *Phys. Rev. A*, 86:063836, Dec 2012.

Danksagung